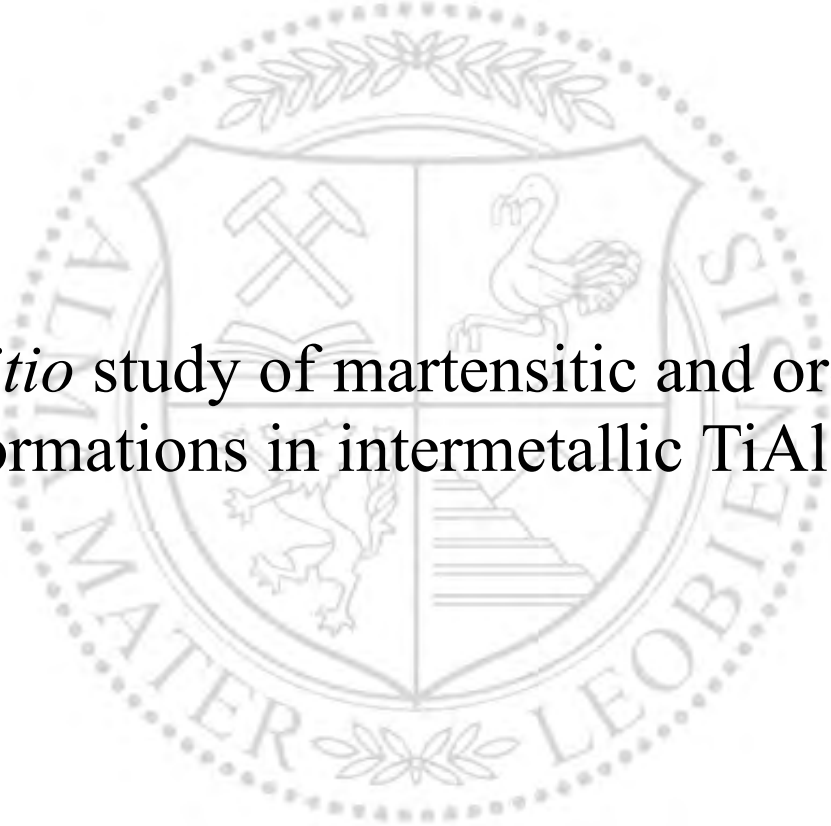




Chair of Physical Metallurgy and Metallic Materials

Doctoral Thesis



*Ab initio* study of martensitic and ordering transformations in intermetallic TiAl-alloys

Neda Abdoshahi

July 2021



**MONTANUNIVERSITÄT LEOBEN**

www.unileoben.ac.at

**AFFIDAVIT**

I declare on oath that I wrote this thesis independently, did not use other than the specified sources and aids, and did not otherwise use any unauthorized aids.

I declare that I have read, understood, and complied with the guidelines of the senate of the Montanuniversität Leoben for "Good Scientific Practice".

Furthermore, I declare that the electronic and printed version of the submitted thesis are identical, both, formally and with regard to content.

Date 05.07.2021

*Neda Abdoshahi*

Signature Author  
Neda Abdoshahi

## **Preface**

The original research introduced in this dissertation was conducted at the Department of Materials Science at the Montanuniversität Leoben, Austria, under the supervision of Priv.-Doz. Dr. David Holec. As a recipient of an FWF fellowship of the Austrian Science Fund(FWF), project Number P29731-N36 at the Department of Materials Science, I gratefully acknowledge the funding from the Austrian Science Fund over a period of four years (June 2017 to June 2021).

I dedicate this dissertation to my parents, Tahere and Manouchehr, because they instilled in me the desire to pursue my passions and reach my goals.

تقدیرم به پدر و مادر عزیزم ماکبر و  
تاهیر حسرت هرگز عشق و ان نیت  
اینجایم تا به نیت و در سال تحصیل من به نیت  
دانشگاه، طهر و در این مسیر سخت و طولانی ماکبر و تاهیر عزیزم .

To my daughter Maria, for she forever knows that she can achieve the unimaginable. I hope she understands why Mommy spends so much time in her office.

My dear husband, Masoud, I dedicate this to you because your support, patience, encouragement, and the most important point *"your love,"* has allowed me to complete this journey.

---

# Acknowledgments

First and foremost, I would like to express sincere thanks to my supervisor, Priv.-Doz. Dr. David Holec, who led me to this research field and patiently guided me through (the dissertation process) my PhD program. This dissertation could not have been possible without his continuous support, encouragement, and unmatched mentoring. Research in materials science with a background in solid state physics was not easy for me; the simulation part being the easiest on the journey, but interpreting the concepts obtained by simulations being the toughest. It was David's guidance and care that kept me moving forward and helped me reach my goal. He inspired me to grow as a student and as a researcher. David was the most patient supervisor who never got fed up from my questions and discussions, at least not showing that to me! Thank you, David, working with you, was very important and inspiring for me.

I would like to express my sincere gratitude to Prof. Dr. Mojmír Šob and Dr. Martin Friák, for providing me with their thoughtful comments and valuable suggestions. Thank you for always encouraging me to my work. Especially, Martin often started his emails to me with the word "*excellent*", this has been stamped on my mind.

I would like to offer my special appreciation to Dr. Boryana Rashkova for her individual guidance and support during the last four years. Whenever I was disappointed, she always told me "*you can*" and pushed me forward.

My humble gratitude also goes to Dipl.-Ing. Dominik Gehringer for always being "*my friend*". Thank you for your scientific and mental help, cheerful dinners, and supportive hugs!

Many thanks must also go to Assoz. Prof. Dr. Svea Mayer and Dr.-Mont. Petra Spörk-Erdely for their nice advice, discussions and kindly sharing office with me.

I would also like to thank Angelika Tremmel, Susanne Strasak, and Regina Kranz for their continued reassuring support during the journey towards this goal.

---

# Contents

<b>Contents</b>	<b>vi</b>
<b>1 Introduction</b>	<b>6</b>
1.1 Materials science and simulation . . . . .	6
1.2 Designing alloys: towards the prediction of materials properties . . . . .	8
1.3 State-of-the-art . . . . .	8
1.3.1 TiAl-based alloys . . . . .	8
1.3.2 Alloying and phase transformations . . . . .	9
1.3.3 Martensitic and ordering transformations . . . . .	11
1.4 Goals of the thesis . . . . .	11
1.5 Structure of the thesis . . . . .	12
<b>2 Methods</b>	<b>13</b>
2.1 Schrödinger equation in a many-body system . . . . .	13
2.2 From wave function methods to density functional theory . . . . .	14
2.2.1 Born-Oppenheimer approximation . . . . .	14
2.2.2 Hartree-Fock method . . . . .	15
2.2.3 Hohenberg-Kohn theorems . . . . .	16
2.2.4 Kohn-Sham equations . . . . .	18
2.2.5 The exchange-correlation potential . . . . .	19
2.2.6 Local density approximation (LDA) . . . . .	20

2.2.7	Generalized gradient approximation (GGA)	21
2.2.8	Basis wave functions	21
2.2.9	Periodic boundary conditions	22
2.2.10	Pseudopotentials	23
2.2.11	Muffin-tin orbitals	24
2.3	Structural stability	24
2.3.1	Chemical stability	24
2.3.2	Mechanical stability	24
2.4	The elastic properties of crystals	26
2.4.1	Single crystalline Young's modulus	27
2.5	Polycrystalline bulk, shear, and Young's modulus	28
2.6	Quasi-harmonic approximation (QHA)	29
2.6.1	The used concepts	29
<b>3</b>	<b>Simulation setup</b>	<b>31</b>
3.1	Structural models	31
3.1.1	Phases with composition $\text{Ti}_{0.5}\text{Al}_{0.5}$	31
3.2	Computational methods	33
3.3	Structural connections	35
3.3.1	Bcc-to-fcc structural connections	35
3.3.2	Bcc-to-hcp structural connections	39
<b>4</b>	<b>Structural properties</b>	<b>42</b>
4.1	TiAl-binary alloys	42
4.2	Ternary TiAl+Mo system	44
4.2.1	Cell shape optimization	44
4.2.2	Chemical stability	46
4.2.3	Phase stability	49

4.3	CPA vs supercell approach . . . . .	49
4.3.1	Local relaxations . . . . .	49
4.3.2	Spontaneous transformation $B19 \rightarrow \beta_o$ . . . . .	52
<b>5</b>	<b>Mechanical properties</b>	<b>55</b>
5.1	Elastic properties . . . . .	55
5.2	Impact of Mo on ductility . . . . .	57
5.3	Elastic anisotropy . . . . .	57
<b>6</b>	<b>Quasi-harmonic approximation: towards thermal expansion</b>	<b>61</b>
6.1	Temperature dependency of volume and $c/a$ ratio . . . . .	61
6.2	Heat capacity and bulk modulus . . . . .	64
6.3	Conclusion . . . . .	66
6.4	Analytical fits . . . . .	66
<b>7</b>	<b>Ordering temperatures as a function of Mo</b>	<b>69</b>
7.1	Configurational entropy . . . . .	69
7.2	Ordering temperature . . . . .	71
<b>8</b>	<b>Bcc to fcc phase transformations</b>	<b>74</b>
8.1	Ground-state properties . . . . .	74
8.2	Tetragonal Bain's path for the stoichiometric TiAl phases . . . . .	76
8.3	Trigonal transformation in the stoichiometric TiAl . . . . .	78
8.4	Impact of Mo on the $\beta_o \leftrightarrow \gamma$ and $\beta \leftrightarrow \gamma_{\text{dis}}$ transformations in TiAl . . . . .	81
8.5	Structural peculiarities of the TiAl(+Mo) system . . . . .	84
8.5.1	Supercell size vs. SQS . . . . .	91
8.6	Spontaneous transformation as a function of the Mo content . . . . .	92
8.6.1	Experimental evidence . . . . .	93
<b>9</b>	<b>Cubic to hexagonal martensitic transformations</b>	<b>95</b>



9.1	Potential energy surface and the energy barriers for binary TiAl system .	95
9.1.1	$\beta_o \rightarrow$ B19 martensitic transformation . . . . .	95
9.1.2	$\beta \rightarrow \alpha'$ martensitic transformation . . . . .	96
9.1.3	Comparison with the CPA method . . . . .	98
9.1.4	Strain energy . . . . .	101
9.2	Energy barrier for ternary martensitic TiAl+Mo system . . . . .	103
<b>10</b>	<b>Conclusion and outlook</b>	<b>105</b>
10.1	Summary of result . . . . .	105
10.2	Proposed future work . . . . .	107
	<b>Bibliography</b>	<b>108</b>

---

# List of abbreviations and symbols

## Abbreviations and acronyms

a.u.	arbitrary units
CP	Cauchy pressure
CPA	coherent potential approximation
ENCUT	cut-off
DFT	density functional theory
EMTO	exact muffin-tin orbital
<i>ext.</i>	external factor for electron cloud
GGA	generalized gradient approximation
gs-cs	ground state optimized cell shape
hcp	hexagonal-closed pack
LCAO	linear combination of atomic orbitals
LDA	local density approximation
LLD	local lattice displacement
MC	Monte Carlo
MD	molecular dynamics
MEP	minimum energy path
NN	nearest neighbor
OPW	orthogonalized plane waves
PAW	projector augmented-wave
PBE	Perdew-Burke-Ernzerhof
PES	potential energy surface
QHA	quasi-harmonic approximation
RT	room temperature
sc	simple cubic
SQS	special quasi-random structure
SRO	short-range order (parameter)
TEC	thermal expansion coefficient

to-cs	temperature optimized cell shape
T	transformed
VASP	Vienna Ab initio Simulation Package
vib	vibrations

## Symbols

### Latin alphabet

$a$	lattice parameter
$a_0$	equilibrium lattice parameter
$A_G$	polycrystalline shear anisotropy
$b$	lattice parameter
bcc	body centered cubic
$B$	bulk modulus
$B_R$	Reuss's bulk modulus
$B_V$	Voigt's bulk modulus
$B'$	pressure derivative of bulk modulus
$c$	lattice parameter
$c_0$	equilibrium lattice parameter
$C_{ij}$	$6 \times 6$ matrix of elastic constants
$C_p$	heat capacity at constant pressure
$e^{i\mathbf{k}\mathbf{r}}$	plain wave
$e$	elementary charge
$E$	energy
$E_f$	energy of formation
$E_0$	equilibrium energy
$E_{\langle hkl \rangle}$	Young's modulus in a direction $\langle hkl \rangle$
$E_{\text{strain}}$	strain energy
$E_{\text{tot}}$	total energy
$E_{\text{xc}}$	exchange-correlation energy
$F$	Helmholtz free energy
$F_{HK}$	Hohenberg-Kohn functional
$F(V, T)$	Helmholtz free energy as a function of volume and temperature
$\mathbf{G}$	reciprocal lattice vector
$G(p, T)$	Gibbs free energy as a function of pressure and temperature
$G_R$	Reuss's shear modulus
$G_V$	Voigt's shear modulus
$H$	Hamiltonian (operator)
$\hbar$	reduced Planck's constant

$H_{HF}$	Hartree-Fock energy
$H_{KS}$	Kohn-Sham Hamiltonian (operator)
$\mathbf{k}$	wave vector
$K_B$	Boltzman constant
$l_{h,k,l}$	directional cosines of the direction $[h, k, l]$
$M$	number of nuclei
$m$	mass of an electron
$M_j$	mass of $j^{th}$ nuclei
$N$	number of electrons
$n(\vec{r})$	electron charge density
$p$	pressure
$\mathbf{R}_j$	position of $j^{th}$ nucleus
$\mathbf{r}_i$	position of $i^{th}$ electron
$S_{ij}$	compliance coefficients
$S_{conf}$	configurational entropy
$S_{\text{muffin-tin}}$	muffin-tin radius
$T$	temperature
$\hat{T}_{\text{elec.}}$	kinetic energy of electrons
$\hat{T}_{\text{nucl.}}$	kinetic energy of nuclei
$T_{ord}$	ordering temperature
$V$	volume
$V_0$	equilibrium volume
$V_H$	Hartree potential
$V_I$	interstitial region potential
$V_{\text{muffin-tin}}$	muffin-tin potential
$\hat{V}_{\text{eff.}}$	effective potential
$\hat{V}_{\text{elec.}}$	potential energy of electrons
$\hat{V}_{\text{nucl.}}$	potential energy of nuclei
$V(\mathbf{r}, t)$	non explicit time-dependent operator
$\hat{V}_{\text{ext.}}$	external potential
$V_{xc}$	exchange-correlation potential
$x$	composition of an alloy
$Z_j$	atomic number of nucleus $j$

## Greek alphabet

$\alpha_a$	lattice thermal expansion in the $a$ -direction
$\alpha_c$	lattice thermal expansion in the $c$ -direction
$\alpha_j$	Warren-Cowley SRO of a coordination shell $j$
$\delta_c$	cell shape changes

$\delta_s$	atomic planes shuffling
$\varepsilon_0$	vacuum permittivity
$\nabla^2$	Laplace operator
$\phi$	single electron wave function
$\Psi(\mathbf{r}, t)$	time-dependent wave functions
$\psi(\mathbf{r})$	time-independent wave functions

---

# Abstract

Titanium aluminides are technologically important intermetallic alloys with many properties interesting also from a basic research point of view. When alloyed with Mo, several (meta)stable phases have been reported; their properties are, largely unknown due to the alloy processing and/or non-existence as a single-phase material. We employed first principles calculations to study compositional trends in structural and mechanical properties. We could show that Mo increases the density of all studied phases, leads to their chemical destabilization with the exception of the ordered bcc  $\beta_o$  phase, increases their ductility, and enhances the elastic anisotropy. Anisotropic thermal expansion coefficients of tetragonal  $\gamma$ -TiAl and hexagonal  $\alpha_2$ Ti<sub>3</sub>Al phases were calculated. The predicted values show that for  $\gamma$ -TiAl, the more computational demanding method with decoupled impact of volume and temperature effects on the cell shape leads to significantly better results than that with only ground-state optimized unit cell geometry. Predictions of ordering temperatures solely based on the configurational entropy do not yield values in the experimentally expected ranges. Furthermore, bcc-fcc structural transformations of  $\beta/\beta_o \rightarrow \gamma_{\text{dis}}/\gamma$  TiAl+Mo are studied. In particular, tetragonal (Bain's path) and trigonal transformations are combined with the concept of special quasi-random structures and examined. Our calculations of the ordered phases show that the  $\beta_o \rightarrow \gamma$  tetragonal transformation is barrierless, i.e., proceeds spontaneously, reflecting the genuine structural instability of the  $\beta_o$  phase. Upon alloying of  $\approx 7.4$  at.% Mo, a small barrier between  $\beta_o$  and  $\gamma$ -related local energy minima is formed. Yet a higher Mo content of  $\approx 9$  at.% leads to an opposite-direction barrierless transformation  $\gamma \rightarrow \beta_o$ , i.e., fully stabilizing the  $\beta_o$  phase. The martensitic bcc-hcp transformation for TiAl+Mo alloys were reported. Since the Potential Energy Surfaces (PES) clearly suggest that the minimum energy paths are not straight connections of the initial and final states, we have additionally relaxed the ionic positions along the transformation paths. We could show that elastic energy is a decent approximation of PES as a function of cell shape and fixed atomic positions, provided the initial structure is mechanically stable. The transformation energy landscape as a function of Mo content predicts that, adding Mo favors  $\beta_o/\beta$  phase on the expense of B19/ $\alpha'$ , eventually leading for spontaneous, barrierless transformations B19 $\rightarrow \beta_o$  and  $\alpha' \rightarrow \beta$  for 12.5 at.% Mo.

## Kurzfassung

Titanaluminide sind technologisch wichtige intermetallische Legierungen mit vielen Eigenschaften, die auch aus Sicht der Grundlagenforschung interessant sind. Durch Legieren mit Mo wurden mehrere (meta)stabile Phasen gefunden deren Eigenschaften, aufgrund des Herstellungsprozesses und/oder als einphasiges Material nicht existieren, weitgehend unbekannt sind. Ab-Initio Berechnungen wurden verwendet, um Trends in den strukturellen und mechanischen Eigenschaften, abhängig von der chemischen Zusammensetzung zu untersuchen. Wir konnten zeigen, dass Mo die Dichte aller untersuchten Phasen erhöht, zu ihrer chemischen Destabilisierung mit Ausnahme der geordneten bcc  $\beta_o$ -Phase führt, ihre Duktilität erhöht und die elastische Anisotropie verstärkt. Weiters wurden anisotrope thermische Ausdehnungskoeffizienten von tetragonalen  $\gamma$ -TiAl- und hexagonalen  $\alpha_2$ Ti<sub>3</sub>Al-Phasen berechnet. Die berechneten Werte zeigen, dass für  $\gamma$ -TiAl die rechenintensivere Methode mit entkoppeltem Einfluss von Volumen- und Temperatureffekten auf die Simulationsgeometrie zu deutlich besseren Ergebnissen führt als diejenige bei dem die Zellgeometrie (Gitterparameter) nur im Grundzustand optimiert wurde. Vorhersagen von Ordnungstemperaturen, die allein auf der Konfigurationsentropie basieren, liefern keine Werte in den experimentell erwarteten Bereichen. Weiters wurden bcc-fcc-Strukturumwandlungen von  $\beta/\beta_o \rightarrow \gamma_{\text{dis}}/\gamma$  TiAl+Mo untersucht. Tetragonale (Bain's path) und trigonale Transformationen mit dem der wurden mit optimiert statistisch zufälligen Strukturmodellen (Special Quasi-random Structures) modelliert und untersucht. Unsere Berechnungen der geordneten Phasen zeigen, dass die tetragonale  $\beta_o \rightarrow \gamma$ -Transformation keine Energiebarriere zeit, d.h. spontan abläuft, was die echte strukturelle Instabilität der  $\beta_o$ -Phase widerspiegelt. Beim Legieren von  $\approx 7.4$  at.% Mo bildet sich eine kleine energetische Barriere zwischen den  $\beta_o$  und  $\gamma$ -bezogenen lokalen Energieminima. Ein höherer Mo-Gehalt von  $\approx 9$  at.% führt jedoch zu einer entgegengesetzt gerichteten barrierefreien Umwandlung  $\gamma \rightarrow \beta_o$ , d.h. zu einer vollständigen Stabilisierung der  $\beta_o$ -Phase. Zudem wurde auch die martensitische bcc-hcp-Umwandlung für TiAl+Mo-Legierungen untersucht. Da die Potentialhyperflächen deutlich darauf hinweisen, dass die minimalen Energiepfade keine geraden Verbindungen der Anfangs- und Endzustände sind, haben wir zusätzlich die Ionenpositionen entlang der Umwandlungspfade optimiert, um den energetisch günstigsten Umwandlungspfad zu finden. Wir konnten zeigen, dass die elastische Energie eine akzeptable Näherung der Potentialhyperfläche als Funktion der Zellform und der konstanten Atompositionen darstellt, vorausgesetzt, die Ausgangsstruktur ist mechanisch stabil. Die Transformationsenergielandschaft als Funktion des Mo-Gehalts sagt voraus, dass die Zugabe von Mo die  $\beta_o/\beta$ -Phase auf Kosten von B19/ $\alpha'$  begünstigt, was schließlich zu spontanen, barrierefreien Transformationen B19  $\rightarrow \beta_o$  und  $\alpha' \rightarrow \beta$  für 12,5 at.% Mo führt.

---

# List of publications

## Peer-reviewed publications as the first author

- Neda Abdoshahi, Petra Spoerk-Erdely, Martin Friák, Svea Mayer, Mojmír Šob, and David Holec, *Ab initio study of chemical disorder as an effective stabilizing mechanism of bcc-based, TiAl(+Mo)*, Phys. Rev. Materials 4 (2020) 103604 (DOI: [10.1103/PhysRevMaterials.4.103604](https://doi.org/10.1103/PhysRevMaterials.4.103604)).

**Abstract:** In order to shed new light on the complex microstructural evolution in the Ti–Al–Mo system, we employ *ab initio* calculations to study bcc-fcc structural transformations of ordered  $\beta_o$ -TiAl(+Mo) and disordered  $\beta$ -TiAl(+Mo) to ordered  $\gamma$ -TiAl(+Mo) and hypothetically assume disordered  $\gamma_{\text{dis}}$ -TiAl(+Mo) alloys, respectively. In particular, tetragonal (Bain’s path) and trigonal transformations are combined with the concept of special quasi-random structures (SQS) and examined. Our calculations of the ordered phases show that the  $\beta_o \rightarrow \gamma$  tetragonal transformation of TiAl is barrierless, i.e., proceeds spontaneously, reflecting the genuine structural instability of the  $\beta_o$  phase. Upon alloying of  $\approx 7.4$  at.% Mo, a small barrier between  $\beta_o$  and  $\gamma$ -related local energy minima is formed. Yet a higher Mo content of  $\approx 9$  at.% leads to an opposite-direction barrierless transformation  $\gamma \rightarrow \beta_o$ , i.e., fully stabilizing the  $\beta_o$  phase. Considering the disordered phases, the  $\beta$ -Ti $_{0.5}$ Al $_{0.5-x}$ Mo $_x$  and  $\gamma_{\text{dis}}$ -Ti $_{0.5}$ Al $_{0.5-x}$ Mo $_x$  are energetically very close. Importantly, for all here considered compositions up to 11 at.% of Mo, a small energy barrier separates  $\beta$ -TiAl(+Mo) and  $\gamma_{\text{dis}}$ (+Mo) energy minima. Finally, a trigonal path was studied as an alternative transformation connecting disordered  $\beta$  and  $\gamma_{\text{dis}}$ -TiAl phases but it turns out that it exhibits an energy barrier over 60 meV/at. which, in comparison to the Bain’s path with 9 meV/at. barrier, effectively disqualifies the trigonal transformation for the TiAl system.

**My contribution:** I designed the study with the help of David Holec, Martin Friák, and Mojmír Šob; I performed all the calculations, evaluated, and visualized the data, and wrote the manuscript with the help of David Holec.



Parts of Chapters 3 and 8 are based on this publication.

- Neda Abdoshahi, Mohammad Dehghani, Lukas Hatzenbichler, Petra Spoerk-Erdely, Andrei V. Ruban, Michael Musi, Svea Mayer, Jürgen Spitaler, and David Holec, *Structural stability, mechanical properties and elastic anisotropy of TiAl+Mo alloys: a comprehensive ab initio study*, final draft ready for submission to an Acta Materialia.

**Abstract:** Titanium aluminides are technologically important intermetallic alloys with also many curious properties interesting from a basic research point of view. When alloyed with Mo, several (meta)stable phases have been reported; their properties are, however, largely unknown due to the alloy processing (e.g. fast cooling) and/or non-existence as a single-phase material. Here we employ first principles calculations to study compositional trends in structural and mechanical properties. We could show that Mo increases the density of all studied phases, leads to their chemical destabilization with the exception of the ordered bcc  $\beta_o$  phase, increases their ductility, and enhances the elastic anisotropy. Discrepancies between two employed *ab initio* methods (special quasi-random structures vs. coherent potential approximation) in the case of the  $\beta_o$  and B19 phases are rationalized with significant local distortions which may eventually facilitate a spontaneous phase transformation. Predictions of ordering temperatures solely based on the ordering energy yield values in the experimentally expected ranges.

**My contribution:** I designed the study with the help of David Holec; I performed all the calculations, evaluated, and visualized the data, and wrote the manuscript.

Parts of Chapters 3, 4, 5 and 7 are based on this manuscript.

- Neda Abdoshahi, Mohammad Dehghani, Petra Spoerk-Erdely, Andrei V. Ruban, Michael Musi, Svea Mayer, Jürgen Spitaler, and David Holec, *Diffusionless hexagonal-to-cubic transformations in TiAl+Mo alloys*, draft in preparation.

**Abstract:** A diffusionless transition from cubic to hexagonal phase has been suggested to take place upon rapid cooling of TiAl+Mo alloys. However, before this transition occurs, the cubic phase must become dynamically unstable with respect to distortions which transform it to the hexagonal structure. The first principle calculations of martensitic bcc-to-hcp transformation for binary and ternary TiAl(+Mo) alloys were reported. Since the potential energy surface (PES) clearly suggest that the minimum energy paths (MEPs) are not straight connections of the initial and final states, we have additionally relaxed the ionic positions using VASP supercell calculations, which yielded different result from the EMTO-CPA method. Further, elastic energy is shown to be a decent approximation of PES as

a function of volume shape change for fixed atomic positions, provided the initial structure is mechanically stable. Moreover the transformation energy landscape as a function of Mo content predicts that, adding Mo favors  $\beta_o/\beta$  phase on the expense of B19/ $\alpha'$ , eventually leading for spontaneous barrierless transformations B19 $\rightarrow\beta_o$  and  $\alpha'\rightarrow\beta$  for 12.5 at.% Mo.

**My contribution:** I designed the study with the help of David Holec; I performed all the calculations, evaluated, and visualized the data, and wrote the manuscript.

Parts of Chapters 3 and 9 are based on this manuscript.

## Peer-reviewed publications as a co-author

- David Holec, Neda Abdoshahi, Svea Mayer and Helmut Clemens, *Thermal Expansion and Other Thermodynamic Properties of  $\alpha_2$ -Ti<sub>3</sub>Al and  $\gamma$ -TiAl Intermetallic Phases from First Principles Methods*, Materials 12 (2019) 1292 (DOI: [10.3390/ma12081292](https://doi.org/10.3390/ma12081292)).

**Abstract:** Anisotropic thermal expansion coefficients of tetragonal  $\gamma$ -TiAl and hexagonal  $\alpha_2$ -Ti<sub>3</sub>Al phases were calculated using first principles methods. Two approaches with different computational costs and degrees of freedom were proposed. The predicted values were compared with available experimental data showing that for  $\gamma$ -TiAl, the more computational demanding method with decoupled impact of volume and temperature effects on the cell shape leads to significantly better results than that with only ground-state optimized unit cell geometry. In the case of the  $\alpha_2$ -Ti<sub>3</sub>Al phase, both approaches yielded comparable results. Additionally, heat capacity and bulk modulus were evaluated as functions of temperature for both phases, and were fitted to provide an analytical formula which can be further used

**My contribution:** I performed the calculations, evaluated the data, and contributed to writing the manuscript.

Chapters 2 and 6 are partly based on this manuscript.

- Mohammad Dehghani, Andrei V. Ruban, Jürgen Spitaler, Neda Abdoshahi and David Holec, *Stability and ordering of bcc and hcp TiAl+Mo: An ab initio study*, submitted to Physics Review Materials.

**Abstract:** Atomic ordering in bcc and hcp TiAl+Mo alloys near equiatomic TiAl composition is investigated by different *ab initio* tools. We show that small addition of Mo, about 5 at. %, is enough to make bcc alloys with more than 50 at. % of Ti stable with respect to the hcp alloys. Moreover, such alloying also leads to stabilizing the B2 ordered structure with respect to its B2<sub>2</sub> modification, which is

the bcc-based ground state structure of binary TiAl. The site preference of Mo in the B2 and B19 ordered alloys is investigated by different methods: in the dilute limit, using the transfer energy formalism; in concentrated alloys, from the total energies of disordered and partially-ordered alloys in the mean-field coherent potential approximation; and from Monte Carlo simulations. These methods produce consistent results for the B2 phase predicting a strong preference of Mo to Al sublattice. The site preference of Mo in the B19 phases varies from a weak preference for Al sites in the single impurity calculations to a quite strong preference for Ti sites in the mean-field approximation and finally to a strong Al preference in Monte Carlo simulations. Mo alloying dramatically increases the order-disorder transition temperatures in bcc and hcp Al-deficient  $\text{Ti}_{0.5}\text{Al}_{0.5-x}\text{Mo}_x$  alloys.

**My contribution:** I performed the VASP calculations, and contributed to editing the manuscript.

## Oral presentations

- Neda Abdoshahi, Mohammad Dehghani, Lukas Hatzenbichler, Andrei V. Ruban, Jürge Spitaler, and David Holec, *Structural phase stability, mechanical properties and elastic anisotropy of TiAl+Mo alloys: an ab initio assessment*, EUROMAT, Graz, Austria, **2021**
- Neda Abdoshahi, Martin Friák, Mojmír Šob and David Holec, *Ab initio study of tetragonal and trigonal bcc-fcc transformations in Ti-Al-Mo system*, CHARM, Brno, Czech Republic, **2019**.
- Neda Abdoshahi, Martin Friák, Mojmír Šob and David Holec, *Ab initio study of tetragonal and trigonal bcc-fcc transformations in TiAl-Mo system*, DPG, Regensburg, Germany, **2019**.
- Neda Abdoshahi, Svea Mayer, Helmut Clemens, and David Holec, *textitA novel approach to quasi-harmonic approximation for non-cubic structures: an application to the intermetallic Ti-Al based phases*, ICAMM, Rennes, France, **2019**.
- Neda Abdoshahi, Mohammad Dehghani, Andrei V. Ruban, Michael Musi, Petra Erdely, Svea Mayer, Jürgen Spitaler and David Holec, *Structural and elastic properties of TiAl+Mo alloys*, MSE, Darmstadt, Germany, **2018**.
- Neda Abdoshahi and David Holec, *Structural and elastic properties of  $\beta/\beta_0$  and  $\alpha'/\alpha'_2$  phases in TiAl+Mo*, Kirchdorf, Austria, **2018**.

- Neda Abdoshahi and David Holec, *Ordering and diffusionless transformations in  $TiAl$* , ViCoM conference, Vienna, Austria, **2018**.

---

# Introduction

## 1.1 Materials science and simulation

Computational materials science offers powerful tools to obtain insights into the materials' structures, behaviors, properties, and their response to imposed internal and external changes. Steadily increasing computational resources enable scientists to apply novel theories and to construct models closer to reality, thus improving the knowledge of materials systems and their components.

Similarly to a diversity of experimental methods, there are numerous theoretical modeling methods. Based on the considered material system and goals of the study, the proper modeling approach is chosen. For this purpose, briefly, the modeling techniques are briefly described below (see Fig. 1.1).

For a typical **mesoscale method**, e.g., dislocations and phase field, the continuum-based methods are employed. Therefore, mesoscale modeling techniques can predict the various parameters, describing the various physical phenomena, governing material behavior at different length scales, either in terms of continuum, thermodynamic descriptions or discrete particles and their interaction.

In order to describe materials on the **atomistic level**, interatomic interactions are needed. The most two famous and commonly applied techniques, making use of those interactions, are molecular dynamics (MD) and Monte Carlo (MC). *Semi-empirical* potentials usually are applied to simulate large systems with even billions of atoms. These techniques can predict the properties of many-particle interactions. The interatomic potential plays a crucial role regarding the accuracy of calculations.

Fitting and optimization of interatomic potentials are severely non-trivial and time-consuming tasks. An even more dramatic disadvantage of the interatomic potentials

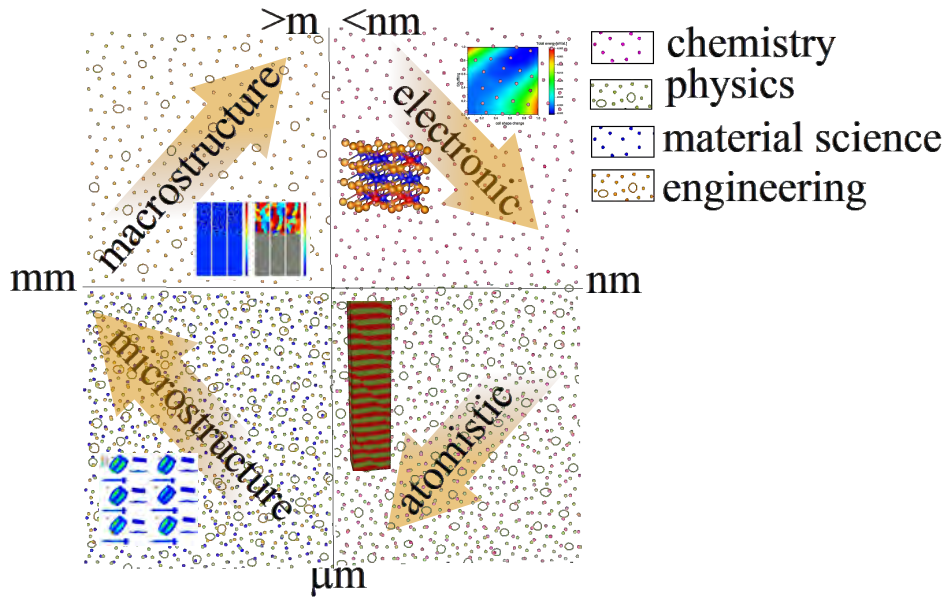


Figure 1.1: Overview of modeling techniques operating at different lengths and typically dealing with phenomena from various materials science disciplines (parts of the figure taken from Refs. [1, 2]).

is that they are not, in general, transferable. That means that each potential is fitted to a certain subset of the material properties. For example, there are potentials for the same elements, which are good at reproducing bulk mechanical properties, whilst others have predictive power for surface energies. These disadvantages affects the wide usage of these techniques in engineering materials science.

To gain detailed insight into the crystal structures **at the electronic level**, Density Functional Theory (DFT) is the method of choice in materials science. In this regard, it is the most popular approach, among so-called *first principles* or *ab initio* modeling which claims to use no input parameters. Thus it is suitable for predicting properties of materials in consistent and unbiased way, spanning from crystalline structures over individual atomistic processes to electronic structure and bonding. Although being a very accurate method, it is limited to only hundreds of atoms because of computational demands.

## 1.2 Designing alloys: towards the prediction of materials properties

An **alloy** is a combination of two or more elements while its properties are not determined by a single element only (for instance, a famous example is brass made from copper and zinc). A simple replacement of one element (e.g., Nb or Mo in TiAl-alloys) with another (e.g., Ni) results in completely different material behavior, and consequently application areas (e.g., shape memory NiTi-alloys vs. structural light-weight TiAl-alloys).

A deeper understanding of the chemical and physical mechanisms can be helpful to realize the diversity of properties of structurally similar intermetallic compounds. Within this study, first-principles methods are employed to come up with a theoretical model, to predict structural and mechanical properties of TiAl+Mo intermetallic alloys.

## 1.3 State-of-the-art

### 1.3.1 TiAl-based alloys

Titanium aluminides (TiAl) form a family of novel light-weight intermetallic alloys. Those alloys exhibit benefits such as low density, high specific yield strength, good corrosion, and oxidation resistance [3–7] making them heavily used in industry. Nevertheless, further studies to improve their weakness such as brittleness [8–10] are needed. The microstructures of the TiAl-alloys have two major constituents at room temperature (RT). An ordered tetragonal face-centered  $\gamma$ -TiAl phase ( $L1_0$ , space group  $P4/mmm$ ) and an ordered hexagonal  $\alpha_2$ -Ti<sub>3</sub>Al phase ( $D0_{19}$ , space group  $P63/mmc$ ) [11]. Both these phases are brittle, considering hot-forming at high temperatures [3, 11].

To overcome these weakness, the binary TiAl is alloyed with specific elements. For example, the cubic  $\beta$ -TiAl-based alloys have been developed with disordered bcc structure ( $A2$ , space group  $Im\bar{3}m$ ) which appears at elevated temperatures.  $\beta$ -TiAl arises in the equilibrium phase diagram of the binary Ti-Al system only at low Al contents [3, 12]. It can be stabilized by alloying with so-called  **$\beta$ -stabilizing elements** such as Mo or Nb.

More specifically, the body-centered cubic phase has two variants: the disordered high-temperature  $\beta$  phase, and a low-temperature ordered  $\beta_o$ -TiAl phase (B2, space group  $Pm\bar{3}m$ ). The ordered structure (CsCl-type) contains two sublattices, which in the case of binary TiAl are one fully occupied with Al and the other one with Ti atoms (see orange planes in Fig. 1.2b). In contrast, all sites in the disordered  $\beta$  phase are randomly occupied with both Al and Ti, since there are no specific sublattices (as shown in Fig. 1.2a). It is also possible to say that, there is only one sublattice for disordered cases.

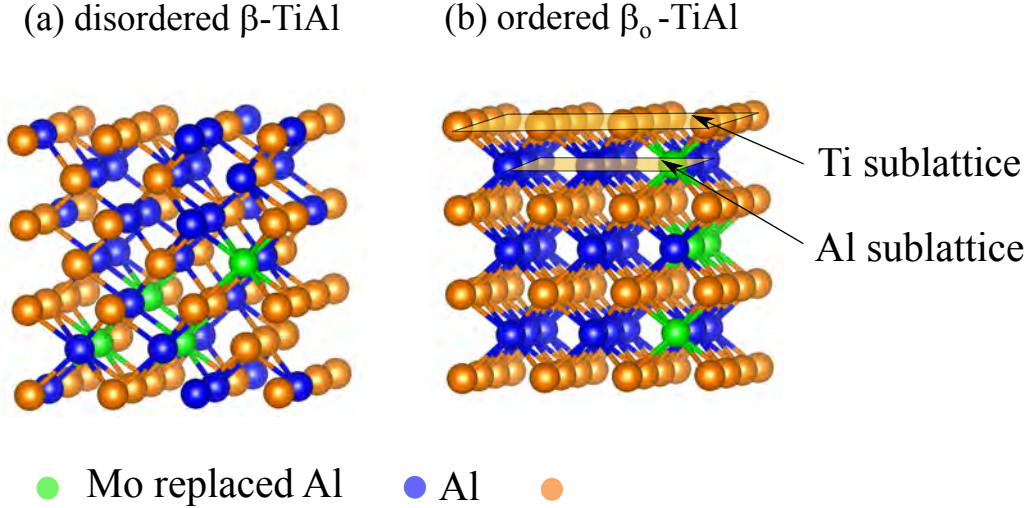


Figure 1.2: Structural model of (a) disordered  $\beta$  and (b) ordered  $\beta_o$  TiAl+Mo. For disordered  $\beta$  phase, the underlying structure is the bcc lattice on which Ti, Al and Mo atoms are fully mixed. In the case of the ordered structure  $\beta_o$ , the underlying lattice is B2 (with Ti and Al sublattices). Mo is shown to substitute only for Al.

The specific role of the disordered  $\beta$  phase is that it provides a sufficient number of independent  $\langle 111 \rangle \{110\}$  slip systems. Consequently, high-temperature workability is significantly improved. However, the phase fraction of the ordered  $\beta_o$  phase should be minimized at service temperature in order not to deteriorate, for example, the creep behavior as reported for various  $\beta/\beta_o$ -phase containing TiAl-alloys [3, 11, 13].

Depending on the exact chemical composition, the alloy passes through different phase fields upon its cooling. As a consequence, various temperature-dependent phase fractions of the  $\beta/\beta_o$ -phase are present at RT. Additionally, different degrees of order can be obtained. In our work, we have shown that structural disorder of the  $\beta$  phase has a similar stabilizing effect as alloying with ternary  $\beta$ -stabilizing Mo element [14]. We suggested that the stabilizing effect is connected with roughening the potential energy surface in the Born-Oppenheimer configurational space. Hence, it barriers appear along the  $\beta/\beta_o \rightarrow \gamma$  transformation path [14].

### 1.3.2 Alloying and phase transformations

As demonstrated by the phase diagram (Fig. 1.3), the final equilibrium composition of TiAl+Mo alloys strongly depends on their Mo content. The crossing of phase-field boundaries in equilibrium includes precipitation and/or dissolution of new phases, and hence involves diffusional processes. The actual phase constitution is additionally dependent on the speed of cooling. For extremely fast cooling rates, diffusion is inhibited.



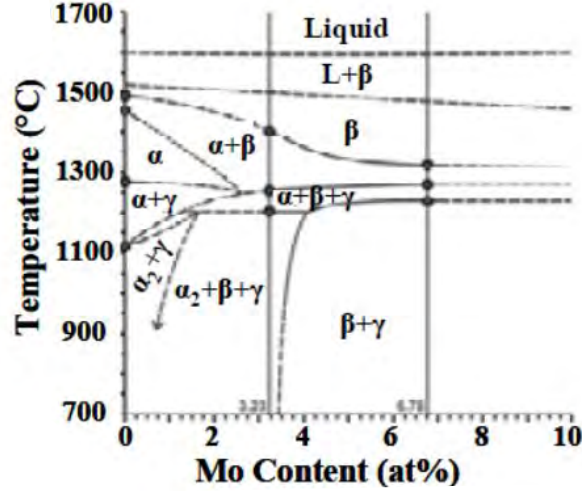


Figure 1.3: The equilibrium Ti-44Al+Mo (at.%) phase diagram [15].

Consequently, precipitation and growth of the  $\alpha/\alpha_2$  and  $\gamma$  phases (as present in the equilibrium phase diagram, Fig. 1.3) are suppressed, and instead, a martensitic hexagonal  $\alpha'/\alpha'_2$  phase appears in the  $\beta/\beta_o$  matrix. Being a martensitic variant implies that both the  $\alpha'/\alpha'_2$  phase and the  $\beta/\beta_o$  matrix have the same chemical composition. This microstructure has been observed recently for the first time in the Ti-44Al-3Mo (at.%) alloy [16]. Having a close-to-stoichiometric overall composition, the  $\alpha'_2$  phase becomes an Al supersaturated  $\alpha_2$  phase (which has a nominal composition  $\text{Ti}_3\text{Al}$ ).

The bcc-based  $\beta$  phase and hcp-based  $\alpha'_2$  phase exhibit the Burger's orientation relationship

$$[1\bar{1}1]_{\beta/\beta_o} \parallel [2\bar{1}\bar{1}]_{\alpha'/\alpha'_2} \quad (1.1)$$

and

$$(011)_{\beta/\beta_o} \parallel (0001)_{\alpha'/\alpha'_2} \quad (1.2)$$

The system has been studied previously by a number of experimental techniques, including light optical microscopy, scanning, and transmission electron microscopy, differential scanning calorimetry, conventional X-ray as well as high-energy X-ray diffraction or mechanical testing [17, 18]. These techniques allowed to establish a pseudo-binary phase diagram. Kabra *et al.* [17] used the neutron diffraction and concluded that the order-disorder temperature in Ti-44Al-7Mo alloy is 1265°C while it drops by  $\approx 30^\circ\text{C}$  when the Mo content is reduced to 3 at.%. The ordering temperature for the  $\alpha_2$  phase ( $\text{Ti}_3\text{Al}$ -based) has been estimated at 1205°C for the 3 at.% alloy variant.

Nevertheless, there is a lack of understanding of the ordering  $\beta \leftrightarrow \beta_o$  mechanisms, as well as no information on the ordering in the novel martensitic phase  $\alpha' \leftrightarrow \alpha'_2$  is available.

Particularly challenging is the case of martensitic microstructure, where the experimental setup does not allow for resolving the exact temperatures at which ordering and the martensitic transformation happen (due to the fast cooling rates applied).

Consequently, it is not known which of the phenomena occurs first, i.e., whether the martensitic transformation starts from the  $\beta_o$  or the  $\beta$  phase (and what consequences the starting configuration may have). Similarly, due to the lack of experimental data, the degree of ordering of the  $\beta_o$  matrix and the martensitic  $\alpha'_2$  phases on cooling to room temperature is not known.

### 1.3.3 Martensitic and ordering transformations

Forming of a low-symmetry orthorhombic B19-TiAl (B19, space group  $Pmma$ ) phase in  $\alpha_2$  phase was observed after fast cooling [19], by structural changes during  $\alpha \rightarrow \alpha_2 + \gamma$  [16], as well as in Ti-(40-44)Al-8.5Nb alloys [11]. The latter claims the B19 phase to be a transitional phase between  $\beta$  and/or  $\beta_o$  and an orthorhombic O-Ti<sub>2</sub>AlNb phase. Moreover, the appearance of the B19 phase was observed [20] in Ti-45Al-3Mo-0.1B alloy. For this comprehensive study it is necessary to understand and predict its structure and its behavior during the martensitic  $\alpha \rightarrow$ B19 phase transformation.

Apart from crystallographic phase transformations, at certain temperatures, both ordering processes  $\beta \leftrightarrow \beta_o$ ,  $\alpha \leftrightarrow \alpha_2$  can occur [21, 22] simultaneously. Additionally, martensitic transformations  $\beta \rightarrow \alpha'$  (disordered hexagonal Ti<sub>0.5</sub>Al<sub>0.5</sub>) and/or  $\beta_o \rightarrow \alpha'_2$  (partially ordered hexagonal Ti<sub>0.5</sub>Al<sub>0.5</sub> based on the  $\alpha_2$  phase) have been reported in Ti-44Al-3Mo alloys [15, 22].

Since many of those phases have only limited stability and/or appear only in complex multi-phase materials, their structural characterization is experimentally challenging. On the other hand, knowledge of compositional trends in mechanical properties is desirable for knowledge-based development and optimization of novel alloys based on the TiAl intermetallic system.

## 1.4 Goals of the thesis

This thesis aims on providing underlying material properties of TiAl+Mo ternary intermetallic system, and thereby on fundamental understanding of ordering phenomena and the martensitic transformation process in the TiAl+Mo system by means of atomistic calculations. The specific goal are:

- Calculate structural and mechanical properties of relevant ordered and disordered phases in ternary TiAl+Mo system using first principles calculations.

- Evaluate impact of configurational entropy on the ordering transformation temperature.
- Estimate transformation barriers for diffusionless transformations in the ternary TiAl+Mo system.

## 1.5 Structure of the thesis

To set the theoretical scene for the detailed prediction of the research questions described above, Chap. 2 discusses the relevant fundamentals of quantum mechanics, and the details of simulation set up are presented in Chap. 3. Chap. 4 introduces the major structural properties of the considered TiAl phases. The insight into the mechanical properties of phases and compositions is discussed particularly in Chap. 5. Chap. 7 addresses the ordering temperature behavior of  $\beta \rightarrow \beta_o$  and  $\alpha' \rightarrow \text{B19}(\alpha'_2)$ . The Chap. 6 and 8 which are mostly based on the author's own publications, provide new insights into the thermal properties and phase transformations, which both resulted as a side projects along the course of this study. The martensitic transformation  $\beta_o \rightarrow \text{B19}$  and  $\beta \rightarrow \alpha'$  is discussed in Chap. 9. Finally, the presented results are concluded and an outlook is given in Chap. 10.

## 2.1 Schrödinger equation in a many-body system



Erwin Schrödinger

One of the critical issues in theoretical physics and chemistry is understanding the structure of electrons in many-body systems. Unlike macro- to microscopic-scale problems, studying light particles such as electrons at nanoscale requires treatment within the quantum space. The basis of quantum mechanics is the Schrödinger equation, which requires writing the necessary descriptor of the Hamiltonian system. The starting point of a discussion is the time-dependent Schrödinger equation as follow:

$$i\hbar\frac{\partial}{\partial t}\Psi(\mathbf{r}, t) = \left( -\frac{\hbar^2}{2m}\nabla^2 + V(\mathbf{r}, t) \right)\Psi(\mathbf{r}, t) = \hat{H}\Psi(\mathbf{r}, t) \quad (2.1)$$

where the  $\mathbf{r}$  is a vector of the positions of many particles. If  $V(\mathbf{r})$  has no explicit dependency on time, then Eq. (2.1) simplifies to the time-independent Schrödinger equation:

$$\hat{H}\psi(\mathbf{r}) = E\psi(\mathbf{r}) . \quad (2.2)$$

In the this Eq. (2.2),  $\hat{H}$  indicates the Hamiltonian operator,  $\psi$  is the many-body wave function which depends on the coordinates of all nuclei and electrons and,  $E$  is the total energy of the system,

$$\psi \equiv \psi(\mathbf{r}_1, \mathbf{r}_2, \dots, \mathbf{r}_N; \mathbf{R}_1, \mathbf{R}_2, \dots, \mathbf{R}_M). \quad (2.3)$$

where it is considered a system containing  $N$  electrons and  $M$  nuclei at positions  $\{\mathbf{r}_i\}_{i=1}^N$  and  $\{\mathbf{R}_j\}_{j=1}^M$ , respectively.

To solve the Schrödinger equation for a solid represented as a many-body system, it is useful to note, that the Hamiltonian operator in Eq. (2.3) includes interactions between the electrons and atomic nuclei,

$$\begin{aligned}
\hat{H} &= \hat{T}_{\text{elec.}}(\{\mathbf{r}_i\}_{i=1}^N) + \hat{T}_{\text{nucl.}}(\{\mathbf{R}_j\}_{j=1}^M) + \hat{V}_{\text{elec.}}(\{\mathbf{r}_i\}_{i=1}^N) + \\
&+ \hat{V}_{\text{nucl.}}(\{\mathbf{R}_j\}_{j=1}^M) + \hat{V}_{\text{elec.-nucl.}}(\{\mathbf{r}_i\}_{i=1}^N, \{\mathbf{R}_j\}_{j=1}^M) = \\
&= -\frac{\hbar^2}{2} \sum_{i=1}^N \frac{\nabla_{\mathbf{r}_i}^2}{m} - \frac{\hbar^2}{2} \sum_{j=1}^M \frac{\nabla_{\mathbf{R}_j}^2}{M_j} + \frac{1}{8\pi\epsilon_0} \sum_{\substack{i,i'=1 \\ i \neq i'}}^N \frac{e^2}{|\mathbf{r}_i - \mathbf{r}_{i'}|} + \\
&+ \frac{1}{8\pi\epsilon_0} \sum_{\substack{j,j'=1 \\ j \neq j'}}^M \frac{e^2 Z_j Z_{j'}}{|\mathbf{R}_j - \mathbf{R}_{j'}|} - \frac{1}{4\pi\epsilon_0} \sum_{i=1}^N \sum_{j=1}^M \frac{e^2 Z_j}{|\mathbf{R}_j - \mathbf{r}_i|},
\end{aligned} \tag{2.4}$$

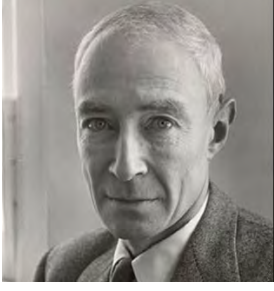
where  $m$  ( $M_j$ ) indicates the mass of an electron (a nucleus),  $\hbar$  is the reduced Planck's constant,  $\epsilon_0$  is the vacuum permittivity,  $e$  is the elementary charge, and  $Z_j$  the atomic number of a nucleus  $j$ . The first two terms,  $\hat{T}_{\text{elec.}}$  and  $\hat{T}_{\text{nucl.}}$  express electron-electron and nucleus-nucleus repulsion energies, respectively. The third and fourth terms,  $\hat{V}_{\text{elec.}}$  and  $\hat{V}_{\text{nucl.}}$ , indicates the electron-nucleus (Coulomb) attraction energies, while the fifth term,  $\hat{V}_{\text{elec.-nucl.}}$ , represent the kinetic energies of electrons and nuclei. Each Laplacian,  $\nabla_{\mathbf{r}_i}^2$  ( $\nabla_{\mathbf{R}_j}^2$ ), involves differentiation concerning the coordinates of the  $i^{\text{th}}$  electron ( $j^{\text{th}}$  nucleus).

## 2.2 From wave function methods to density functional theory

In practice, solving equation Eq. (2.2) analytically is achievable only for minimal systems due to the nature of the wave function, Eq. (2.3), that requires coordinates of all interacting particles. Consequently, several approximations have been extended to compute the ground-state energy, i.e., the minimum eigenvalue of  $\hat{H}$ , as well as energies of excited states, i.e., higher eigenvalues of  $\hat{H}$ .

### 2.2.1 Born-Oppenheimer approximation

The first step forward was the Born-Oppenheimer (adiabatic) approximation [23] which neglects the motion of much heavier and slower nuclei. Considering the mass of an electron is  $\simeq 1800$  times smaller than the mass of a proton. The nucleus-to-electron mass ratio increases for heavier particles. Therefore, the nucleus acts as a fixed external potential with zero kinetic energy from the prospect of a moving electron. The



Robert Oppenheimer

electrons in the first place keep the internal equilibrium and react to all external forces. Hence, the dynamics of nuclei and electrons can be decoupled, as it is appearing on different time scales. Such a simplistic argument vastly decreases the complexity of the wave function, Eq. (2.4), which displays a function of the electron positions only,

$$\psi \equiv \psi(\mathbf{r}_1, \mathbf{r}_2, \dots, \mathbf{r}_N) . \quad (2.5)$$

Consequently, the Hamiltonian operator, Eq. 2.4, takes the form

$$\begin{aligned} \hat{H} &= \hat{T}_{\text{elec.}}(\{\mathbf{r}_i\}_{i=1}^N) + \hat{V}_{\text{elec.}}(\{\mathbf{r}_i\}_{i=1}^N) + \hat{V}_{\text{ext.}}(\{\mathbf{r}_i\}_{i=1}^N, \{\mathbf{R}_j\}_{j=1}^M) = \\ &= -\frac{\hbar^2}{2} \sum_{i=1}^N \frac{\nabla_{\mathbf{r}_i}^2}{m} + \frac{1}{8\pi\epsilon_0} \sum_{\substack{i,i'=1 \\ i \neq i'}}^N \frac{e^2}{|\mathbf{r}_i - \mathbf{r}_{i'}|} + \\ &+ \hat{V}_{\text{ext.}}(\{\mathbf{r}_i\}_{i=1}^N, \{\mathbf{R}_j\}_{j=1}^M). \end{aligned} \quad (2.6)$$

The  $V_{\text{ext.}}$  term includes the electron-nucleus interaction, which can be described as the interaction of electrons with distinct external potential. In contrast, the universal first two terms in Eq. (2.6), the  $V_{\text{elec.}}$  term comprises all the material-specific information.

While the Born-Oppenheimer approximation simplified the Schrödinger equation (2.1) significantly, the solution for actual materials was still too costly due to the Coulombic electron-electron interactions.



Douglas R. Hartree

## 2.2.2 Hartree-Fock method

Among additional efforts to overcome the complexity of the many-body problem are the Hartree (1928) and the Hartree-Fock approximations (1930) [24]. Hartree offered an *ansatz* for the form of the electron wave function written as a product of single-electron wave functions,  $\phi_i(\mathbf{r}_i)$ ,  $i = 1, 2, \dots, N$ :

$$\psi(\mathbf{r}_1, \mathbf{r}_2, \dots, \mathbf{r}_N) \equiv \phi_1(\mathbf{r}_1)\phi_2(\mathbf{r}_2), \dots, \phi_N(\mathbf{r}_N). \quad (2.7)$$



Vladimir A. Fock

As a consequence, the Hamiltonian was decomposed into a sum of individual (non-interacting) Hamiltonians, one for each electron. In the Hartree's formulation, each electron identifies the others as a mean field, generate a replacement of the Coulombic electron-electron interaction by an effective (Hartree) potential from all other electrons. The total wave function describing the set of all

electrons is product of single-electron wave functions. Since the Hartree method neglects the electron-electron exchange interactions defined by the Pauli exclusion principle, the corresponding total energy,  $E = \sum_{i=1}^N$ , is overestimated. This problem is resolved by taking the many-body wave-function in a form of a single *Slater* determinant as:

$$\psi(\mathbf{x}_1, \mathbf{x}_2, \dots, \mathbf{x}_N) = \frac{1}{\sqrt{N!}} \begin{bmatrix} \phi_1(\mathbf{x}_1) & \cdots & \phi_1(\mathbf{x}_N) \\ \vdots & \ddots & \vdots \\ \phi_N(\mathbf{x}_1) & \cdots & \phi_N(\mathbf{x}_N) \end{bmatrix}. \quad (2.8)$$

where the variable  $\mathbf{x}$  includes both spatial,  $\mathbf{r}$ , and spin,  $\mathbf{s}$ , coordinates, and  $1/\sqrt{N!}$  represents a normalization factor of the  $N$ -electron system. The wave function (2.8) is antisymmetric, i.e., changes sign upon exchanging positions of two particles. Two electrons cannot occupy the same orbital (two equal rows in Eq. (2.8)) and the same point in the generalized space (two equal columns in Eq. (2.8)), as the Slater determinant is nullified in such a case.

The hypothesis of independent electrons and the initiation of an effective potential from the averaged potential, however, prohibit repulsive interaction between anti-parallel spin electrons emerging in the so-called correlation effects (demonstrated by the fact that two electrons cannot stay very close to each other due to the Coulomb repulsion) [25]. This leads to an overestimation of the total energies and band gaps. The Hartree-Fock approach is relatively suitable for systems with a small number of localized electrons. Still, it fails in perfect metals with completely delocalized electrons, as it omits the collective Coulomb screening.

### 2.2.3 Hohenberg-Kohn theorems

Against the Hartree and the Hartree-Fock approximations, the Density Functional Theory (DFT) synthesizes both exchange and correlation effects. Instead of the extremely sophisticated wave function (2.5), DFT considers the electronic charge density,  $n(\mathbf{r}) = n(x, y, z)$ , which is a function of only 3 variables. The total charge density according to an  $N$ -electron system can be written as the expectation value of the density operator,  $\hat{n}(\mathbf{r})$ ,

$$\begin{aligned} n(\mathbf{r}) &= \langle \psi | \hat{n}(\mathbf{r}) | \psi \rangle = \langle \psi | \sum_{i=1}^N \delta(\mathbf{r} - \mathbf{r}_i) | \psi \rangle \\ &= \sum_{i=1}^N \int \delta(\mathbf{r} - \mathbf{r}_i) |\psi(\mathbf{r}_1, \mathbf{r}_2, \dots, \mathbf{r}_N)|^2 d\mathbf{r}_1 d\mathbf{r}_2 \dots d\mathbf{r}_N \\ &= \sum_{i=1}^N \int |\psi(\mathbf{r}_1, \mathbf{r}_2, \dots, \mathbf{r}_i = \mathbf{r}, \dots, \mathbf{r}_N)|^2 d\mathbf{r}_1 d\mathbf{r}_2 \dots d\mathbf{r}_N, \end{aligned} \quad (2.9)$$



Pierre C. Hohenberg



Walter Kohn

where  $\delta$  denotes the Kronecker delta. DFT relies on two theorems introduced by Hohenberg and Kohn [26] in 1964, declaring that ground-state properties of atoms, molecules, and solids can be extracted from their total electronic charge density.

**H-K Theorem 1.** For any system of interacting particles in an external potential field,  $V_{\text{ext.}}(\mathbf{r})$ , the potential  $V_{\text{ext.}}(\mathbf{r})$  is determined uniquely—except for an additive constant by the ground-state particle density alone.

The H-K Theorem 1 claims one-to-one correspondence between the external potential and the ground-state electronic charge density. The ground-state wave function, accordingly, is also prepared. Hence, each likely wave function provides a unique charge density and vice versa; each possible charge density defines a unique Hamiltonian, hence, the dependent ground-state wave function. We note that Schrödinger equations with Hamiltonians  $\hat{H}$  and  $\hat{H}' = \hat{H} + c$ , where  $c$  is an arbitrary constant, will produce the same eigenfunctions and all the eigenenergies will only be shifted by  $c$ .

**H-K Theorem 2.** For any system of interacting particles defined by the charge density  $n(\mathbf{r})$ —in an external potential,  $V_{\text{ext.}}(\mathbf{r})$ , there is a total energy functional,

$$E[n(\mathbf{r})] = F_{\text{HK}}[n(\mathbf{r})] + V_{\text{ext.}}[n(\mathbf{r})] = F_{\text{HK}}[n(\mathbf{r})] + \int V_{\text{ext.}} n(\mathbf{r}) d\mathbf{r}, \quad (2.10)$$

where  $F_{\text{HK}}[n(\mathbf{r})]$  indicates a universal functional. The exact ground-state energy is the global minimum of  $E[n(\mathbf{r})]$  conditional to the constraint that the integral of  $E[n(\mathbf{r})]$  remains the total number of electrons in the system. The corresponding density is the exact ground-state density  $n_0(\mathbf{r})$ , meaning that

$$\left. \frac{\delta}{\delta n} E[n(\mathbf{r})] \right|_{n=n_0} = 0, \quad (2.11)$$

and

$$E_0 = E[n_0(\mathbf{r})]. \quad (2.12)$$

According to the H-K Theorem 2, the ground-state density can be prepared (up to an additive constant) by using the variational (Ritz) principle [27] represented by Eq. (2.11), i.e. as the global minimum of the total energy functional,  $E[n(\mathbf{r})]$ . This charge density also defines the exact ground-state energy.



Accurate evidence of Hohenberg-Kohn theorems can be found in the original paper [26]. Although the theorems developed the fundamental aspect of electronic structure problems, they still present (only) a variational principle method but no direct recipe for solving the many-body Schrödinger equation. Especially, no information about the so-called Hohenberg-Kohn functional,  $F_{\text{HK}}[n(\mathbf{r})]$ , is given, without the fact that it is universal, i.e. the same for all electron systems and independent of the external potential  $V_{\text{ext.}}(\mathbf{r})$ .

## 2.2.4 Kohn-Sham equations



Lu J. Sham

In 1965, Kohn and Sham [28] introduced a concept that enabled to turn of DFT into a real computational tool. The basic idea was to describe the physical system of many interacting electrons by a set of fictitious non-interacting particles in an external effective potential,  $V_{\text{eff.}}$ .

The *Kohn-Sham ansatz* ensures that the ground-state charge density of the fictitious non-interacting system is equal to that of the real interacting system.

**Kohn-Sham Ansatz.** There is an effective (Kohn-Sham) potential,  $\hat{V}_{\text{eff.}}$  for each system of interacting electrons in an external potential, yielding charge density

$$n(\mathbf{r}) = \sum_{i=1}^N |\phi_i(\mathbf{r})|^2,$$

equal to that of the interacting system. The (Kohn-Sham) orbitals,  $\phi_i(\mathbf{r})$ , obey the one particle Schrödinger-like equation

$$\underbrace{\left( -\frac{\hbar^2}{2m} \nabla^2 + \hat{V}_{\text{eff.}} \right)}_{\hat{H}_{\text{KS}}} \phi_i(\mathbf{r}) = E_i \phi_i(\mathbf{r}). \quad (2.13)$$

Alternately of solving Schrödinger equation for the  $N$ -electron wave function, the Kohn-Sham Ansatz states that it suffices to solve  $N$  single-electron Schrödinger-like equations (2.13) for a system with  $N$  independent (non-interacting) electrons which move in a potential that generated by the nuclei and the remaining electrons. The eigenvalues of the Kohn-Sham Hamiltonian,  $\hat{H}_{\text{KS}}$  in Eq. (2.13), do not represent real single-electron energies. Also, the Kohn-Sham orbitals,  $\phi_i$ , have no real physical meaning but have been shown to generate reasonable descriptions of real electronic band structures [29]. The only way to combine quantum-mechanical exchange and correlation effects is to include them in the effective potential term,  $\hat{V}_{\text{eff.}}$ , which is identical due to the second Hohenberg-

Kohn Theorem. According to Kohn and Sham,

$$V_{\text{eff.}} = V_{\text{ext.}}[n(\mathbf{r})] + V_{\text{H}}[n(\mathbf{r})] + V_{\text{xc}}[n(\mathbf{r})]. \quad (2.14)$$

The first term,  $V_{\text{ext.}}[n(\mathbf{r})]$ , indicates the external potential acting on the interacting system of electrons (e.g., the potential background from ions). The second term,  $V_{\text{H}}$ , is the Coulomb (a.k.a. Hartree) potential

$$V_{\text{H}} = \frac{1}{4\pi\epsilon_0} \int \frac{n(\mathbf{r}')}{|\mathbf{r} - \mathbf{r}'|} d\mathbf{r}', \quad (2.15)$$

while the last term,  $V_{\text{xc}}$ , called exchange-correlation potential, incorporates everything else to make  $V_{\text{eff.}}$  exact. The exchange-correlation potential contains the kinetic energy difference between the Coulomb interaction of electrons with the exchange-correlation hole as well as the real interaction and fictitious non-interacting systems. Going back to Eq. (2.10), the Hohenberg-Kohn functional,  $F_{\text{HK}}$ , takes the form

$$F_{\text{HK}}[n(\mathbf{r})] = T_0[n(\mathbf{r})] + V_{\text{H}}[n(\mathbf{r})] + V_{\text{xc}}[n(\mathbf{r})], \quad (2.16)$$

where the  $T_0[n(\mathbf{r})]$  denotes the kinetic energy of the non-interacting system.

The Kohn-Sham method, Eq. (2.13), Eq. (2.14), provides the exact theory and the correct charge density for any system by considering the exchange-correlation functional. The only approximation is the Born-Oppenheimer hypothesis of decoupled electronic and ionic dynamics. In practice, however, the  $V_{\text{xc}}[n(\mathbf{r})]$  term is unexplored and needs to be approximated too.

The Kohn-Sham equations Eq. (2.13) define a self-consistent problem and are usually solved by an iterative method. First, a trial charge density is used to compute the corresponding Kohn-Sham Hamiltonian,  $\hat{H}_{\text{KS}}$ . Then, the Kohn-Sham equations Eq. (2.13) are determined, and a new charge density is defined from the Kohn-Sham orbitals,  $\phi_i(\mathbf{r})$ , and applied to construct the Kohn-Sham Hamiltonian again. The scheme is repeated until arriving convergence within a designated accuracy.

## 2.2.5 The exchange-correlation potential

The exchange-correlation potential,  $V_{\text{xc}}$  in Eq. (2.14), contains the energy difference between the physical system of interacting electrons and the auxiliary non-interacting system.  $V_{\text{xc}}$  can be calculated as a functional derivative of the exchange-correlation energy,  $E_{\text{xc}}$ , with considering the local density,  $n(\mathbf{r})$ ,

$$V_{\text{xc}}[n(\mathbf{r})] = \frac{\delta E_{\text{xc}}[n(\mathbf{r})]}{\delta n(\mathbf{r})}. \quad (2.17)$$

When considering homogeneous electron gas,  $V_{xc}$  depends only on the value of the density. For non-homogeneous systems, however,  $V_{xc}$  generally depends also on the derivatives of the charge density, leading to

$$V_{xc}[n(\mathbf{r})] = \int V_{xc}(n(\mathbf{r}), \nabla n(\mathbf{r}), \nabla(\nabla n(\mathbf{r})), \dots), n(\mathbf{r}) d\mathbf{r}. \quad (2.18)$$

In what follows, the most popularly applied approximations for the exchange-correlation potential will be described.

## 2.2.6 Local density approximation (LDA)

The Local Density Approximation (LDA) was firstly introduced in 1965, in the original work by Kohn and Sham [28] who assumed the so-called jellium model, i.e. a homogeneous electron gas with electrons evenly distributed in a uniform positive external potential. Consequently, the exchange-correlation energy functional,  $E_{xc}[n(\mathbf{r})]$  in Eq. (2.17), reads [25]

$$E_{xc}^{\text{LDA}}[n(\mathbf{r})] = E_x^{\text{LDA}}[n(\mathbf{r})] + E_c^{\text{LDA}}[n(\mathbf{r})] = \int \varepsilon_{xc}^{\text{LDA}}(n(\mathbf{r}))n(\mathbf{r})d\mathbf{r}, \quad (2.19)$$

wherein  $\varepsilon_{xc}^{\text{LDA}}(n(\mathbf{r}))$  is the exchange-correlation energy of each particle of a single electron in a uniform electron gas with the density  $n(\mathbf{r})$ . Furthermore,  $\varepsilon_{xc}^{\text{LDA}}(n(\mathbf{r}))$  can be expressed as a sum of the exchange energy density,  $\varepsilon_x^{\text{LDA}}(n(\mathbf{r}))$ , and the correlation energy density,  $\varepsilon_c^{\text{LDA}}(n(\mathbf{r}))$ ,

$$\varepsilon_{xc}^{\text{LDA}}(n(\mathbf{r})) = \varepsilon_x^{\text{LDA}}(n(\mathbf{r})) + \varepsilon_c^{\text{LDA}}(n(\mathbf{r})). \quad (2.20)$$

Employing the Hartree-Fock approximation for homogeneous electron gas yields the exchange part,  $\varepsilon_c^{\text{LDA}}(n(\mathbf{r})) = -Cn^{1/3}(\mathbf{r})$  [28, 30], and hence

$$E_x^{\text{LDA}}[n(\mathbf{r})] = \underbrace{-\frac{3}{4}\left(\frac{3}{\pi}\right)^{1/3}}_C \int n^{4/3}(\mathbf{r})d\mathbf{r}. \quad (2.21)$$

Although the correlation part,  $\varepsilon_c^{\text{LDA}}(n(\mathbf{r}))$ , comes more challenging to display in an analytic form, it was parametrized by e.g. Ceperley and Alder [31] via quantum Monte-Carlo calculations. From the definition, LDA presents a good explanation for systems possessing rather a uniform charge density, e.g., nearly free electron metals. LDA also works pretty well for semiconductors, molecules, and ionic crystals but breaks once the charge density changes distinctly, such as in the case of highly localized charge density distribution. LDA disesteems band gaps and exceeds binding, which leads to generally lower lattice parameters (bond lengths) compared to experimental values [25].

## 2.2.7 Generalized gradient approximation (GGA)



John P. Perdew

Very complex potential landscapes around electrons characterize most real systems, therefore non-homogeneous charge density, calling for further improvement of the simplistic LDA approach. Already Kohn and Sham regarded that the charge density gradient,  $\nabla n(\mathbf{r})$ , is important to get a better view of the exchange-correlation energy. In the 1990s, Perdew, and co-workers [32, 33] made a real breakthrough by proposing the Generalized Gradient Approximation (GGA), in which the exchange-correlation energy reads

$$E_{\text{xc}}^{\text{GGA}}[n(\mathbf{r})] = \int \varepsilon_{\text{xc}}^{\text{GGA}}(n(\mathbf{r}), \nabla n(\mathbf{r})) n(\mathbf{r}) d\mathbf{r} = \int \varepsilon_{\text{xc}}^{\text{GGA}}(n(\mathbf{r})) F_{\text{xc}}(n(\mathbf{r}), \nabla n(\mathbf{r})) n(\mathbf{r}) d\mathbf{r}. \quad (2.22)$$

GGA exchange-correlation energy functionals produce plenty of results for many systems but underestimate binding, systematically, hence overestimate bond lengths. Similarly to LDA, GGA underestimates band gaps [25, 34]. To overcome this limitation, the so-called meta-GGA (MGGA) approach—adding more semi-local information than GGA have been developed [34]. MGGA also respects higher-order density gradients or includes the kinetic energy density, which contains derivatives of the occupied Kohn-Sham orbitals. Another approach is hybrid exchange-correlation functionals, connecting the Hartree-Fock and GGA method advantages, as their systematic errors partially cancel out [25]. Unlike GGA, the Hartree-Fock method yields smaller bond lengths, larger binding energy, and wider band gaps. Since Hartree and Fock omitted correlation effects, hybrid functionals include full GGA-type correlation, while the exchange part is some mixture of the exact Hartree-Fock exchange (often  $\simeq 25\%$ ) and a GGA-type exchange [25, 35].

## 2.2.8 Basis wave functions

For a practical implementation of DFT, it is important to expand the Kohn-Sham orbitals,  $\phi_i(\mathbf{r})$  in Eq. (2.13), in a reasonable basis,  $\phi_p^{\text{basis}}(\mathbf{r})$ ,

$$\phi_i(\mathbf{r}) = \sum_{p=1}^P c_p^i \phi_p^{\text{basis}}(\mathbf{r}), \quad (2.23)$$

where  $c_p^i$  are constant coefficients. Accordingly, the Kohn-Sham equations are equal to the system of linear equations [36]

$$\underbrace{\begin{pmatrix} \dots & \dots & \dots \\ \vdots & \langle \phi_j^{\text{basis}} | \hat{H}_{\text{KS}} | \phi_k^{\text{basis}} \rangle - E_i \langle \phi_j^{\text{basis}} | \phi_k^{\text{basis}} \rangle & \vdots \\ \dots & \dots & \dots \end{pmatrix}}_H \begin{pmatrix} c_1^i \\ \vdots \\ c_P^i \end{pmatrix} = \begin{pmatrix} 0 \\ \vdots \\ 0 \end{pmatrix}. \quad (2.24)$$

Diagonalisation of the matrix  $H$  produces  $P$  sets of coefficients  $c_p^i$  and  $P$  eigenvalues. In principle, the function space where the eigenfunctions  $\phi_i(\mathbf{r})$  belong to is infinite-dimensional; hence  $P$  is infinite. For practical reasons, however,  $P$  requires to be truncated because the actual size of the basis set influences the accuracy of the solution, directly. Suitable basis wave functions can reduce the value of  $P$  required for the designated accuracy. The linear combination of atomic orbitals (LCAO) [37], orthogonalized plane waves method (OPW) [38], and projector augmented plane waves (PAW) [39] are the most popular ones include. In this thesis, the last-mentioned PAW method was applied. The advantage of plane waves is their orthogonality, largely simplifying terms of type  $E_i \langle \phi_j^{\text{basis}} | \phi_k^{\text{basis}} \rangle$  matrix equation (2.24), and their simplistic analytical form.

## 2.2.9 Periodic boundary conditions

Extended systems with too many atoms, such as bulk materials or surfaces, could be computationally treatable. Consequently, an important feature is crystal periodicity that allows using supercells consisting of several unit cells to approximate the intended system. Following periodic boundary conditions, the Bloch Theorem [25, 40], ensures that defining wave functions inside a unit cell (supercell) is enough to explain the infinite periodic system since wave functions outside this limited region only vary by a phase factor. Following the Bloch Theorem, each Kohn-Sham eigenfunction in a periodic solid can be denoted as a product of a plane wave,  $e^{i\mathbf{k}\mathbf{r}}$  with a wave vector  $\mathbf{k}$  from the first Brillouin zone, and a lattice-periodic function,

$$\phi_{n,\mathbf{k}}(\mathbf{r}) = e^{i\mathbf{k}\mathbf{r}} u_{n,\mathbf{k}}(\mathbf{r}). \quad (2.25)$$

In the above, the band index,  $n$ , label the wave functions for a given  $\mathbf{k}$ . This means that a wave vector labels each plane wave,  $\mathbf{k}$ , i.e., a triplet of  $(k_1, k_2, k_3)$ . Applying a Fourier expansion of  $u_{n,\mathbf{k}}(\mathbf{r})$  with respect to the reciprocal lattice vectors,  $\mathbf{G}$ , leads to

$$\phi_{n,\mathbf{k}}(\mathbf{r}) = e^{i\mathbf{k}\mathbf{r}} \sum_{\mathbf{G}} c_{n,\mathbf{k}}^{\mathbf{G}} e^{i\mathbf{G}\mathbf{r}} = \sum_{\mathbf{G}} c_{n,\mathbf{k}}^{\mathbf{G}} e^{i(\mathbf{K}+\mathbf{G})\mathbf{r}}, \quad (2.26)$$

where  $c_{n,\mathbf{k}}^{\mathbf{G}}$  are (complex) expansion coefficients that require to be determined. In principle, wave functions for electrons inside a unit cell should be calculated at infinite number of  $\mathbf{k}$ -points in the corresponding reciprocal unit cell. For practical reasons, however, only a finite number of  $\mathbf{k}$ -points, i.e. a certain  $\mathbf{k}$ -point mesh is assumed [25].

As already discussed, a formally exact description of the electronic wave functions needs an infinite basis set. In reality, only a limited number of plane waves can be taken into account. The basis set size is conventionally connected to the kinetic energy of a plane wave

$$E = \frac{\hbar^2 |\mathbf{k} + \mathbf{G}|^2}{2m}. \quad (2.27)$$

Concerning the ground-state properties, lower-energy plane waves probably provide more to the solution sought than the higher-energy ones. Therefore, a cut-off energy

$$E = \frac{\hbar^2 |\mathbf{k}_{\text{cut}}|^2}{2m}. \quad (2.28)$$

can be determined and only plane waves with  $|\mathbf{k} + \mathbf{G}| < \mathbf{k}_{\text{cut}}$  are used in the expansion Eq. (2.26). Obviously, the higher the  $E_{\text{cut}}$  value, the larger wave function basis is generated, directly affecting the quality of the solution.

### 2.2.10 Pseudopotentials

The wave function expansion into plane waves, Eq. (2.26), demands a large number of plane waves in the core region where there are rapid oscillations by the diverging potential. Since oscillations are computationally very expensive to represent, the *pseudopotential* method efficiently can reduce the core electrons tightly bonded. They are highly localized in the close environment of atomic nuclei and no significant participation in chemical bonding. Pseudopotentials are formed to generate artificial nodeless wave functions in the nucleus and core electron region while replicating the valence electron states (only) outside of a given radius. Due to that, the more wave functions from the core as a valence state, a more accurate pseudopotential can be generated; nevertheless, this can significantly raise computational costs. The already mentioned projector augmented plane waves (PAW) [39] connects both the pseudopotential and the all-electron methods. Applying the frozen core approximation to the core region's wave function achieves the accuracy of all electron methods. While actual valence wave functions with actual nodes near nuclei can be obtained, then it gives accurate calculations of the optical and magnetic properties possible while retaining the capability of the pseudopotential method [25, 36].

### 2.2.11 Muffin-tin orbitals

The muffin-tin spheres divide the crystal into two parts, one is the region surrounded by the atomic sites and the other one is the interstitial region outside of the mentioned spheres. Inside the muffin-tin spheres (the spheres never touch each other) with radius  $S_{\text{muffin-tin}}$ , the potential,  $V_{\text{muffin-tin}}$ , is assumed to be spherically symmetric, while for the interstitial region is considered approximately constant,  $V_I$ . Without loss of generality, the potential in the interstitial region can be set to zero. In this relation, the potential of a single muffin-tin well for a crystal with one atom is written by:

$$V_{\text{muffin-tin}}(\mathbf{r}) = \begin{cases} V(\mathbf{r}) - V_I & , \text{ if } |\mathbf{r}| < S_{\text{muffin-tin}} , \\ 0 & , \text{ if } |\mathbf{r}| > S_{\text{muffin-tin}} , \end{cases} \quad (2.29)$$

where,  $V(\mathbf{r})$  is the spherically symmetric part of the crystal potential. Now, the Schrödinger equation (2.13) can be written as:

$$\left[ -\frac{\hbar^2}{2m}\nabla^2 + V_{\text{muffin-tin}} \right] \phi_i(\mathbf{r}) = (E_i - V_I)\phi_i(\mathbf{r}). \quad (2.30)$$

## 2.3 Structural stability

Inside the useful part of this thesis, a material's structural stability was evaluated on three levels, containing chemical, mechanical, and dynamical (vibrational, phonon) stability. Theoretical concepts can be found in any standard textbook of solid state physics, e.g., Kittel and McEuen [41].

### 2.3.1 Chemical stability

The energy of formation,  $E_f$ , which explain chemical stability, represents the energy absorbed or released when combining particles from an infinite pool into a complex structure,

$$E_f = \frac{1}{\sum_s n_s} \left( E_{\text{tot}} - \sum_s n_s \mu_s \right). \quad (2.31)$$

where,  $E_{\text{tot}}$  is the total energy of the cell,  $\mu_s$  and  $n_s$  are the chemical potential and the number of atoms, respectively, of the element  $s$  (e.g. Ti, Al or Mo). The chemical potential,  $\mu_s$ , is conventionally approximated by the total energy per atom of the ground state of the element  $s$ , e.g.  $\mu_{\text{Al}} \equiv E_{\text{tot}}^{\text{fcc-Al}}$ ,  $\mu_{\text{Ti}} \equiv E_{\text{tot}}^{\text{hcp-Ti}}$  or  $\mu_{\text{Mo}} \equiv E_{\text{tot}}^{\text{bcc-Mo}}$ . The negative formation energy,  $E_f$  [42, 43] means the structure is chemically stable.

### 2.3.2 Mechanical stability

Certain strain energy can be expected by any deformation which can bring material from its equilibrium characterized by equilibrium energy  $E_0$  and the volume  $V_0$  to a

higher-energy (deformed) state. For instance, the strain energy,  $E(\varepsilon)$ , of a homogeneous deformation by an infinitesimal strain, can be Taylor-expanded around the equilibrium configuration and approximated by a quadratic function of all the independent deformation parameters, i.e. the strain components  $\varepsilon_{ij}$ . This quadratic approximation of the strain energy is valid for sufficiently small strains, which is known as harmonic elasticity,

$$\begin{aligned}
E(\varepsilon) &= \underbrace{E_0}_A + V_0 \sum_{i,j=1}^3 \underbrace{\frac{\partial E}{\partial \varepsilon_{ij}} \Big|_{V_0}}_{B_{ij}} \varepsilon_{ij} + \frac{1}{2} V_0 \sum_{i,j,k,l=1}^3 \underbrace{\frac{\partial^2 E}{\partial \varepsilon_{ij} \partial \varepsilon_{kl}} \Big|_{V_0}}_{C_{ijkl}} \varepsilon_{ij} \varepsilon_{kl} + O(\varepsilon^3) = \\
&= A + V_0 \sum_{i,j=1}^3 B_{ij} \varepsilon_{ij} + \frac{1}{2} V_0 \sum_{i,j,k,l=1}^3 C_{ijkl} \varepsilon_{ij} \varepsilon_{kl} = \\
&= \frac{1}{2} V_0 \sum_{i,j,k,l=1}^3 C_{ijkl} \varepsilon_{ij} \varepsilon_{kl}
\end{aligned} \tag{2.32}$$

The harmonic approximation is granted for the previous equation. As all strains are zero in equilibrium, the intended strain energy is set to zero ( $E_0 \equiv A \equiv 0$ ). The first derivatives of the strain energy are zero ( $B_{ij} \equiv 0$ ), because the Taylor expansion is done nearby equilibrium configuration. The theory of linear elasticity cancels the higher-order derivatives ( $O(\varepsilon^3) \equiv 0$ ). In Eq. (2.32),  $C_{ijkl}$  is the 4-rank elastic tensor, having generally 81 independent components. Imposing the symmetry requirement,  $C_{ijkl} = C_{jikl} = C_{ijlk}$ , together with the rule of exchanging partial derivatives,  $C_{ijkl} = C_{klij}$ , the number of independent components decreases to 21. Furthermore, applying a mapping that gets a pair of Cartesian indices inside a single integer (Voigt's notation)

$$11 \mapsto 1; \quad 22 \mapsto 2; \quad 33 \mapsto 3; \quad 23 \mapsto 4; \quad 13 \mapsto 5; \quad 12 \mapsto 6, \tag{2.33}$$

the quadratic form of Eq. (2.32) reads

$$E(\varepsilon) = \frac{1}{2} V_0 \sum_{i,j=1}^6 C_{ij} \varepsilon_i \varepsilon_j \tag{2.34}$$

Lastly, in the lack of external loads, the material is stable; while within the harmonic approximation if and only if for all non-zero strains its elastic energy given by Eq. (2.34) is positive. As  $C_{ij}$  (in the Voigt's notation) is a  $6 \times 6$  matrix, this is equivalent to the following necessary and enough mechanical stability conditions [44],

- (I) the matrix  $\mathbb{C}$  is positive definite,
- (II) all eigenvalues of  $\mathbb{C}$  are positive,



(III) all leading principal minors of  $\mathbb{C}$  are positive.

These conditions hold regardless of the crystal symmetry. The simplest form of (I) is for cubic systems

$$C_{11} - C_{12} > 0, \quad C_{11} + 2C_{12} > 0 \quad C_{44} > 0, \quad (2.35)$$

known as the *Born stability criterion* [44, 45].

## 2.4 The elastic properties of crystals

DFT allows a parameter-free approach for assessing mechanical properties at the atomic level from single-crystal elastic constants. Keeping the notation of Section 2.3.2 together with the assumption of harmonic elasticity, second-order elastic constants,  $C_{ij}$ , can be described as the coefficients of proportionality between the stresses,  $\sigma_i$ , of the material and the macroscopic strains,  $\varepsilon_j$ , acting on the material. This relationship is known as the Hooke's law, which in components reads

$$\sigma_i = \sum_{j=1}^6 C_{ij}\varepsilon_j, \quad (i = 1, 2, \dots, 6) \quad (2.36)$$

Equation (2.36) considers the earlier introduced Voigt's notation Eq. (2.33). Therefore, the elastic (stiffness) matrix,  $C_{ij}$  has size  $6 \times 6$  and it is symmetric, consequently contains 21 independent elements. The crystal class of the material in question dictates additional symmetry requirements that further decrease independent elastic constants [44]. Specifically, the elastic response of material with cubic symmetry is fully characterized by three independent elastic constants,  $C_{11}, C_{12}, C_{44}$ , while the corresponding elastic matrix reads

$$C_{ij}^{\text{cubic}} = \begin{pmatrix} C_{11} & C_{12} & C_{12} & 0 & 0 & 0 \\ C_{12} & C_{11} & C_{12} & 0 & 0 & 0 \\ C_{12} & C_{12} & C_{11} & 0 & 0 & 0 \\ 0 & 0 & 0 & C_{44} & 0 & 0 \\ 0 & 0 & 0 & 0 & C_{44} & 0 \\ 0 & 0 & 0 & 0 & 0 & C_{44} \end{pmatrix}. \quad (2.37)$$

And hexagonal crystal system with 5 independent elastic constants:

$$C_{ij}^{\text{hexagonal}} = \begin{pmatrix} C_{11} & C_{12} & C_{13} & 0 & 0 & 0 \\ C_{12} & C_{11} & C_{13} & 0 & 0 & 0 \\ C_{13} & C_{13} & C_{11} & 0 & 0 & 0 \\ 0 & 0 & 0 & C_{44} & 0 & 0 \\ 0 & 0 & 0 & 0 & C_{44} & 0 \\ 0 & 0 & 0 & 0 & 0 & C_{66} \end{pmatrix} \quad (2.38)$$

with  $C_{66} = (C_{11} - C_{12})/2$  [44].

Two different methods are available to calculate elastic constants from first principles. The energy-strain method extracts  $C_{ij}$  directly from the variation of the strain energy,  $E$ , of the system with strain according to the already derived Eq. (2.34), i.e.  $E(\varepsilon) = \frac{1}{2}V_0 \sum_{i,j=1}^6 C_{ij}\varepsilon_i\varepsilon_j$

Based on the Hooke's law (2.36), the stress-strain method uses directly the variation of stresses with the applied strain, as given by  $\sigma_i = \sum_{j=1}^6 C_{ij}\varepsilon_j$ . As shown by Caro, Schulz, and O'Reilly [46], the stress-strain method is more robust. It converges faster than the energy-strain approach concerning the number of plane waves in the basis set and the number of  $k$ -points sampling the reciprocal space [47].

### 2.4.1 Single crystalline Young's modulus

The directional dependence of Young's modulus,  $E_{hkl}$ , can be related to the elastic compliances  $(S_{ij}) = (C_{ij})^{-1}$ .

For a cubic structure, the directional Young's modulus is [48]:

$$\frac{1}{E_{hkl}} = S_{11} - 2 \left( S_{11} - S_{12} - \frac{1}{2}S_{44} \right) (l_1^2 l_2^2 + l_2^2 l_3^2 + l_1^2 l_3^2) \quad (2.39)$$

where  $l_1$ ,  $l_2$  and  $l_3$  are the directional cosines of the direction  $[hkl]$ .

Equation (2.39) simplifies for the three low-index cubic directions into:

$$\frac{1}{E_{100}} = S_{11} , \quad (2.40)$$

$$\frac{1}{E_{110}} = S_{11} - \frac{1}{2} \left( S_{11} - S_{12} - \frac{1}{2}S_{44} \right) , \quad (2.41)$$

$$\frac{1}{E_{111}} = S_{11} - \frac{2}{3} \left( S_{11} - S_{12} - \frac{1}{2}S_{44} \right) . \quad (2.42)$$

Similarly, for hexagonal phases one gets [48]:

$$\frac{1}{E_{hkl}} = (1 - l_3^2)S_{11} + l_3^4 S_{33} + l_3^2(1 - l_3^2)(2S_{13} + S_{44}) \quad (2.43)$$

where the Eq. (2.43) yields:

$$\frac{1}{E_{2\bar{1}\bar{1}0}} = \frac{1}{E_{100}} = S_{11} , \quad (2.44)$$

$$\frac{1}{E_{0001}} = \frac{1}{E_{001}} = S_{33} . \quad (2.45)$$

## 2.5 Polycrystalline bulk, shear, and Young's modulus

From the obtained  $C_{ij}$  of a single crystal, polycrystalline bulk modulus,  $B$ , and shear modulus,  $G$ , are defined as:

$$B = \frac{B_V + B_R}{2} , \quad (2.46)$$

$$G = \frac{G_V + G_R}{2} , \quad (2.47)$$

where the  $B_V$ ,  $G_V$ , and  $B_R$ ,  $G_R$  are Voigt's and Reuss's bulk and shear modulus respectively.

For a cubic system with  $C_{11}, C_{12}$  and  $C_{44}$  elastic constants:

$$B_V = B_R = \frac{C_{11} + 2C_{12}}{3} , \quad (2.48)$$

$$G_V = \frac{C_{11} - C_{12} + 3C_{44}}{5} , \quad (2.49)$$

$$G_R = \frac{5(C_{11} - C_{12})C_{44}}{3(C_{11} - C_{12} + 4C_{44})} . \quad (2.50)$$

On the other hand, for hexagonal structures the numbers of independent single-crystal elastic constant are five ( $C_{11}$ ,  $C_{12}$ ,  $C_{13}$ ,  $C_{66}$  and  $C_{33}$ ), the Voigt's, Reuss's bulk and shear modulus are given by

$$B_V = \frac{2C_{11} + 2C_{12} + 4C_{13} + C_{33}}{9} , \quad (2.51)$$

$$B_R = \frac{(C_{11} + C_{12})C_{33} - 2C_{13}^2}{C_{11} + C_{12} - 4C_{13} + 2C_{33}} , \quad (2.52)$$

$$G_V = \frac{C_{11} + C_{12} - 4C_{13} + 2C_{33} + C_{44} + 12C_{66}}{30} , \quad (2.53)$$

$$G_R = \frac{5[(C_{11} + C_{12})C_{33} - 2C_{13}^2]C_{44}C_{66}}{6B_V C_{44} C_{66} + 2[(C_{11} + C_{12})C_{33} - 2C_{13}^2](C_{44} + C_{66})} , \quad (2.54)$$

with

$$C_{66} = \frac{C_{11} - C_{12}}{2} . \quad (2.55)$$

Polycrystalline Young's modulus,  $E$ , is calculated as:

$$E = \frac{9BG}{3B + G} . \quad (2.56)$$

## 2.6 Quasi-harmonic approximation (QHA)

Recently, phonopy [49] has become one of the most used tools in the computational material science field. The quasi-harmonic approximation (QHA) is implemented in it to calculate some thermal properties, e.g., thermal expansion or heat capacity. However, in the there implemented approach, the temperature has no direct effect on the unit cell geometry such as  $c/a$  and  $b/a$  ratios or the lattice angles [50]. Since the main application field of the TiAl-based alloys is at high temperatures, accurate knowledge of temperature dependencies of structural and thermodynamic properties, i.e., thermal expansion coefficient (TEC) is of crucial importance[51, 52].

As a counterpart to the experimentally estimated values of TEC [53–58], first principles quantum-mechanical methods were used to predict the thermal expansion properties of  $\gamma$ -TiAl alloys [59]. Nonetheless, comparing the result of Fu *et al.* [59] and He *et al.* [58], the thus revealed discrepancies call for improved implementation of the QHA to determine TEC for  $\alpha_2$ -Ti<sub>3</sub>Al (hexagonal) and  $\gamma$ -TiAl (tetragonal) phases.

### 2.6.1 The used concepts

Note: This section is a part of an own publication [50].

Structural optimization includes the evaluation of total energies at various volumes. Full relaxation including the unit cell shape and internal atomic coordinates optimization was performed for every volume, yielding lattice parameters  $a_0^\xi(V)$  and  $c_0^\xi(V)$  ( $\xi = \gamma$  or  $\alpha_2$ ) as functions of volume at 0 K.

Thermal properties were evaluated within the quasi-harmonic approximation (QHA) using the phonopy code [49, 60]. The phonon frequencies were calculated for 6 evenly spaced volumes in the range 15.4–17.4 Å<sup>3</sup>/at. ( $\gamma$ -phase) and 6 volumes in the range 15.8–17.9 Å<sup>3</sup>/at. ( $\alpha_2$ -phase) employing  $3 \times 3 \times 3$  (54 atoms) and  $2 \times 2 \times 2$  (64 atoms) supercells, respectively.

Assuming that the  $c/a$  ratio is only a function of volume and not temperature, the resulting temperature dependence of volume  $V^\xi(T)$  as obtained from the QHA (phonopy-qha package) allows to determine also the temperature dependencies of individual lattice

constants  $x^\xi(T)$ ,  $x = a, c$  and  $\xi = \gamma, \alpha_2$ , as:

$$x^\xi(T) = x_0^\xi(V(T)) . \quad (2.57)$$

This treatment is in Chap. 6 termed as ‘ground state optimized cell shape’ (gs-cs).

To probe the validity of the assumption that the  $c/a$  is only a function of volume independent of temperature, we have adopted additional scheme. For every volume, we selected 5  $c/a$  ratios around the GGA-PBE equilibrium values ( $(c/a)_\gamma^{\text{GGA-PBE}} = 1.018$ ,  $(c/a)_{\alpha_2}^{\text{GGA-PBE}} = 0.809$ ). For each of these static configurations, thermodynamic properties within the harmonic approximation (phonopy package) were calculated, hence yielding vibrational Helmholtz free energies  $F_{\text{vib}}(T, V, c/a)$ . The total Helmholtz free energy,  $F$ , was constructed by adding the 0 K total energies:

$$F(T, V, c/a) = E_{\text{tot}}(V, c/a) + F_{\text{vib}}(T, V, c/a) . \quad (2.58)$$

The equilibrium geometry at a fixed temperature  $T$  was then calculated by two-step fitting. First, we estimated

$$F(T, V) = \min_{c/a} F(T, V, c/a) \quad (2.59)$$

by fitting the  $F(T = \text{const.}, V = \text{const.}, c/a)$  data with a second order polynomial. Subsequently, the  $F(T, V)$  data were fitted with the Birch–Murnaghan equation of state [61] to obtain the equilibrium volume  $V_0(T)$  (in addition to free energy,  $F(T)$ , bulk modulus,  $B(T)$ , and pressure derivative of bulk modulus,  $B'(T)$ ). Finally, the  $(c/a)(T = \text{const.}, V)$  data minimising  $F(T = \text{const.}, V, c/a)$  in Eq. (2.59), were linearly interpolated as a function of  $V$ , and the equilibrium value at temperature  $T$  was estimated from this linear fit at  $V = V_0(T)$ . This procedure allows to decouple the influence of temperature and pressure (volume) on the cell geometry and in the Chap. 6 is thus termed ‘temperature optimized cell shape’ (to-cs) approach.

The thermal expansion coefficients were calculated from the estimated lattice parameters as:

$$\alpha_x^\xi(T) = \frac{1}{x_{\xi(T)}} \frac{dx_\xi}{dT} \approx \frac{1}{x_{\xi(T)}} \frac{x_\xi(T + \Delta T) - x_\xi(T - \Delta T)}{2\Delta T} . \quad (2.60)$$

Finally, the heat capacity at constant (ambient) pressure,  $C_p$ , was estimated from the Helmholtz free energy,  $F^\xi(T)$ , as

$$C_p(T) = -T \frac{\partial^2 F(T)}{\partial T^2} \approx -T \frac{F(T + \Delta T) + F(T - \Delta T) - 2F(T)}{(\Delta T)^2} \quad (2.61)$$

The latter expressions in Eqs. (2.60) and (2.61) represent numerical derivatives as both, lattice constants and Helmholtz free energy were calculated on a discrete set of temperatures from 0 to 1000 K with a step of 10 K.

## Simulation setup

### 3.1 Structural models

#### 3.1.1 Phases with composition $\text{Ti}_{0.5}\text{Al}_{0.5}$

In the present thesis, several different TiAl structures were considered for investigation. Their overview is shown in this section. Those include eight TiAl-based structures, namely  $\alpha_2$ -Ti<sub>3</sub>Al,  $\alpha'_2$ -TiAl,  $\alpha'$ -TiAl,  $\beta_o$ -TiAl,  $\beta$ -TiAl,  $\gamma$ -TiAl,  $\gamma_{\text{dis}}$ -TiAl and B19-TiAl (Table 3.1).

The chemical disorder is modeled with supercells having optimized short range order pair correlation functions, often referred to as Special Quasi-random Structures (SQSs) [62]. They were generated with our own code `sqsgenerator` [63].

A conventional bcc cell  $\beta$  was used to construct  $3 \times 3 \times 3$  supercells containing 54 atoms which represent the disordered  $\beta$ -TiAl phase ( $\text{Ti}_{0.5}\text{Al}_{0.5}$ ) (see Fig. 3.1a). From the perspective as to how to distribute atoms among the lattice sites (in the supercell for the SQS approach or the unit cell for the CPA), this structure has only 1 sublattice (all lattice sites are equivalent), see Fig. 3.1a). The same supercell size was used also for modeling its ordered variant,  $\beta_o$ -TiAl, based on the B2 unit cell (space group nr. 221 ( $Pm\bar{3}m$ ), Fig. 3.1b)). In contrast to the  $\beta$  phase, the ordered- $\beta_o$  structure has two sublattices. In their perfect state, these two sublattices are fully populated with Ti and Al atoms, respectively. Therefore, Mo may occupy any of these sublattices. Assuming a direct substitution, this leads to what is further on referred to as Ti-rich compositions,  $\text{Ti}_{0.5}\text{Al}_{0.5-x}\text{Mo}_x$  or Al-rich compositions,  $\text{Ti}_{0.5-x}\text{Al}_{0.5}\text{Mo}_x$ . Obviously, the same compositions (and hence terminology) are allowed also for the disordered  $\beta$  phase in which all three elements occupy the same sublattice. The structural studies are complemented also with discussing compositional trends of the stable  $\text{Ti}_{0.5}\text{Al}_{0.5}$  intermetallic phase, the conventional slightly-tetragonal  $\gamma$ -TiAl ( $L1_0$ , space group nr. 123 ( $P4/mmm$ )) and its

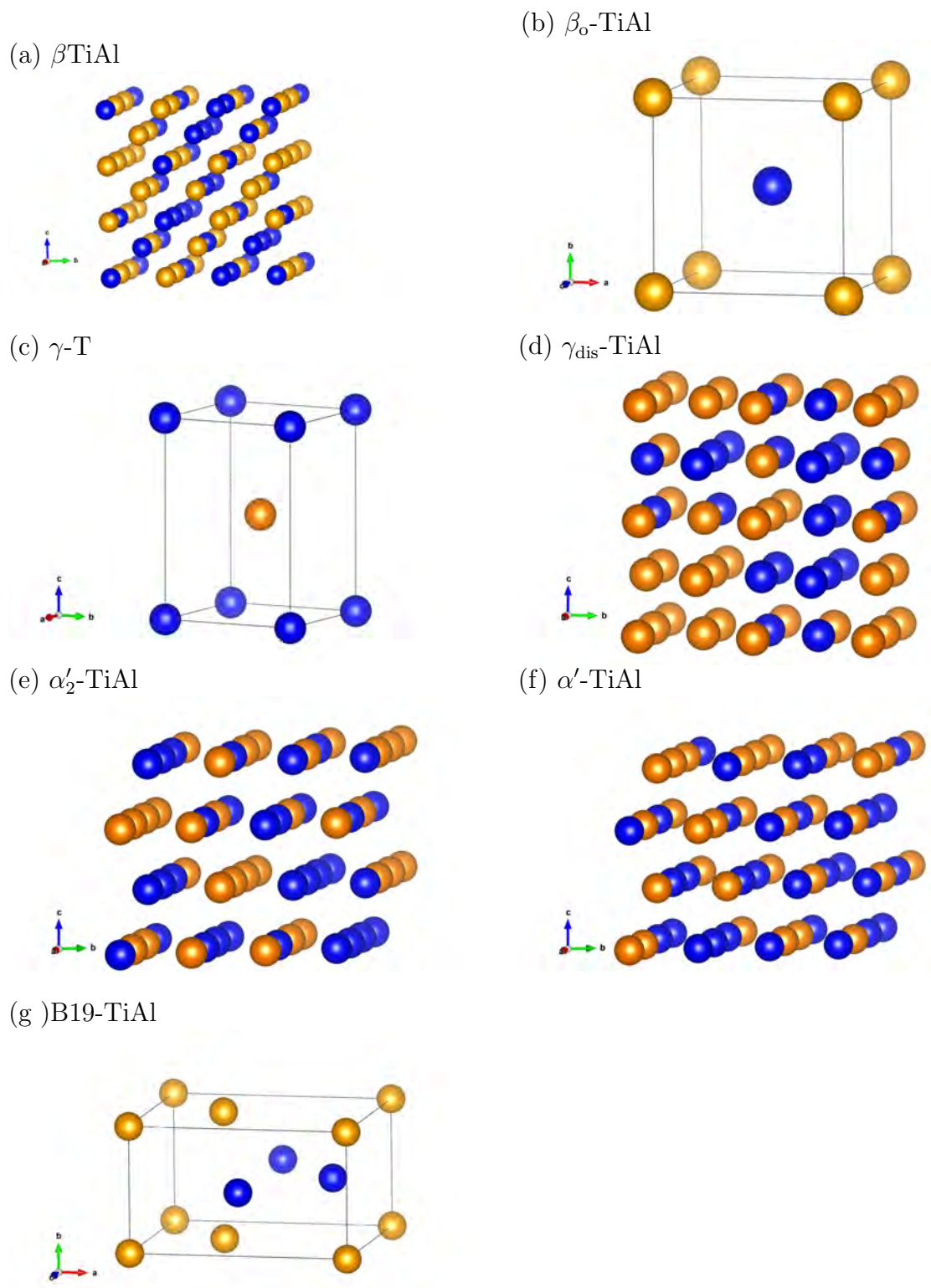


Figure 3.1: Visualization of the atomic arrangements of the studied phases in simulation boxes.

hypothetical disordered counterpart,  $\gamma_{\text{dis}}$  (A1, space group nr 225 ( $Fm\bar{3}m$ )). The unitcell of  $\gamma$ -TiAl can be reduced to a body-centered tetragonal (bct) structure shown in Fig. 3.1c. Both  $\gamma_{\text{dis}}$  and Mo-alloyed  $\gamma$  phases were modeled as  $2 \times 2 \times 2$  multiple of a 4-atom conventional fcc/ $\gamma$ -TiAl cell leading to 32 atomic supercells (see  $\gamma_{\text{dis}}$  in Fig. 3.1d) [14]. Again, the Ti-rich and Al-rich terminology for Mo-alloyed systems is used with the same meaning as for the  $\beta_o/\beta$  structures.

Regarding the hexagonal counterparts for the martensitic transformation, we consider  $\alpha_2$ -Ti<sub>3</sub>Al (D0<sub>19</sub>, space group nr. 194 ( $P6_3/mmc$ )) (see Fig. 3.2a) as a parent phase for creating the martensitic  $\alpha'_2/\alpha'$  structures (i.e., with the same composition of Ti<sub>0.5</sub>Al<sub>0.5</sub> as the  $\beta/\beta_o$  phases). The D0<sub>19</sub> has two sublattices: a Ti sublattice containing 75% of the lattice sites and Al with 25% lattice sites (Fig. 3.2b). Since an overall composition of Ti<sub>0.5</sub>Al<sub>0.5</sub> is required for the  $\alpha'_2$  structure, the Al sublattice was fully populated with Al atoms, while the D0<sub>19</sub>-structure Ti sublattice was randomly populated with 1/3 Al atoms and 2/3 of Ti atoms (Fig. 3.2c). These are the fractional occupancies that enter the CPA structural definition using the D0<sub>19</sub> unitcell, and are the target sublattice concentrations to the supercell model as well. In the latter case, a  $2 \times 2 \times 2$  supercell of the D0<sub>19</sub> 8-atomic unit cell (all together with 64 atoms) was created. The (originally D0<sub>19</sub>-structure) Ti sublattice was randomly populated with 32 Ti and 16 Al atoms (Fig 3.2c). Hence, The resulting  $\alpha'_2$  structure is only a partially ordered structure (see Fig. 3.1e). In order to create a disordered  $\alpha'$  structure with the composition Ti<sub>0.5</sub>Al<sub>0.5</sub>, all 64 atom sites were randomly populated with 32 Ti and 32 Al atoms, i.e., the resulting structure is hcp lattice (A3, space group nr. 194 ( $P6_3/mmc$ )) with fractional occupancies  $x_{\text{Ti}} = 0.5$  and  $x_{\text{Al}} = 0.5$  for all sites. For the Mo-alloyed ordered  $\alpha'_2$  structures (Fig 3.2f), Mo was considered to replace Al/Ti on Ti-sublattice (of the underlying D0<sub>19</sub> structure, Fig. 3.2b). The reason is that our calculations revealed that adding Mo on the Al-sublattice yields higher energies than on the Ti-sublattice and hence such atomic distribution is less favorable. As a fully ordered counterpart of the  $\alpha'$ -TiAl phase, we consider the orthorhombic B19-TiAl (space group nr. 51 ( $Pmma$ )) phase (see Fig. 3.1g) [64].

## 3.2 Computational methods

Our calculations are based on Density Functional Theory (DFT), introduced in Chap. 2 as implemented in two complementary codes. The supercell calculations were performed using Vienna *Ab-initio* Simulation Package (VASP) [65] using Projector Augmented-Wave method (PAW) potentials [39, 66]. The valence configurations of used pseudopotentials of Ti, Al, and Mo were  $[\text{Ar}]3d^24s^2$ ,  $[\text{Ne}]3p^1$ , and  $[\text{Kr}]4d^55s^1$  respectively. The electron-electron exchange and correlation interactions were calculated using Perdew-Burke-Ernzerhof's formulation of the generalized gradient approximation (GGA-PBE) [33].



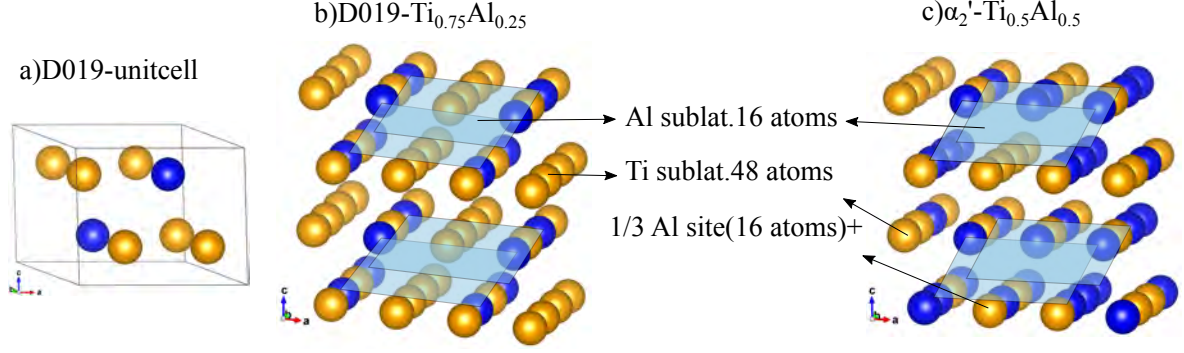


Figure 3.2: A schematic visualization of the relation between  $\alpha_2$ -Ti<sub>3</sub>Al and  $\alpha'_2$ -TiAl structures: (a)  $\alpha_2$  (D0<sub>19</sub>) unit cell, (b)  $2 \times 2 \times 2$  supercell of  $\alpha_2$ , and (c)  $\alpha'_2$  supercell with (D0<sub>19</sub>) Al-sublattice fully occupied with Al and (D0<sub>19</sub>) Ti-sublattice populated with 2/3 Ti and 1/3 Al atoms.

Table 3.1: Overview of the investigated TiAl-phases.

Phase	Nominal compositions	Ordering	Space group	Structure type
$\alpha_2$	hcp-Ti <sub>3</sub> Al	ordered	$P6_3/mmc$	D0 <sub>19</sub>
$\alpha'_2$	hcp-TiAl	partially ordered	$P6_3/mmc$	D0 <sub>19</sub>
$\alpha'$	hcp-Ti <sub>3</sub> Al	disordered	$P6_3/mmc$	A4
$\beta_o$	bcc-TiAl	ordered	$Pm\bar{3}m$	B2
$\beta$	bcc-TiAl	disordered	$Im\bar{3}m$	A2
$\gamma$	bct-TiAl	ordered	$P4/mmm$	L1 <sub>0</sub>
$\gamma_{\text{dis}}$	fcc-TiAl	disordered	$Fm\bar{3}m$	L1 <sub>0</sub>
B19	orthorhombic-TiAl	ordered	$Pmma$	B2

The wave functions were expanded in plane waves up to a kinetic energy cut-off of 500 eV. An automatically generated  $\Gamma$ -centered Monkhorst-Pack mesh of  $k$ -points was used to sample the irreducible part of the Brillouin zone. The spacing of  $k$ -points used for sampling the irreducible part of the first Brillouin zone was  $\approx 0.1 \text{ \AA}^{-1}$ . This translates to  $19 \times 19 \times 19$ ,  $12 \times 12 \times 13$  and  $20 \times 20 \times 18$   $k$ -point meshes for the reciprocal lattice of  $\beta_o$ ,  $\alpha_2$  and  $\gamma$  unit cells, respectively.

The calculations were converged with respect to the number of  $k$ -points and plane wave cut-off energy to reach a total energy accuracy of 1 meV/at. or better. A total energy convergence threshold of  $10^{-6}$  eV (per simulation box) was used for the electronic self-consistency, while  $10^{-4}$  eV was used as a stopping criterion for the structural relaxations. In order to compare the influence of local atomic relaxations, different optimization schemes were used and are discussed in the next chapters.

The second approach employed the Green’s function Exact Muffin-tin Orbital (EMTO) method [67, 68] within the Coherent Potential Approximation (CPA) [69–71] as implemented in the Lyngby version of EMTO-CPA code [72]. The intrasite Coulomb interactions parameters, that describe electrostatic interactions in the single-site approximation, are used in calculations of the total energy of random alloys within CPA. These parameters have been calculated using the locally self-consistent Green’s function (LSGF) [73, 74] the method implemented within the EMTO technique (ELSGF) [75]. All the self-consistent EMTO-CPA calculations were performed with the orbital momentum cutoff of  $l_{max} = 3$  for partial waves. The integration over the Brillouin zone was performed using a  $32 \times 32 \times 32$  grid of  $k$ -points for cubic structures,  $32 \times 32 \times 19$  for the hcp structure, and  $18 \times 32 \times 19$  for the B19 structure determined according to the Monkhorst-Pack scheme [76]. Self-consistent electron densities were obtained within the spherical cell approximation (SCA) [77] and the local density approximation (LDA) [32]. Then the total energies were calculated employing the full charge density (FCD) formalism [78, 79] and the GGA-PBE [33] for the exchange-correlation energy. In all the EMTO-CPA calculations of the B19 structure, we have used the relaxed atomic coordinates of TiAl calculated by VASP. Parts of most of the figures in this thesis were visualized using the VESTA package [80–82].

Thermal properties were evaluated within the quasi-harmonic approximation (QHA) using the phonopy code [83, 84].

The atomic distributions inside the supercells were generated following the Special Quasi-random Structures (SQSs) concept [85] with optimized pair correlation functions up to the 7<sup>th</sup> coordination shell [86] using an in-house software tool [63].

## 3.3 Structural connections

### 3.3.1 Bcc-to-fcc structural connections

Note: This section is a part of an own publication [14].

In order to investigate the transformation barriers, it is necessary to define the structural connection(s) of the initial and final phases of interest. When a body-centered cubic phase is represented by a conventional cubic cell, a simple tetragonal deformation leads to a face-centered cubic structure represented by a body-centered tetragonal cell (bct) (Fig. 3.3a). This is known as Bain’s transformation path [87–95]. As the starting points, first, consider the  $a$  and  $c$  be the lattice constants of the bcc or bct structure;  $a = c = a_{bcc}$  in the former state, i.e.  $c/a = 1$ . Second consider an fcc conventional cell with a cubic lattice parameter  $a_{fcc}$ ; the lattice parameters of the corresponding bct cell are  $a = a_{fcc}\sqrt{2}/2$  and  $c = a_{fcc}$ ,

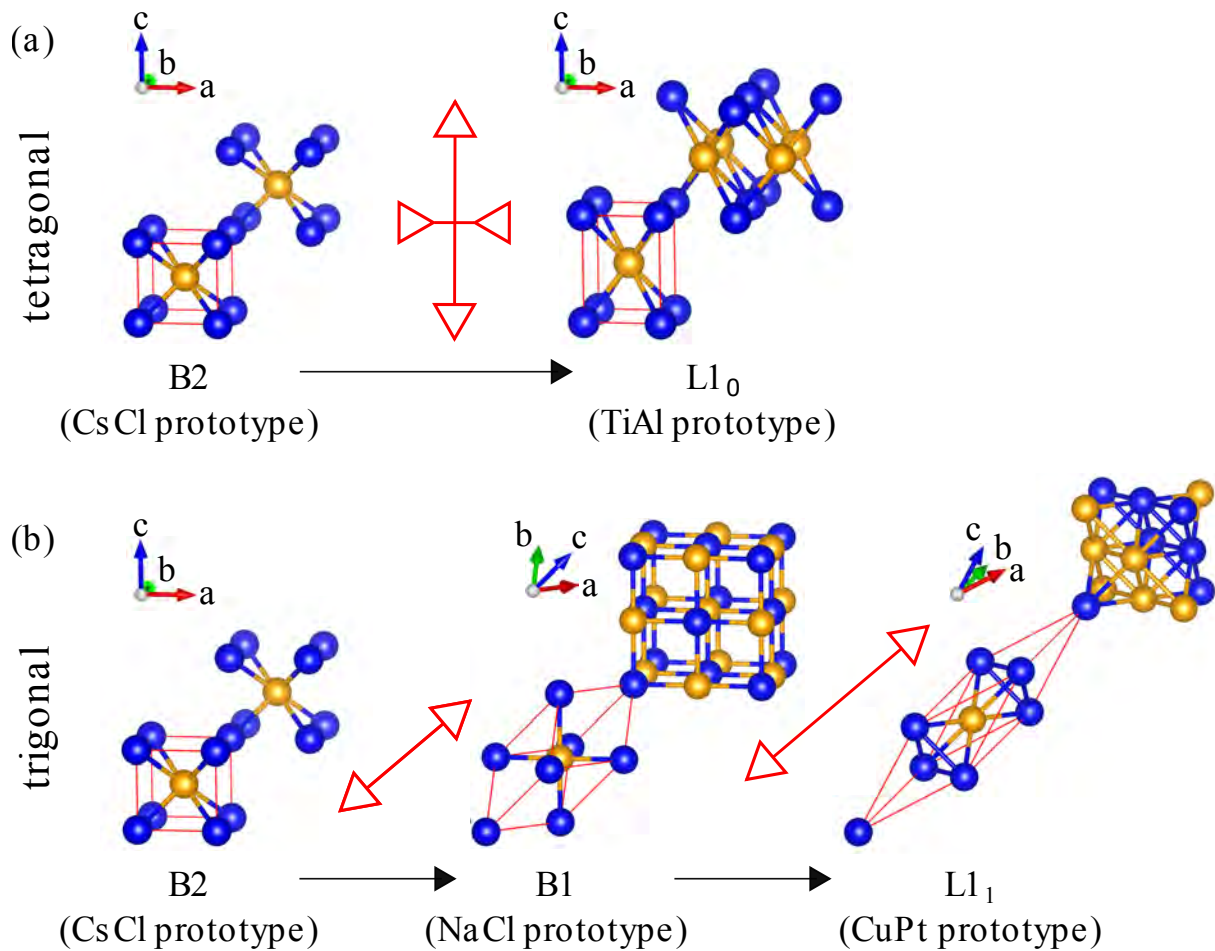


Figure 3.3: Visualization of the considered structural transformations: (a) tetragonal (Bain's) path connecting the  $\beta_o$  (B2) and  $\gamma$  (L1<sub>0</sub>) structures and (b) trigonal path connecting the  $\beta_o$  (B2) and L1<sub>1</sub> structures an intermediate B1 structure. In the case of disordered systems, all sites are occupied by both Ti and Al (and Mo) atoms with an equal probability reflecting the desired composition, and both paths connect the bcc and the fcc structures, whereby the trigonal path contains an intermediate simple cubic structure. The red arrows schematically show the applied deformation (tetragonal or trigonal).

i.e.,  $c/a = \sqrt{2}$ . Using a transformation coordinate  $\Delta$ , where  $\Delta = 0$  corresponds to the bcc structure whereas  $\Delta = 1$  represents the bct (fcc) structure, the lattice parameters of the bct cell change as:

$$a(\Delta) = (1 - \Delta)a_{\text{bcc}} + \Delta \frac{\sqrt{2}}{2} a_{\text{fcc}} , \quad (3.1)$$

$$c(\Delta) = (1 - \Delta)a_{\text{bcc}} + \Delta \cdot a_{\text{fcc}} . \quad (3.2)$$

During this transformation, the  $(100)_{\text{bcc}}$  plane converts to the  $(110)_{\text{fcc}}$  while the  $(001)_{\text{bcc}}$  remains the  $(001)_{\text{fcc}}$  plane. We note, that some authors (see, e.g., Refs. [94–97]) use directly  $c/a$  as the transformation coordinate changing from  $c/a = 1$  ( $\Delta = 0$ ) to  $c/a = \sqrt{2}$  ( $\Delta = 1$ ). Another important point is that the lattice parameters change linearly along the transformation path. Consequently, volume is neither linearly changing with  $\Delta$  nor it is constant as, e.g., in Ref. [93]. Nonetheless, in the particular case of the Bain’s path in the TiAl+Mo system, these different definitions result in negligible changes of the energy landscape since the specific volumes of the  $\beta_{\text{o}}$ -TiAl ( $V = 16.19 \text{ \AA}^3/\text{at.}$ ) and the  $\gamma$ -TiAl ( $V = 16.25 \text{ \AA}^3/\text{at.}$ ) phases are almost identical.

When applying the Bain’s transformation path to the ordered  $\gamma$ -TiAl phase which is a slightly tetragonally deformed fcc structure, the lattice parameters  $a_{\text{fcc}}$  in Eqs. (3.1) and (3.2) are replaced by  $a_{\gamma}$  and  $c_{\gamma}$ , respectively. The Bain’s transformation path is schematically shown in Fig. 3.3a for the ordered structures  $\beta_{\text{o}} \leftrightarrow \gamma$  and the two chemical species Ti and Al are shown as spheres with different colors (blue and orange, respectively). In the case of transformations between binary disordered structures,  $\beta \leftrightarrow \gamma_{\text{dis}}$ , all lattice sites are equivalent, occupied randomly by Ti and Al atoms with the same probability (all atoms in the figure would have the same color). The trigonal path is another type of a bcc-to-fcc transformation (see, e.g., Refs. [88–93, 95–102]). As shown in Fig. 3.3b, it is defined by an extension along the  $[111]$  direction of the bcc structure. The ordered cubic-symmetry structures forming an equimolar binary compound are B2 (CsCl prototype), B1 (NaCl prototype), and  $L1_1$  (CuPt prototype). They can be conveniently described by a suitable transformation coordinate  $\Delta$  with values  $\Delta = 0$  for the bcc (B2 in the case of ordered binary compound) phase,  $\Delta = \frac{1}{3}$  for the simple cubic (sc)(B1) phase and  $\Delta = 1$  for the fcc ( $L1_1$ ) phase. The lattice vectors matrix defining the unit cell is given as a function of the transformation coordinate  $\Delta$ , following the graphical representation in Fig. 3.3b by also considering the possible specific volume change along the transformation path, as:

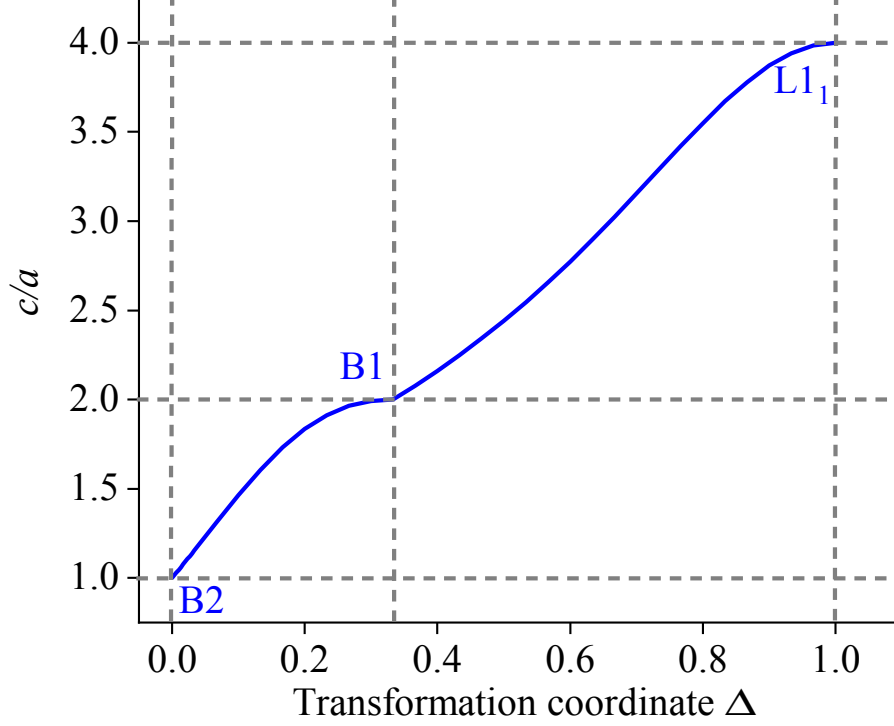


Figure 3.4: Dependence of  $c/a = \sqrt{2}|\llbracket 111 \rrbracket|/|\llbracket 11\bar{2} \rrbracket|$  on the transformation coordinate  $\Delta$  for the trigonal transformation defined by Eqs. (3.3) and (3.4).  $|\llbracket \cdot \rrbracket|$  means length of a vector  $\llbracket \cdot \rrbracket$  in a non-orthogonal coordination system which is defined by the rows of matrix  $\mathbf{M}$  in Eq. (3.3).

$$\mathbf{M}(\Delta) = \begin{cases} a(\Delta) \begin{pmatrix} 1 & \epsilon & 0 \\ 0 & 1 & \epsilon \\ \epsilon & 0 & 1 \end{pmatrix}, & \epsilon = 3\Delta, & \text{if } 0 \leq \Delta \leq \frac{1}{3}, \\ a(\Delta) \begin{pmatrix} 1 & 1-\epsilon & \epsilon \\ \epsilon & 1 & 1-\epsilon \\ 1-\epsilon & \epsilon & 1 \end{pmatrix}, & \epsilon = \frac{3}{4} \left( \Delta - \frac{1}{3} \right), & \text{if } \frac{1}{3} \leq \Delta \leq 1, \end{cases} \quad (3.3)$$

The unit cell volume,  $V = \det \mathbf{M}$ , is linearly interpolated between the high-symmetry structures along the trigonal transformation path as

$$V(\Delta) = \begin{cases} (1 - 3\Delta)V_{\text{bcc}} + 3\Delta \cdot V_{\text{sc}}, & \text{if } 0 \leq \Delta \leq \frac{1}{3}, \\ 3\Delta \cdot V_{\text{sc}} + \frac{3\Delta - 1}{2}V_{\text{fcc}}, & \text{if } \frac{1}{3} \leq \Delta \leq 1, \end{cases} \quad (3.4)$$

where  $V_{\text{bcc}}$ ,  $V_{\text{sc}}$ , and  $V_{\text{fcc}}$  are equilibrium volumes of bcc (B2), sc (B1) and fcc (L1<sub>1</sub>) structures per 2 atoms, respectively.

We note that our definitions of the trigonal transformation path allow for volume changes between the  $\beta_o$  and L1<sub>1</sub>, and  $\beta$  and  $\gamma_{\text{dis}}$  phases, respectively. In contrast to our description,

previous literature focusing on the trigonal path with the constant volume used  $c/a$  as a transformation coordinate [89, 93]. There,  $c$  is the length of the [111] vector in a non-orthogonal coordination system defined by rows of the matrix  $\mathbf{M}$  in Eq. (3.3), whereas  $a = |[11\bar{2}]|/\sqrt{2}$ . Knowing additionally the relation between  $V = \det \mathbf{M}$  and  $\Delta$  (in the present case given by Eq. (3.4)), one can directly relate  $c/a$  to  $\Delta$ . This is shown in Fig. 3.4.

### 3.3.2 Bcc-to-hcp structural connections

In this study, also a bcc $\rightarrow$ hcp transformation path was investigated. Namely, it was applied for ordered phases,  $\beta_o \rightarrow$ B19 and disordered  $\beta \rightarrow \alpha'$  phases to reveal barriers for corresponding martensitic transformations.

As proposed by Paidar *et al.* [93], this can be realized by applying a homogeneous deformation (volume expansion) coupled with shuffling of neighboring atomic planes in opposite directions.

The structure in the bottom-left corner of Fig. 3.5,  $(\delta_c, \delta_s) = (0, 0)$ , represents the  $\beta_o$ -bcc structure projected along the  $[1\bar{1}0]$  cubic direction, thus leading to a representation with and tetragonal cell with  $a$  and  $c$  lattice constants equal to  $3.187 \text{ \AA}$  ( $= a_{\beta_o}$ ) and  $4.507 \text{ \AA}$  ( $= \sqrt{2}a_{\beta_o}$ ), respectively. The upper-right corner  $(\delta_c, \delta_s) = (1, 1)$  shows the orthorhombic B19 structure, representing a hexagonal counterpart of the ordered the  $\beta_o$  phase. To execute  $\beta_o \rightarrow$ B19 transition, two independent mechanisms are used simultaneously. The first one is related to changing the cell shape (represented by the parameter  $\delta_c$ ) by stretching  $a$  by approximately 9%,  $c$  by 3% and shrinking the  $b$  lattice constant by approximately 8% (follow structure changes along the horizontal rows in Fig. 3.5). The lattice parameters of  $\beta_o$  unitcell change as:

$$a_{\text{B19}} = \frac{\sqrt{2}a_{\beta_o}}{\left(\frac{V}{V_0}\right)^{1/3}}, \quad (3.5)$$

$$b_{\text{B19}} = a_{\text{B19}} \left( \frac{\delta_s 2\sqrt{3} - 3\sqrt{2}}{6} + \frac{\sqrt{2}}{2} \right), \quad (3.6)$$

$$c_{\text{B19}} = a_{\text{B19}} \left( \frac{\delta_s(2\sqrt{2} - 3)}{3} + 1 \right), \quad (3.7)$$

where

$$\frac{V}{V_0} = \sqrt{2} \left[ \frac{\delta_s 2\sqrt{3} - 3\sqrt{2}}{6} + \frac{\sqrt{2}}{2} \right] \left[ \frac{\delta_s 2\sqrt{2} - 3}{3} + 1 \right] \quad (3.8)$$

and  $V_0 = (a_{\beta_o})^3$ . For  $\delta_s = \delta_c = 0$ , we obtain the bcc structure and  $\delta_s = \delta_c = 1$  corresponds to the hcp structure.

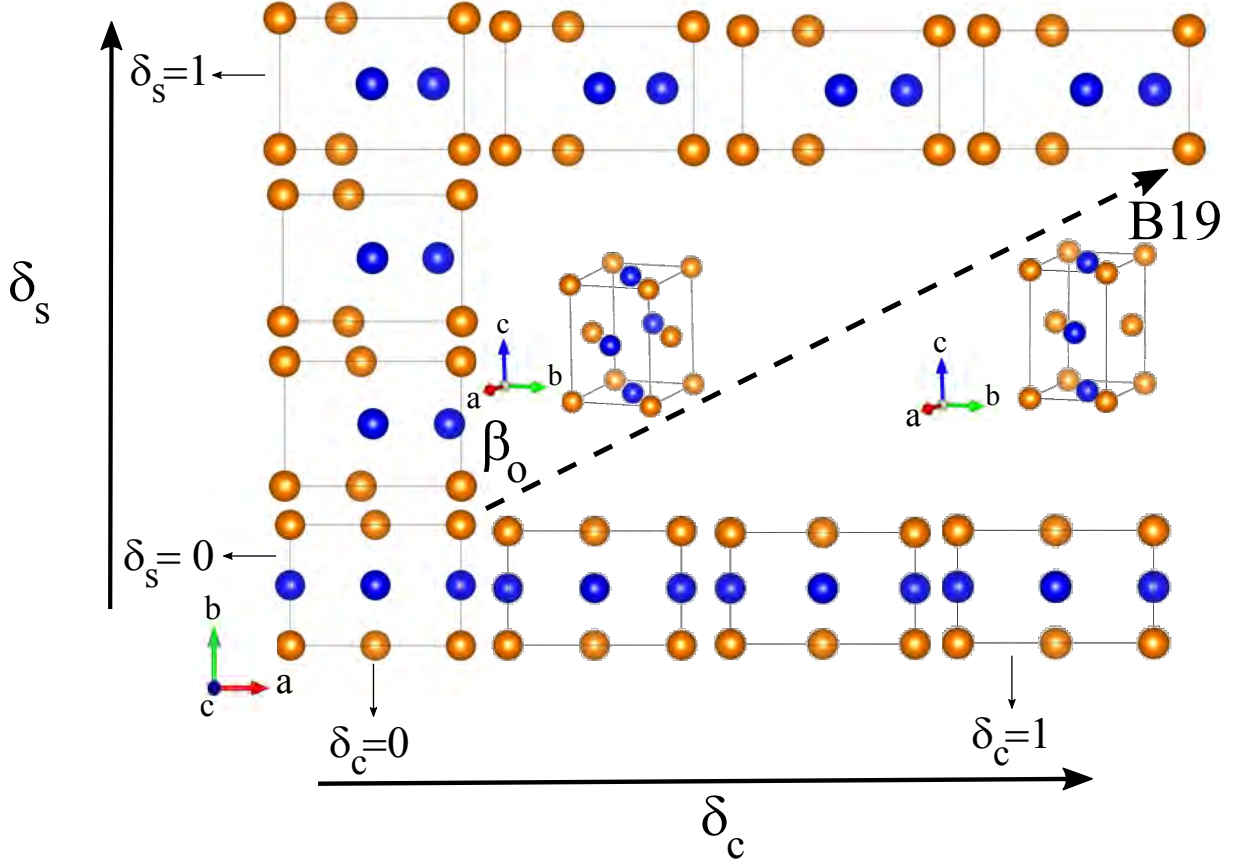


Figure 3.5: Visualization of  $\beta_o \rightarrow \text{B19}$  transformation in terms of cell shape changes and shuffling of atoms.

Therefore, along the  $\beta_o \rightarrow \text{B19}$  transformation path the lattice parameters change as:

$$a = a_{\beta_o}(1 - \delta_c) + a_{\text{B19}}\delta_c , \quad (3.9)$$

$$b = b_{\beta_o}(1 - \delta_c) + b_{\text{B19}}\delta_c , \quad (3.10)$$

$$c = c_{\beta_o}(1 - \delta_c) + c_{\text{B19}}\delta_c . \quad (3.11)$$

The second mechanism is the shuffling of atomic positions which is visualized in Fig. 3.5 as the structural changes along the  $\delta_s$  axis (vertical columns) column (a), as the dark blue balls (Al atoms) are approaching more each other. Namely, the distances between the atoms (both Al (blue) and Ti (orange)) change from being uniform along the  $a$  lattice vector for  $\delta_s = 0$  to being pair-wise coupled ( $\delta_s = 1$ ).

The positions of atoms are, in the units of the orthorhombic lattice constants  $a$ ,  $b$  and  $c$ , given as  $(\frac{1}{2} - \frac{\delta_s}{6}, 0, \frac{1}{2})$ ,  $(0, 0, 0)$ ,  $(-\frac{\delta_s}{6}, \frac{1}{2}, \frac{1}{2})$  and  $(\frac{1}{2}, \frac{1}{2}, 0)$ .

The above described transformations represent the well known Burgers orientation relationship  $(110)_{\text{bcc}} \parallel (0001)_{\text{hcp}}$ , which has been intensively studied before [93, 103–105].

It is trivial to mention the same equations (Eqs. (3.9)–(3.11)) and definitions were used for  $\beta \rightarrow \alpha'$  transformation path.

Finally, let us know that while those two mechanisms are well defined/decoupled in the case of ordered  $\beta_o \rightarrow$ B19 phases, the exact meaning of the transformation coordinates, especially the shuffling described by  $\delta_s$ , becomes somewhat ambiguous in the case of disordered and/or Mo alloyed systems, due to the local relaxations. Therefore, investigation of the whole potential energy surface (PES) in terms of two independent parameters  $\delta_c$  and  $\delta_s$  was done only for the binary TiAl system. For the ternary TiAl+Mo systems, we used a single transformation coordinate,  $\delta$ , linearly interpolating between the  $\beta_o/\beta$  cell shape and atomic positions, and B19/ $\alpha'$  cell shape and atomic positions. Such transformation path corresponds to a section of the PES along with configurations with  $\delta_c = \delta_s = \delta$ , visualized by a dashed arrow in Fig. 3.5. The error in estimating the transformation barrier from the whole PES and along this single section are discussed in Chap. 9 for the case of ordered and disordered binary TiAl systems.



## Structural properties

The equilibrium structural properties and energies were obtained by fitting volume-dependent energies by Birch-Murnaghan equation of state [61] by fixing the cell symmetry (cubic, hexagonal, orthorhombic) and relaxing atomic positions for each volume, unless stated otherwise. The chemical stability was quantified using the formation energy,  $E_f$ , defined as:

$$E_f = E_0(\text{Ti}_m\text{Al}_n\text{Mo}_l) - \frac{mE_0(\text{Ti}) + nE_0(\text{Al}) + lE_0(\text{Mo})}{m + n + l}, \quad (4.1)$$

where  $E_0(\text{Ti}_m\text{Al}_n\text{Mo}_l)$  is the total energy (per atom) of a supercell with  $m$ ,  $n$  and  $l$  atoms of Ti, Al and Mo, respectively, representing the studied phases.  $E_0(\text{Ti})$ ,  $E_0(\text{Al})$  and  $E_0(\text{Mo})$  are the total energies (per atom) of hcp-Ti, fcc-Al and bcc-Mo elements in their standard (reference) states, respectively. The equilibrium total energies were obtained by fitting volume-dependent energies by Birch-Murnaghan equation of state [61] by fixing the cell symmetry (cubic, hexagonal, orthorhombic) and relaxing atomic positions for each volume unless stated otherwise.

### 4.1 TiAl-binary alloys

The equilibrium ground state properties of a compound at zero pressure are obtained by minimizing the internal energy. The relevant degrees of freedom are specific volume, atomic position, and cell shape. The atomic positions which depend on the local chemical environment, are naturally differing from ideal lattice sites in the supercell VASP approach to disordered systems due to explicitly considering different nearest neighborhoods. This relaxation is caused by energy decrease by vanishing a net force each atom is experiencing. On the other hand, due to the effective potential experienced by atoms in the EMTO-CPA approach, no such local relaxations occur since all sites on a certain sublattice are strictly equivalent. Similarly, due to the explicit disorder in the supercell

treatment together with rather small supercell sizes used, the final symmetry of the disordered supercells is very low (ideally P1), which eventually leads to non-zero stresses even for zero pressure.

Such a cell shape breaks the macroscopic crystallographic symmetry; it is an artificial consequence of the arrangement of atoms in the supercell and will not occur on a macroscopic scale due to averaging. Therefore, it is not present in the EMTO-CPA treatment where the long-range order is correctly described.

In order to address these issues, we consider 3 different optimization schemes of each supercell structure calculated with VASP. Namely, 'no-relaxation' represents structures optimized only with respect to the specific volume, by fixing the atomic positions and desired crystallographic symmetry (cubic, hexagonal, orthorhombic). These results should (structurally) correspond to the EMTO-CPA results.

In the second mode, 'ionic-relaxation', the atomic positions and volume are relaxed while still restricting the cell shape to the desired macroscopic symmetry (cubic for  $\beta/\beta_o$  structures, hexagonal for  $\alpha'/\alpha'_2$  structures, tetragonal for  $\gamma/\gamma_{\text{dis}}$  and orthogonal for B19 structure). In order to achieve the cell shape optimization with prescribed symmetry, the  $c/a$  ratio was also optimized by running a series of calculations at fixed volume in the case of hexagonal and tetragonal structures; for the orthorhombic phase, additionally also the  $b/a$  ratio was optimized. Finally, we also 'fully-relaxed' the cell shape by setting ISIF=3 in the VASP input file INCAR.

As seen from Table 4.1,  $E_f$  is negative for all compositions, suggesting that all structures are chemically stable. As expected, all relaxation schemes yield the same result in the case of the  $\beta_o$  and  $\gamma$  structures due to their high symmetry. Minor energy differences between different optimization schemes are obtained in the case of the B19-TiAl structure. Nonetheless, the differences in the range of 1 meV/at. are the edge of the accuracy of our calculations, and consequently, also in this case we conclude that the optimized geometry, as well as formation energy, is almost independent of the chosen method.

Allowing the local atomic positions to relax yields a decrease in the formation energy for all disordered (partially ordered,  $\alpha'_2$ ) structures: by  $\approx 20$  meV/at. for  $\alpha'/\alpha'_2$ ,  $\approx 10$  meV/at. for  $\gamma_{\text{dis}}$  and  $\approx 50$  meV/at. for the  $\beta_o$  phase.

Allowing for a full cell shape relaxation in the case of the hexagonal  $\alpha'/\alpha'_2$  structures did not yield any significant further relaxation.

Significantly larger discrepancies are obtained in the case of the  $\beta$  phase. A large energy drop of 24 meV/at. is obtained once the cell shape is allowed to relax. A closer look reveals that the initially cubic shape is slightly tetragonally distorted; some local environments

are even so strongly distorted, that they notably resemble the  $\gamma$ -TiAl phase, the ground state structure for stoichiometric composition. Therefore, a spontaneous transformation  $\beta \rightarrow \gamma$  is predicted to occur for the disordered  $\beta$  phase as a consequence of the symmetry broken by the chemical disorder in the SQS (see Chap. 8 and Ref. [14]).

Analyzing the energy differences between the ordered and disordered phases (optimization mode 'ionic-relaxation') yields that the formation energies of the ordered phases are lower than that of the disordered phases, namely  $\Delta E_f(\alpha' - \alpha'_2) = 42$  meV/at.,  $\Delta E_f(\beta - \beta_o) = 11$  meV/at. and  $\Delta E_f(\gamma_{\text{dis}} - \gamma) = 163$  meV/at. In the former case of hexagonal structures, even lower energy is obtained for the fully-ordered variant B19,  $\Delta E_f(\alpha'_2 - \text{B19}) = 60$  meV/at.

Similarly, the energy differences have been calculated for EMTO-CPA result. Specifically,  $\Delta E_f(\alpha' - \alpha'_2) = 45$  meV/at.,  $\Delta E_f(\beta - \beta_o) = 56$  meV/at. and  $\Delta E_f(\gamma_{\text{dis}} - \gamma) = 179$  meV/at.. It is predicted the lower energy difference with the VASP-SQS method for all cases, specially for the cubic TiAl binary alloys. Further, discussions about the fully-relaxed result of  $\beta/\beta_o$  and  $\gamma_{\text{dis}}/\gamma$  have presented in detail in Chap. 8.

## 4.2 Ternary TiAl+Mo system

### 4.2.1 Cell shape optimization

The main aim of this chapter is to reveal compositional trends induced by alloying Mo into the cubic and hexagonal  $\text{Ti}_{0.5}\text{Al}_{0.5}$  phases. We start by discussing structural trends in this section, followed by stability analysis and mechanical properties in the next sections. The below presented structural properties of supercells are based on the 'ionic-relaxation' data (see the previous section) preserving the macroscopic unit cell geometry but relaxing local atomic positions. The only exception is the B19 phase for which the 'fully-relaxed' data are presented. This was motivated by (i) a good agreement between the two relaxation schemes for pure  $\text{Ti}_{0.5}\text{Al}_{0.5}$  (Tab. 4.1) and by (ii) employing a computationally more efficient method (a full relaxation in a single calculation instead of a series of fixed volume/cell shape calculations which would have been subsequently fitted).

The equilibrium volume trends are summarized in Fig. 4.1 for  $\text{Ti}_{0.5}\text{Al}_{0.5-x}\text{Mo}_x$  (Ti-rich) and  $\text{Ti}_{0.5-x}\text{Al}_{0.5}\text{Mo}_x$  (Al-rich) compositions ( $0 \leq x \lesssim 0.17$ ) as a function of the Mo content,  $x$ . It is found that the volume of TiAl+Mo alloys decreases almost linearly in most of the structures. The most significant deviation is the Ti-rich  $\beta_o$  and B19 phases yielding an almost constant value.

The mostly decreasing specific volume together with the fact that Mo is heavier than

Table 4.1: Formation energy  $E_f$ , equilibrium volume  $V_0$  optimized lattice constants  $a$ ,  $b$  and  $c$ ,  $c/a$  and bulk modulus  $B$ , for different TiAl-phases calculated using the supercell approach with various optimization schemes and compared with EMTO-CPA results.

Phase	Relaxation	$E_f$ [eV/at.]	$V_0$ [ $\text{\AA}^3$ /at.]	$a$ [ $\text{\AA}$ ]	$b$ [ $\text{\AA}$ ]	$c$ [ $\text{\AA}$ ]	$c/a$	$B$ [GPa]
$\beta_o$	EMTO-CPA	-0.281	16.257	3.192	3.192	3.192	1.000	111
	no-relaxation	-0.263	16.185	3.187	3.187	3.187	1.000	110
	ionic-relaxation	-0.263	16.185	3.187	3.187	3.187	1.000	110
	full-relaxation	-0.263	16.186	3.187	3.187	3.187	1.000	-
$\beta$	EMTO-CPA	-0.237	16.496	3.207	3.207	3.207	1.000	105
	no-relaxation	-0.201	16.468	3.178	3.178	3.178	1.000	105
	ionic-relaxation	-0.252	16.305	3.194	3.194	3.194	1.000	154
	full-relaxation	-0.276	16.466	3.608	2.875	3.189	0.883	-
$\gamma$	EMTO-CPA	-0.404	15.95	3.96	3.96	4.06	1.03	117
	no-relaxation	-0.404	16.245	3.994	3.994	4.073	1.019	113
	ionic-relaxation	-0.404	16.245	3.994	3.994	4.073	1.019	113
	full-relaxation	-0.404	16.245	3.994	3.994	4.073	1.019	113
$\gamma_{\text{dis}}$	EMTO-CPA	-0.225	16.25	4.02	4.02	4.02	1.000	110
	no-relaxation	-0.232	16.550	4.045	4.045	4.045	1.000	105
	ionic-relaxation	-0.241	16.557	4.045	4.045	4.045	1.000	103
	full-relaxation	-0.248	16.497	4.760	4.760	2.936	1.616	-
$\alpha'_2$	EMTO-CPA	-0.287	16.506	5.727	5.727	4.648	0.811	108
	no-relaxation	-0.280	16.427	5.721	5.721	4.635	0.811	108
	ionic-relaxation	-0.300	16.409	5.737	5.737	4.604	0.802	107
	full-relaxation	-0.301	16.398	5.791	5.715	4.604	0.795	-
$\alpha'$	EMTO-CPA	-0.242	16.592	5.739	5.739	4.653	0.810	106
	no-relaxation	-0.240	16.556	5.729	5.729	4.659	0.813	107
	ionic-relaxation	-0.258	16.540	5.733	5.733	4.647	0.810	106
	full-relaxation	-0.259	16.534	5.770	5.754	4.647	0.805	-
$B19$	EMTO-CPA	-0.352	16.327	4.923	2.865	4.631	0.940	112
	no-relaxation	-0.359	16.279	4.875	2.882	4.634	0.950	105
	ionic-relaxation	-0.360	16.241	4.888	2.871	4.627	0.946	111
	full-relaxation	-0.361	17.361	5.086	2.936	4.649	0.914	-

either of Ti and Al, suggests that the mass density of the alloys containing Mo significantly increases. We note that the trends obtained by both modeling techniques, the supercell approach (solid lines) as well as the CPA method (dashed lines), are the same and thus are expected to be trustworthy.

The volumetric trends are somewhat surprising, taking into account the atomic sizes as conventionally measured with either covalent radii ( $r(\text{Al}) = 121 \text{ pm} < r(\text{Mo}) = 154 \text{ pm} < r(\text{Ti}) = 160 \text{ pm}$  [106] or atomic radii ( $r(\text{Al}) = 125 \text{ pm} < r(\text{Ti}) = 140 \text{ pm} < r(\text{Mo}) = 145 \text{ pm}$ ) [107]. In contrast to those, metallic radii suggests that Mo is marginally the smallest atom:  $r(\text{Mo}) = 139 \text{ pm} < r(\text{Al}) = 143 \text{ pm} < r(\text{Ti}) = 147 \text{ pm}$  [108]. This points towards a stronger effect of the metallic bonding as compared with the covalent one and therefore many-body interactions are more presumably dominant than the angular bonding. Although such interpretation may seem somewhat speculative, it is well in line with the ductility trend-givers (Pugh’s criterion, Cauchy pressure) discussed later in Sec. 5.2.

Comparing ordered and disordered phases, it turns out that the ordered phases result in smaller specific volumes, hence in higher mass density. This is even strengthened by considering the B19 phase as the most ordered counterpart of the  $\alpha'/\alpha'_2$  phases. It is worth mentioning that the EMTO-CPA results for the high Mo content compositions suggest an opposite trend: a fully disordered  $\beta$  structure is predicted to have a smaller specific volume than the  $\beta_o$  phase. A closer inspection reveals that this is primarily caused by the much stronger specific volume decrease with increasing Mo content in the case of the EMTO-CPA calculations w.r.t. VASP-SQS ones. Additionally, the significant local distortions [14] which are not accounted for by the EMTO-CPA approach, lead to increasing average spacing between the atoms in the  $\beta$  phase and hence large space volume as predicted by VASP-SQS method.

## 4.2.2 Chemical stability

Chemical stability as measured by the energy of formation (Eq. 4.1) suggests that although all studied structures are chemically stable ( $E_f < 0$ ), neither of  $\gamma/\gamma_{\text{dis}}$  and B19/ $\alpha'_2/\alpha$  phases really prefers to contain Mo (Fig. 4.2). In other words, alloying Mo increases  $E_f$  with respect to the  $\text{Ti}_{0.5}\text{Al}_{0.5}$  state and hence leads to a relative destabilization of those phases.

In those cases, the CPA-based and supercell-based results exhibit qualitatively the same trends.

The  $\beta$  phase exhibits the same behaviour as described above: alloying Mo is predicted to chemically destabilize it for both VASP-SQS and EMTO-CPA methods. Contrarily

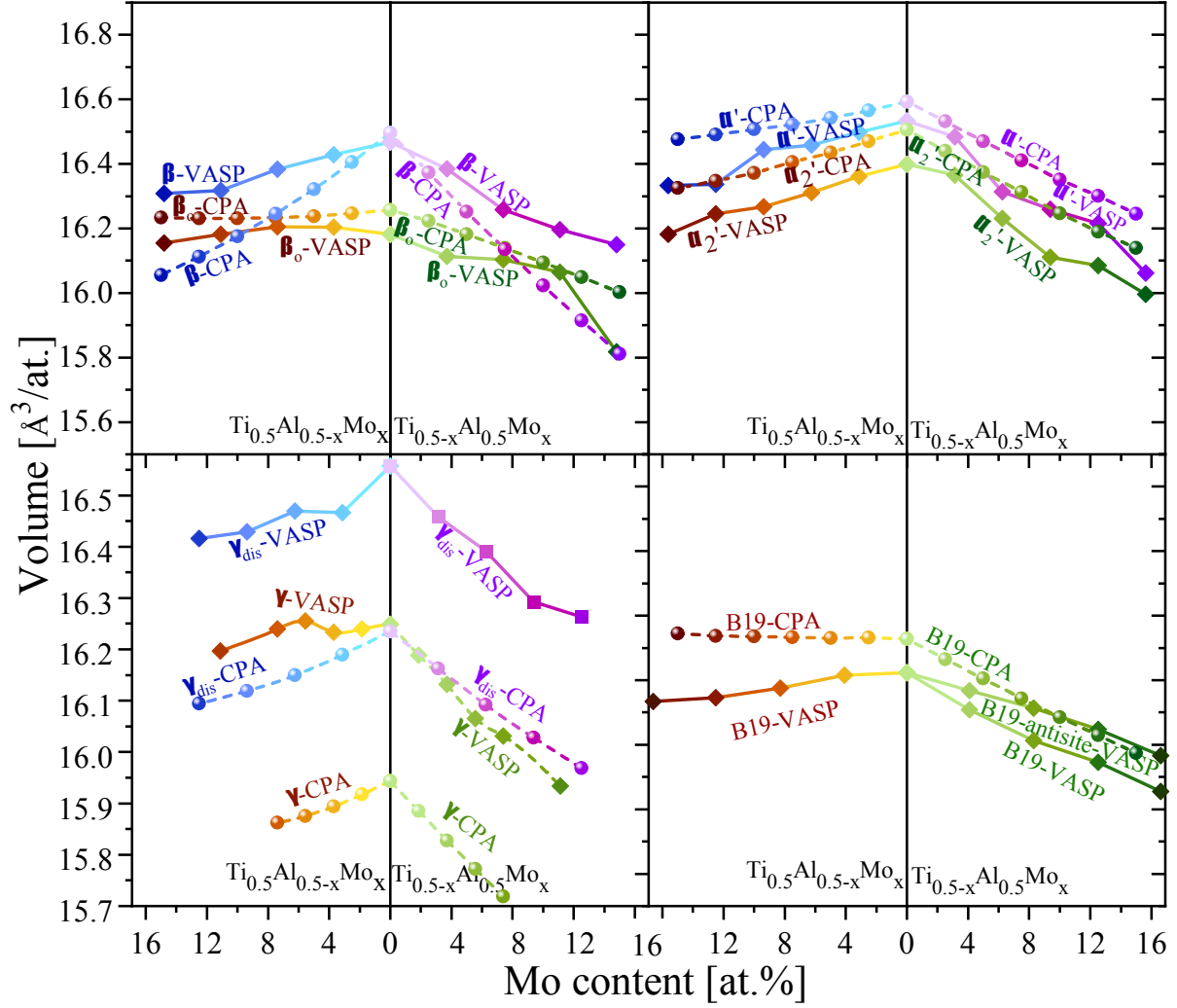


Figure 4.1: The calculated volume plotted against the molybdenum contents on two different sublattices and different structures. Dashed and solid lines denote data obtained using EMTO-CPA and VASP-SQS methods, respectively. The Ti-rich compositions are shown with blue (disordered) and orange (ordered) colors, while the Al-rich compositions with pink (disordered) and green (ordered) colors. The increasing amount of molybdenum is displayed by darkening the color shades.

to that, Mo is suggested to stabilize the ordered  $\beta_o$  phase (which is in agreement with previous data for the Ti-rich configurations [109]). While both methods agree for the Ti-rich composition, there is a large difference between them in the case of the Al-rich compositions. There the EMTO-CPA method predicts destabilization (increasing  $E_f$ ) by alloying of Mo, while the VASP-SQS method leads to a slight stabilization (decreasing  $E_f$ ). We interpret this as a direct impact of local relaxations present in the VASP-SQS method, which act as the stabilization mechanism.

Anti-site substitutional mechanisms were also considered for the Al-rich compositions

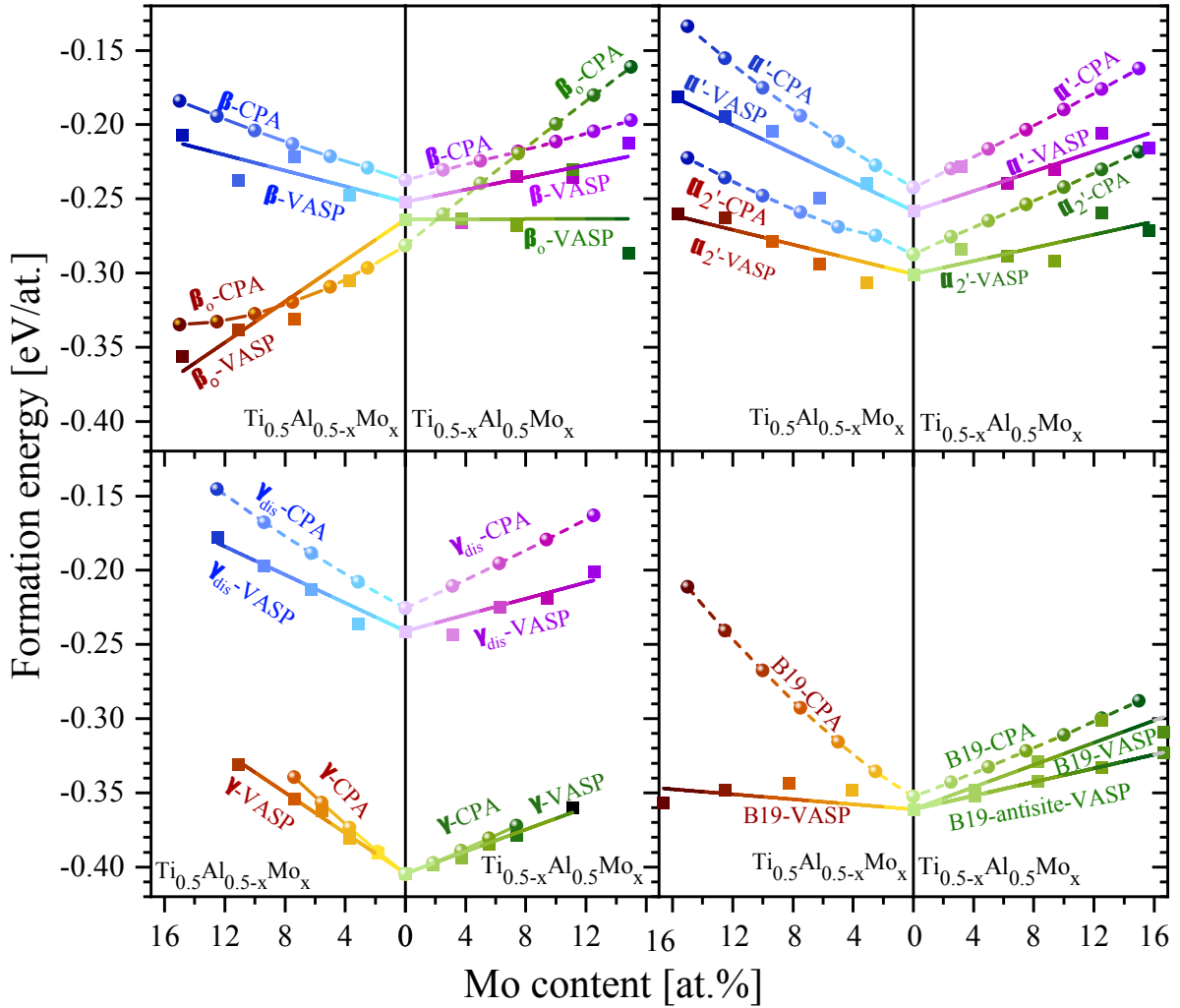


Figure 4.2: The calculated formation energy plotted against the molybdenum contents on two different sublattices and different structures. Dash and solid lines denote data obtained using EMTO-CPA and VASP-SQS method, respectively. The Ti-rich compositions are shown with blue (disordered) and orange (ordered) colors, while the Al-rich compositions with pink (disordered) and green (ordered) colors. The increasing amount of molybdenum is displayed by darkening the color shades.

of the B19 phase. In particular, Mo atoms were placed on the Al sublattice and the same number of Al atoms were distributed on the Ti sublattice. It turns out that such configurations yield even lower energies than a direct substitution with Mo atoms on the Ti sublattice. We interpret this as a strong Al sublattice preference for Mo in the case of the B19, in contrast to a previous report which did not consider anti-site defects in the B19 phase [110].

In all cases, the trends are fairly linear in the investigated compositional range and hence linear trends lines were added as guides for the eye into Fig. 4.2. The VASP-SQS data are more scattered (w.r.t. a linear trend) than the EMTO-CPA values. This is likely a consequence of finite-sized (and perhaps not large enough) supercells in the VASP-SQS approach (It is discussed in Chap. 8).

### 4.2.3 Phase stability

A further insight into the stability of individual phases is provided by investigating their elastic stability. An elastically (mechanically) stable structure is, in the Voigt's notation, described by a  $6 \times 6$  matrix  $C_{ij}$  of elastic constants, which is positive-definite, i.e. any (small-enough) deformation leads to an increase of the internal energy [111]. Positive-definiteness of a matrix is equivalent to all its eigenvalues (and in particular the smallest one), to be positive. Minimum eigenvalues for the  $C_{ij}$  matrices for all  $\beta/\beta_o$  and  $\alpha'/\alpha'_2$  (reported and discussed in detail in Chap. 5) structures are shown in Fig. 4.3. While all the hexagonal structures are predicted mechanically stable ( $\lambda_{\min} > 0$ , Fig. 4.3b), several  $\beta_o$  structures are identified as mechanically unstable ( $\lambda_{\min} < 0$ , Fig. 4.3a). Those are removed from any further analyses in this and next Chapters.

## 4.3 CPA vs supercell approach

### 4.3.1 Local relaxations

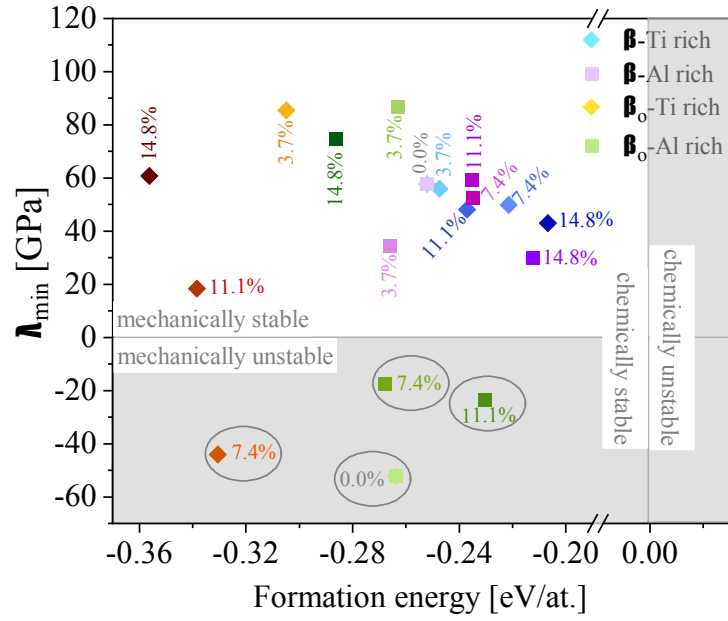
In order to understand the VASP-SQS and EMTO-CPA predictions in details, in this section we focus on differences of both methods to gain more insight into these approaches.

According to Fig.4.2, it seems  $\beta_o$  Al-rich and B19 Ti-rich compositions result in opposite trends of formation energy from the two methods. Therefore, the VASP-SQS formation energy of these compositions (green and orange solid lines, respectively) with fixed atomic positions are plotted in Fig. 4.4a to be compared with the EMTO-CPA results.

Clearly, the unrelaxed VASP results are in consistent with the EMTO-CPA data with  $\approx 20$  meV/at. differences in case of the  $\beta_o$  phase and even less for the B19 phase, which are quite acceptable. It is thereby concluded that the differences between the two methods



(a)



(b)

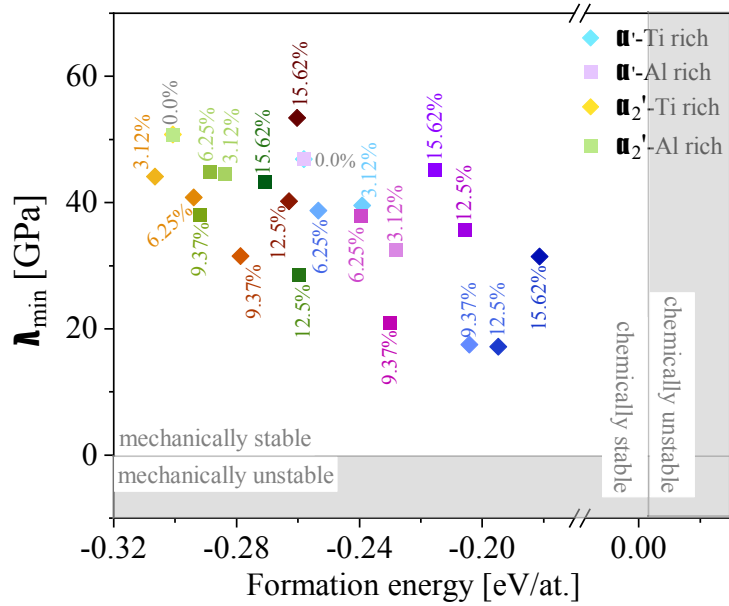


Figure 4.3: Minimum eigenvalues,  $\lambda_{\min}$ , of the matrix of elastic constants  $C_{ij}$  plotted against corresponding formation energy,  $E_f$ , for (a)  $\beta/\beta_0$  and (b)  $\alpha'/\alpha'_2$  phases as a function of Mo content. Negative (positive) values of  $\lambda_{\min}$  ( $E_f$ ) signify mechanically (chemically) unstable systems.

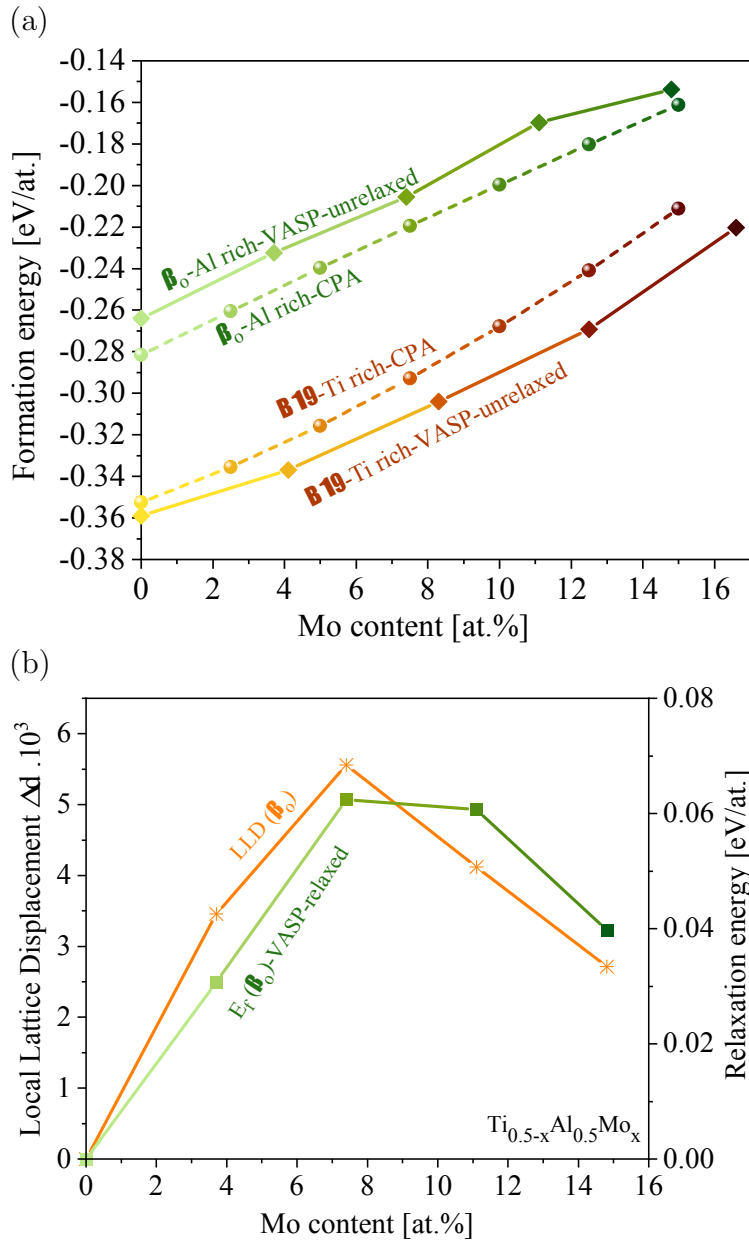


Figure 4.4: a) The unrelaxed formation energies of  $\beta_0$  Al-rich (green color), and B19 Ti-rich (orange color) compositions of VASP-SQS (solid lines) calculations have compared with EMTO-CPA (dashed lines) calculations as a function of Mo contents and b) the relaxation energies (green color) and local lattice displacement (orange color) of  $\beta_0$  Al-rich compositions as a function of Mo contents

in Fig. 4.2 stem from differently treated local atomic relaxations the effect of relaxation by relaxing the atomic position, cell shape and cell volume in structures. To quantify the effect of the atomic relaxations, the mean Local Lattice Displacement (LLD), defined as [112]:

$$\Delta d = 1/N \sum_i \sqrt{(x_i - x'_i)^2 + (y_i - y'_i)^2 + (z_i - z'_i)^2}, \quad (4.2)$$

is used to measure the effect. In the above, the relaxed and unrelaxed positions of atom  $i$  are  $(x_i, y_i, z_i)$  and  $(x'_i, y'_i, z'_i)$ , respectively and  $N$  is the number of atoms in the unitcell. In Fig.4.4b, the LLD,  $\Delta d$  and the relaxation energy are represented as a function of the Mo content for the  $\beta_o$  phase. The relaxation energy is defined as the energy difference (per atom) between the supercell relaxed and fixed atomic positions.

The  $\Delta d$  increases with Mo up to  $\approx 7.5$  at.% and afterward decreases. That is, the relaxation becomes large in concentrated alloys. The relaxation energy exhibits a similar trend as that of  $\Delta d$ , which is easy to understand since a larger  $\Delta d$  is generally expected to result in a larger relaxation energy.

### 4.3.2 Spontaneous transformation B19 $\rightarrow$ $\beta_o$

The situation is slightly more complicated in the case of the B19-phase. The orthorhombic symmetry implies that  $b/a$  and  $c/a$  ratios are degrees of freedom during the structural optimization. Combined with the relaxation of the atomic positions allowed by the VASP calculation this leads to a possibility of relaxing the B19-based supercell into the  $\beta_o$  (see Sec. 3.3.2). We therefore analyze of our VASP B19 Ti-rich structures in terms of radial distribution functions. Local structural motifs resembling a cubic structure can be detected after the full relaxation especially for high Mo contents (see Fig. 4.5). In the other words, the structural instability of B19 phase at  $\text{Ti}_{0.38}\text{Al}_{0.50}\text{Mo}_{0.12}$  and  $\text{Ti}_{0.34}\text{Al}_{0.50}\text{Mo}_{0.16}$  compositions have emerged already, facilitated by the local atomic displacements. For instance in case of 12.5 at.% Mo, the local structural motif with  $a = 4.031 \text{ \AA}$  and  $b = c = 2.850 \text{ \AA}$  (see Fig. 4.6) changes to  $a = 3.081 \text{ \AA}$ ,  $b = 3.224 \text{ \AA}$  and  $c = 3.010 \text{ \AA}$  after full structural relaxation leading to a significant change of the cell shape, which is noticeably similar to the cubic lattice parameters. Therefore we conclude that the discrepancies between the EMTO-CPA and VASP-SQS results shown in Fig. 4.2 for the B19 phase and its Ti-rich compositions can be ascribed to fundamental differences between the two methods: the system exhibits spontaneous (barrier-less) phase transformation from the B19 to the  $\beta_o$  phase for high Mo content, which cannot be realised by the relaxation scheme in the EMTO code (having fixed atomic positions), but is reflected by the structures fully-relaxed by VASP. The B19 $\rightarrow$   $\beta_o$  transformation is discussed in detail in Chap. 9.

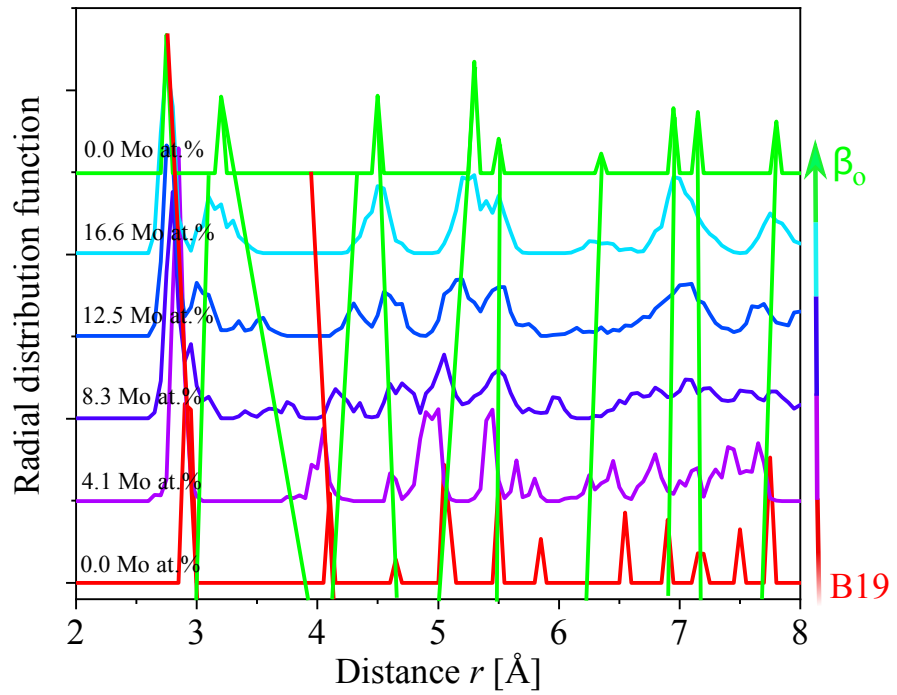


Figure 4.5: Radial distribution functions for  $0 \leq \text{Mo} \leq 16.6$  at.% compositions and binary  $\beta_0$  composition. The straight lines schematically indicate shifts in selected nearest neighbor shells of atoms.

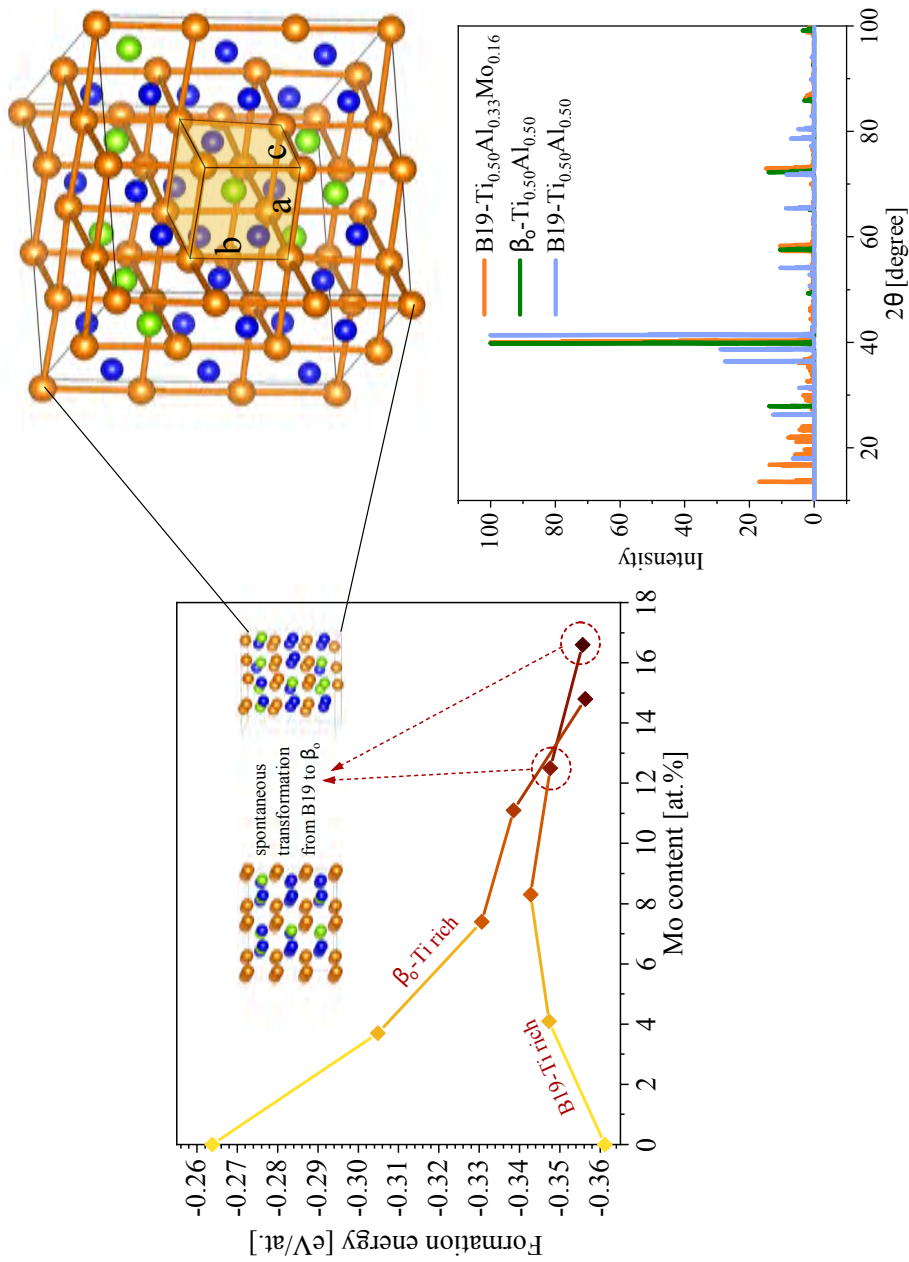


Figure 4.6: The calculated formation energy of the ordered  $\beta_0$ -TiAl and B19-TiAl as a function of the Mo content. The dashed orange arrows show spontaneous transformation as obtained during the structural relaxation at 0 K. The crystallography shows how the B19  $\rightarrow$   $\beta_0$  transformation happens along with fully relaxation by the VASP-SQS. relaxation. The low-right graph represents the predicted XRD pattern for  $\beta_0$  (green color), B19- $\text{Ti}_{0.5}\text{Al}_{0.5}$  (blue color) and B19- $\text{Ti}_{0.5}\text{Al}_{0.33}\text{Mo}_{0.16}$  compositions (orange color), which transforms spontaneously to  $\beta_0$  phase.

---

# Mechanical properties

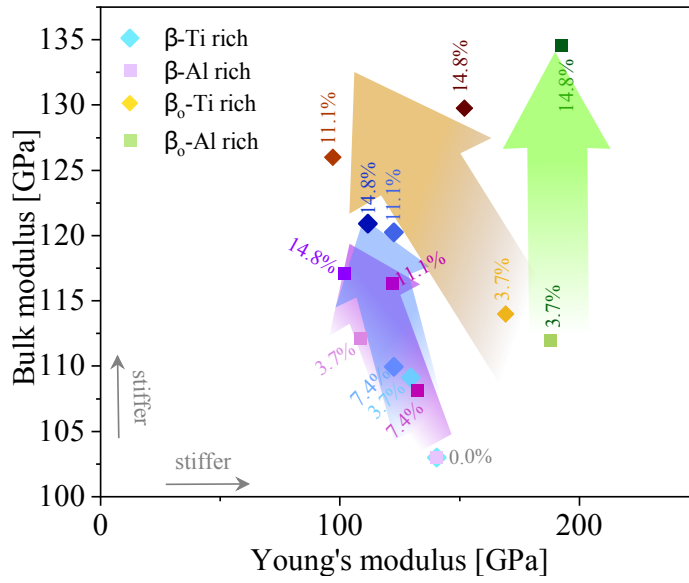
## 5.1 Elastic properties

We start with discussing the elastic response of  $\beta/\beta_o$  and  $\alpha'/\alpha'_2$  phases of the TiAl+Mo system. The polycrystalline elastic bulk and Young's moduli, obtained using the single crystal elastic constants  $C_{ij}$ , are shown in Fig. 5.1. To help the reader extracting the composition-related trends, points corresponding to the same phase and off-stoichiometry are underlain with colored arrows, highlighting the trends for increasing Mo content. As a general observation we state that bulk modulus increases with Mo content in the case of the ordered  $\beta_o$  phase; the uncertainty in elastic properties related to the structural instability of the ordered  $\beta_o$  prohibits identifying a clear trend for the Young's modulus. Bulk modulus increases with increasing Mo content also for the disordered  $\beta$  phase, but now the Young's modulus slightly drops. The same holds true for all hexagonal  $\alpha'$  and  $\alpha'_2$  variants. We note, however, that a closer inspection of the individual data-points reveals a significant scatter in some cases (i.e., the smallest bulk modulus value for  $\alpha'$  Al-rich compositions is actually obtained for 15.62 at.% Mo), and hence the absolute values should be taken with care.

Additionally it turns out that the (partially) ordered variants yield slightly larger Young's modulus (are thus stiffer) than the corresponding disordered phases with the same composition. This difference is larger for the Al-rich compositions (compare purple and green datasets in Fig. 5.1 than for the Ti-rich ones (blue and orange datasets in Fig. 5.1). Lastly, while the bulk moduli span over the same range of  $\approx 105$  GPa ( $x_{\text{Mo}} = 0$ ) to  $\approx 125$  GPa ( $x_{\text{Mo}} \approx 15$  at.%), ordered  $\beta_o$  phase is predicted to have  $\approx 10\%$  larger bulk modulus than corresponding disordered configurations  $\beta$ .

In general we conclude that Mo decreases compressibility ( $1/B$ ) of the  $\beta/\beta_o$  and  $\alpha'/\alpha'_2$  phases and leads to a slight softening of tensile modulus.

(a)



(b)

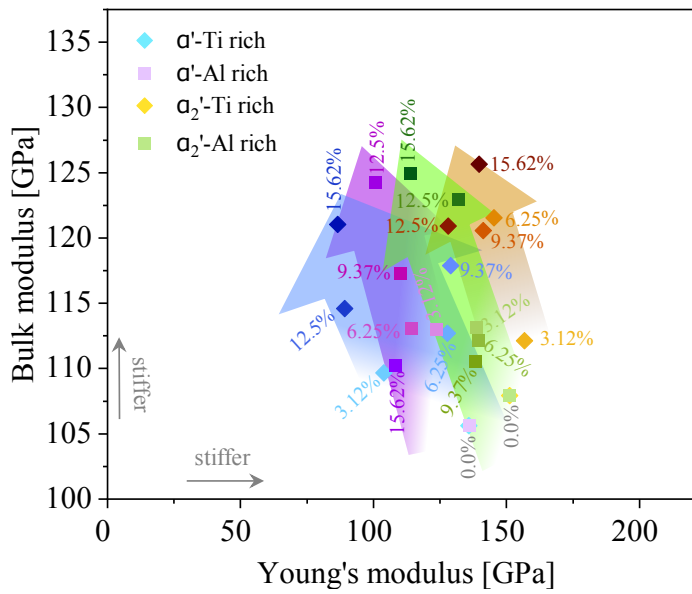


Figure 5.1: (Polycrystalline) bulk modulus,  $B$ , plotted against the polycrystalline Young's modulus,  $E$ , for (a) cubic  $\beta/\beta_0$  and (b) hexagonal  $\alpha'/\alpha'_2$  TiAl+Mo phases for various Mo compositions. The different sublattices (Ti-rich and Al-rich compositions) are shown with square and diamond symbols, respectively. Ordered and disordered/cubic and hexagonal phases are differentiated by colors (blue-pink/yellow-green respectively). The colored underlying arrows are guides for the eye to highlight Mo concentration trends.

## 5.2 Impact of Mo on ductility

Ductility and brittleness trends of materials are often assumed based on Pugh's  $B/G$  ratios and Cauchy pressure values, since both are readily available once the elastic properties are determined. According to the Pugh's criterion [113], a system is expected to behave in a ductile (brittle) manner if  $B/G > 1.75$  ( $B/G < 1.75$ ). Despite the exact statements above may be too strong (in particular the "magic" boundary for  $B/G$ ), they can be certainly used as a qualitative indicators for coherently comparing a series of systems/compositions.

The thus obtained trends are commonly supported by the Cauchy pressure behavior: Pettifor [114] has suggested that the more positive the Cauchy pressure is, the more dominant is metallic bonding (and hence the ductile behaviour), whereas negative values signify angular bonding and hence a brittle character. The Cauchy pressure for cubic systems is defined as  $C_{12} - C_{44}$ . Two analogous values exist for hexagonal crystals:  $C_{13} - C_{44}$  for  $\{100\}$  planes and  $C_{12} - C_{66}$  for the (001) plane. Therefore, we average these values with considering a twice larger weight on the first value (representing (100) and (010) planes) in order to get a single value, similarly as in the cubic case.

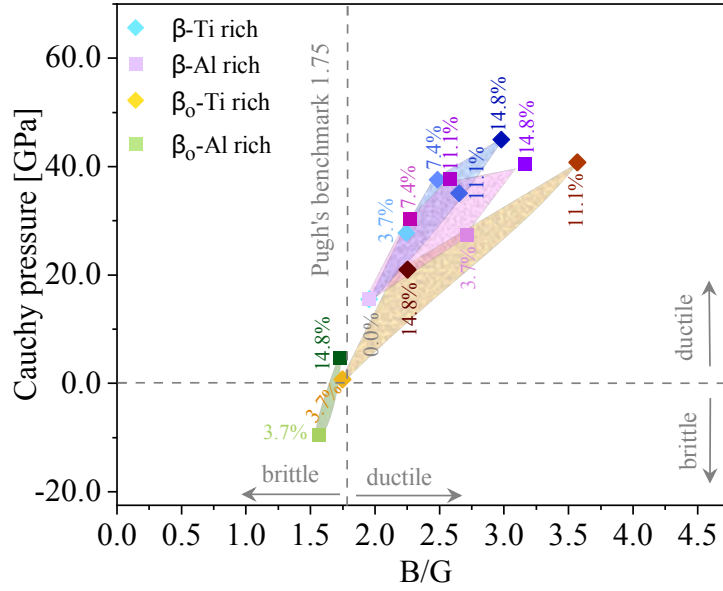
The results presented in Fig. 5.2 demonstrate that Mo increases ductility of all considered phases. Both factors,  $B/G$  as well as the Cauchy pressure, increase with increasing Mo content for all phases. This is mainly true for the Pugh's  $B/G$  ratio. It seems by increasing Mo in both Al/Ti-rich compositions the  $B/G$  ratio of disordered- $\beta$  is going up in positive range noticeably. The calculated Cauchy pressure trends also point towards increased ductility by increasing their values in to the positive range, i.e., suggesting more metallic bonding and thus more ductility. For the ordered- $\beta_0$  structure the Cauchy pressure stays positive, except for 3.7 at.% Mo at Ti-rich site, which is predicted to behave in a brittle manner. The  $B/G$  ratio and Cauchy pressure were calculated also the for hexagonal structures. In all Ti/Al-rich compositions (Fig. 5.2b)  $B/G > 1.75$  together with positive Cauchy pressure, therefore the actual composition is predicted to play an important role influencing ductility. This is for example evident for the disordered  $\alpha'$  compositions with high molybdenum impact (the blue and pink areas).

## 5.3 Elastic anisotropy

Elastic anisotropy directly impacts many mechanical and physical properties, for example phase transformations, dislocation dynamics and plastic deformation, or thermodynamic properties, to name a few [48]. While anisotropy is commonly described with the Zener's anisotropy ratio for the cubic materials, general elastic symmetry requires a slightly more involved treatment [115].



(a)



(b)

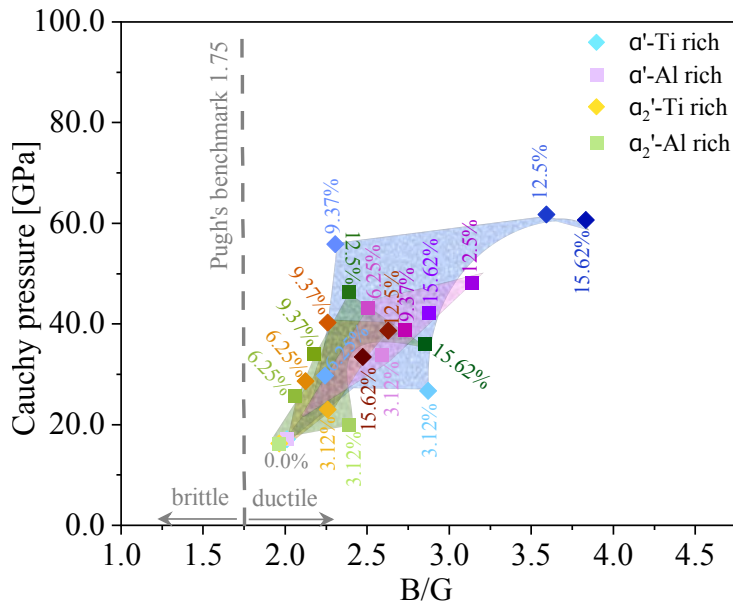


Figure 5.2: The Cauchy pressure versus  $B/G$  ratio of the TiAl+Mo system for (a) for cubic  $\beta/\beta_0$  and (b) hexagonal  $\alpha'/\alpha'_2$  structures. The different sublattices (Ti-rich and Al-rich compositions) are shown with square and diamond symbols, respectively. Ordered and disordered/cubic and hexagonal phases are differentiated by colors (blue-pink/yellow-green respectively). The shaded areas help to identify trends related to Mo content.

In this section we use two quantities which can be applied both to cubic and hexagonal systems. Considering the single-crystalline elastic constants  $C_{ij}$ , it is possible to calculate directionally-dependent Young's modulus  $E_{hkl}$  [48], which quantifies the elastic response in different crystallographic directions upon application of uniaxial stress (in the direction  $[h\ k\ l]$ ). Elastically isotropic materials (by definition) do not exhibit any directional dependence of  $E_{hkl}$  and Young's modulus is a constant. Hence, quantification of the difference between maximum and minimum value of  $E_{hkl}$  as a function of the crystallographic direction allows to 'quantify' deviation from an elastically isotropic material, which corresponds to  $E_{\max} - E_{\min} = 0$ . Obviously, such quantification can be applied to any arbitrary crystal symmetry. We note that in the case elastically isotropic materials, also the polycrystalline Voigt's ( $E_V$ ) and Reuss's ( $E_R$ ) averages are identical and equal to single-crystalline  $E$ .

As a second quantification we employ the polycrystalline shear anisotropy calculated as:

$$A_G = \frac{G_V - G_R}{G_V + G_R}, \quad (5.1)$$

where  $G_V$  and  $G_R$  are shear moduli within the Voigt's and Reuss's averages, respectively. Again,  $A_G = 0$  signifies elastic isotropy and a departure from zero represent the increasing anisotropy.

Two important aspects can be deduced from results shown in Fig. 5.3. Firstly, in particular the  $\beta_o$  phase shows a very strong anisotropy as the Mo increases (Fig. 5.3a), although the same compositional trend is observed also for the hexagonal phases (Fig. 5.3b). Interestingly, for the  $\beta_o$  phase, this effect is predicted to be maximum for  $x_{\text{Mo}} \approx 11$  at.% whereas for even higher Mo content, the significantly more isotropic behaviour is obtained. Generally, the cubic phases  $\beta/\beta_o$  are expected to be more anisotropic than the hexagonal  $\alpha'/\alpha'_2$  ones. Secondly, the disordered cubic phase  $\beta$  is clearly less isotropic than its ordered variant  $\beta_o$ . On the contrary, no significant difference between the (partially) ordered  $\alpha'_2$  and disordered  $\alpha'$  hexagonal variants is predicted.

The generally increased anisotropy due to Mo alloying may contribute to the (strain) hardening of those alloys [116], in addition to the impact of refinement and solid-solution hardening effects reported for the Ti-Al-Mo before [21].

It is noteworthy to mention, that values of  $E_{\min} \leq 0$  signify mechanical instability. If such situation happens in a certain direction, straining material along such direction would lead to negative strain energy and hence to a spontaneous transformation to other structure. Such situation is the case for low-Mo compositions ( $x_{\text{Mo}} \leq 8$  at.%) in the Al-rich ordered  $\beta_o$  phase, which have been, however, excluded already by the  $\lambda_{\min} > 0$  criterion (Sec. 4.2.2 and Fig. 4.3).

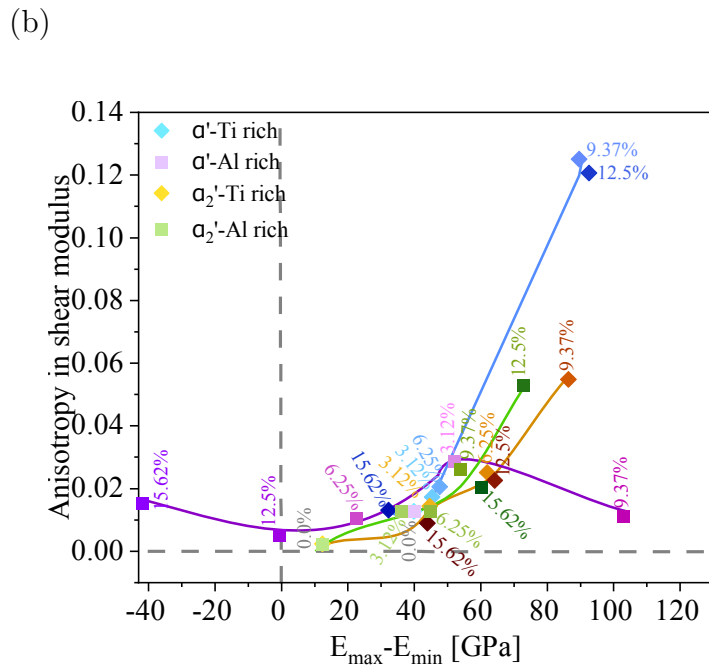
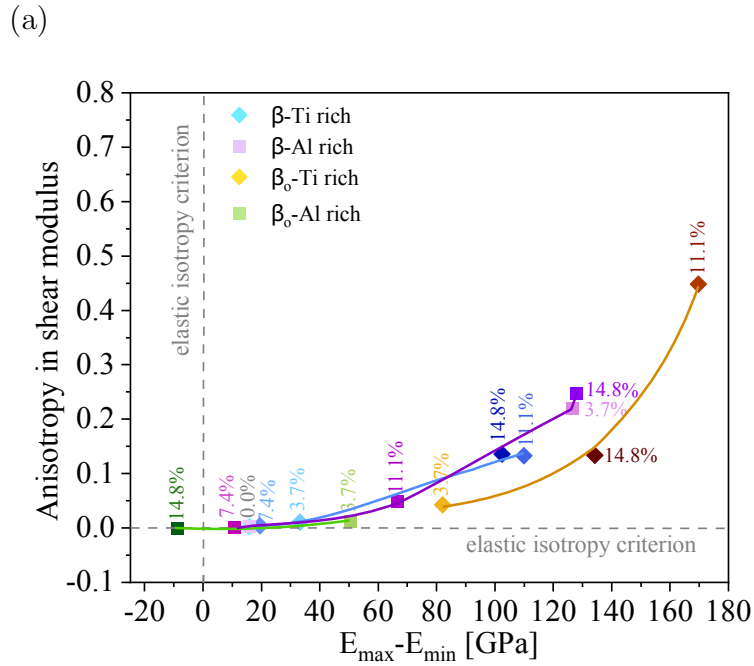


Figure 5.3: Quantification of the elastic anisotropy using the shear anisotropy,  $A_G$ , versus directional Young's modulus of TiAl+Mo compositions, a) for the cubic phases and b) for the hexagonal structures. The different sublattices used for Mo substitution (Ti/Al-rich) are specified by square and diamond symbols respectively, further, ordered and disordered phases ( $\beta$ - $\beta_0$ / $\alpha$ - $\alpha_2$ ) are differentiated by colors (blue-pink/yellow-green respectively).

# Quasi-harmonic approximation: towards thermal expansion

This chapter is based on an own publication [50]

## 6.1 Temperature dependency of volume and $c/a$ ratio

Figure 6.1 shows the temperature dependence of volume and  $c/a$  ratio for the intended phases,  $\gamma$  (orange curves) and  $\alpha_2$  (blue curves), by applying the two above explained approaches, gs-cs (dashed lines) and to-cs (solid lines). Results in Fig. 6.1a suggests identical behaviour for  $\alpha_2$ -Ti<sub>3</sub>Al phase considering both approaches. On the contrary, there are obvious differences in the case of  $\gamma$ -TiAl. A rapid, non-linear increase (specifically, for the gs-cs approach) of the specific volume above room temperature (RT),  $\approx 298\text{K}$ , is predicted for  $\gamma$ -TiAl.

According to Fig. 6.1b, while the absolute values of the  $c/a$  ratio for the hexagonal  $\alpha_2$ -Ti<sub>3</sub>Al structure are nearly the same, a significant discrepancy between the two approaches is predicted for the tetragonal  $\gamma$ -TiAl phase. Surprisingly, the the methods are showing inverse behaviour for the two structures. Namely, while the gs-cs( $\gamma$ ) approach leads to temperature-induced increase of  $c/a$ , its value decreases in the case of the  $\alpha_2$  phase, and a vice verse trend is obtained for the to-cs approach (solid lines) by considering both structures.

It is possible to predict the lattice parameters  $a$  and  $c$ , in terms of specific volume and  $c/a$  and subsequently, the lattice thermal expansion coefficients (see Fig. 6.2),  $\alpha_a$  and  $\alpha_c$  can be obtained by solving the Eq. (2.60).

As displayed in Fig. 6.2a, a marginally larger  $\alpha_a$  than  $\alpha_c$  is predicted for all temperatures in case of  $\alpha_2$ -Ti<sub>3</sub>Al structure. Noticeably, while the  $\alpha_c$  of the  $\alpha_2$ -Ti<sub>3</sub>Al structure is going

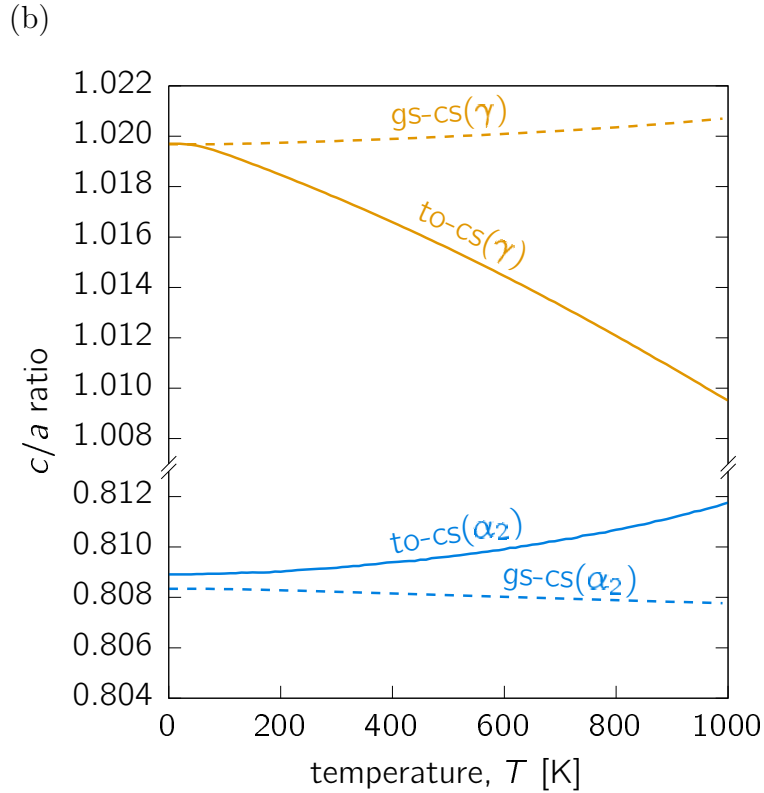
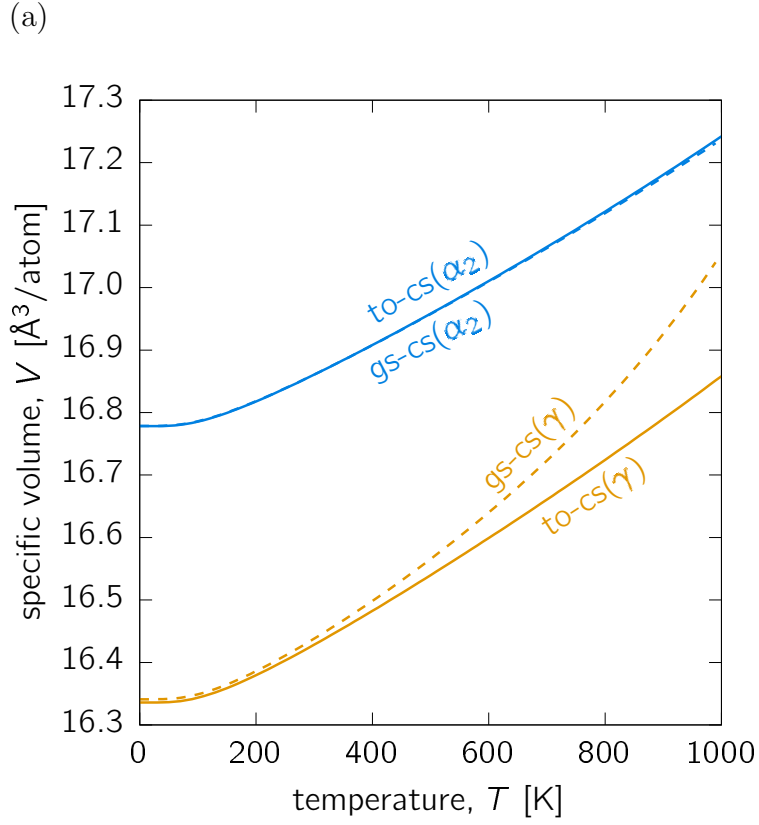


Figure 6.1: (a) Specific volume and (b)  $c/a$  ratio as functions of temperature for the  $\alpha_2$ - $\text{Ti}_3\text{Al}$  (blue) and  $\gamma$ - $\text{TiAl}$  (orange) phases predicted using quasi-harmonic approximation with cell shape optimised at 0 K (dashed, label ‘gs-cs’ (ground state optimised cell shape)) and at every temperature (solid line, label ‘to-cs’ (temperature optimised cell shape)).

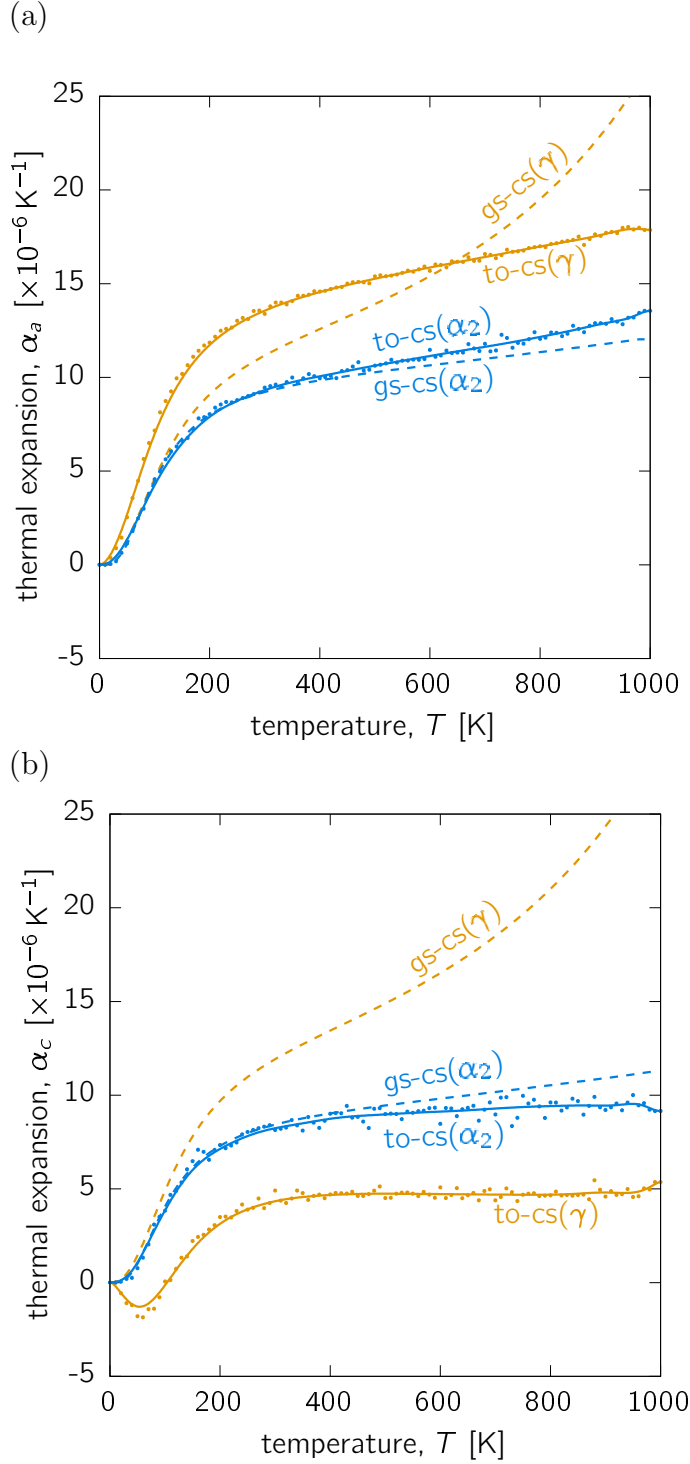


Figure 6.2: Lattice thermal expansion along (a)  $a$ -direction,  $\alpha_a$ , and (b)  $c$ -direction,  $\alpha_c$ , as functions of temperature for the  $\alpha_2$ -Ti<sub>3</sub>Al (blue) and  $\gamma$ -TiAl (orange) phases predicted using quasi-harmonic approximation with cell shape optimised at 0 K (dashed, label ‘gs-cs’) and at every temperature (solid line, label ‘to-cs’). The data points shown by dots are the actual numerically calculated values using Eq. (2.60). The smooth curves are ‘guides for the eyes’ from interpolation using Bezier curves.

to be saturated above RT around  $10 \times 10^{-6} \text{ K}^{-1}$  (Fig. 6.2b),  $\alpha_a$  is still increasing above RT and even higher than  $10 \times 10^{-6} \text{ K}^{-1}$  above  $\sim 600 \text{ K}$  (Fig. 6.2a). Importantly, there are no significant differences between the predicted values by gs-cs and to-cs methods. The obtained differences are of the same order as the scatter of the numerical noise imposed by the to-cs method, represented by the individual data points in Fig. 6.2.

The  $\gamma$ -TiAl structure behaves differently. It seems for both  $\alpha_a$  and  $\alpha_c$ , the gs-cs approach yields a very similar, strongly temperature dependent behaviour as well as strong temperature dependency. It is a consequence of its large volume thermal expanding of volume as shown in Fig. 6.1a. Contrarily, this structure shows a large TEC values  $\alpha_a$  (*a*-direction) of  $\sim 15 \times 10^{-6} \text{ K}^{-1}$  only for  $\alpha_a$  (*a*-direction) above RT using the to-cs approach, whereas a 3-fold smaller values of  $\sim 5 \times 10^{-6} \text{ K}^{-1}$  are predicted for  $\alpha_c$  (*c*-direction). This behavior can be interpreted a consequence of the strong temperature dependence of  $c/a$ .

In summary, while the computationally more demanding to-cs method does not yield too different temperature dependence of the structural properties in comparison with the simpler gs-cs approach for the  $\alpha_2$ -Ti<sub>3</sub>Al, non-negligible differences are obtained in the case of the  $\gamma$ -TiAl.

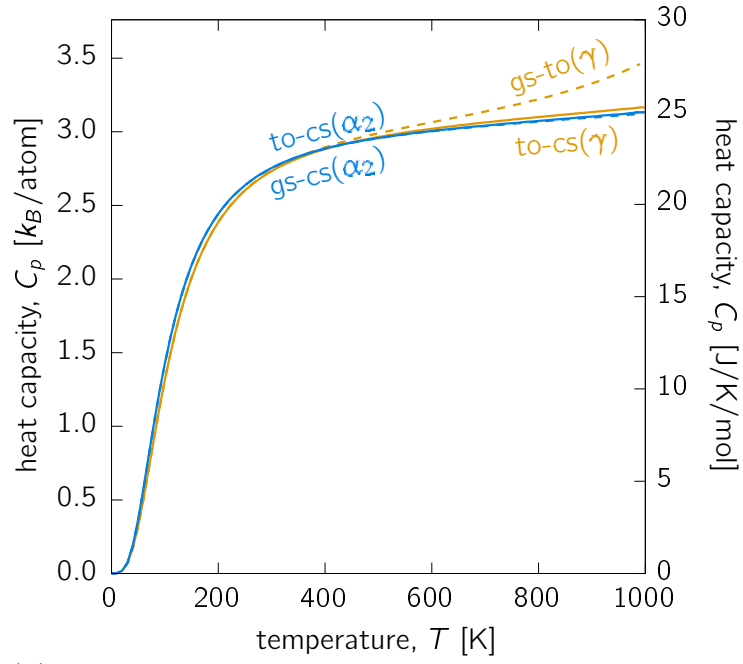
## 6.2 Heat capacity and bulk modulus

The heat capacity can be calculated using the computed vibrational entropy by the Helmholtz free energy. In fact, it is expressed in the relevant literature [117, 118] as the only important contribution when dealing with non-magnetic materials at temperatures far below the melting point. Due to that, some other thermal-dependent properties can be calculated by the here obtained thermodynamic potentials. The heat capacity,  $C_p$ , at constant (ambient) pressure was evaluated according to Eq. (2.61). The calculated values for the two phases are almost identical, in particular from the to-cs treatment (Fig. 6.3b). This result could be intuitively understood by the fact that the molar heat capacities of Al and Ti are very similar [119].

Bulk modulus can be estimated by fitting the Helmholtz free energy surface at a fixed temperature with the Birch-Murnaghan equation of state. Obviously, the bulk modulus of  $\gamma$ -TiAl is smaller than  $\alpha_2$ -Ti<sub>3</sub>Al (Fig. 6.3b). Moreover, the softness of bulk modulus is predicted to reduce by  $\sim 12\%$  with increasing temperature from 0 to 770 K ( $\sim 500^\circ\text{C}$ ), and similarly,  $\sim 12\%$  between RT and  $500^\circ\text{C}$  for both structures using the ‘to-cs’ approach.

Significantly different is only the gs-cs temperature dependence for the  $\gamma$ -TiAl, which yields a drop of over 30% between 0 and 770 K, further underlying that this approach is not reasonable for the  $\gamma$ -TiAl, as already demonstrated by other properties.

(a)



(b)

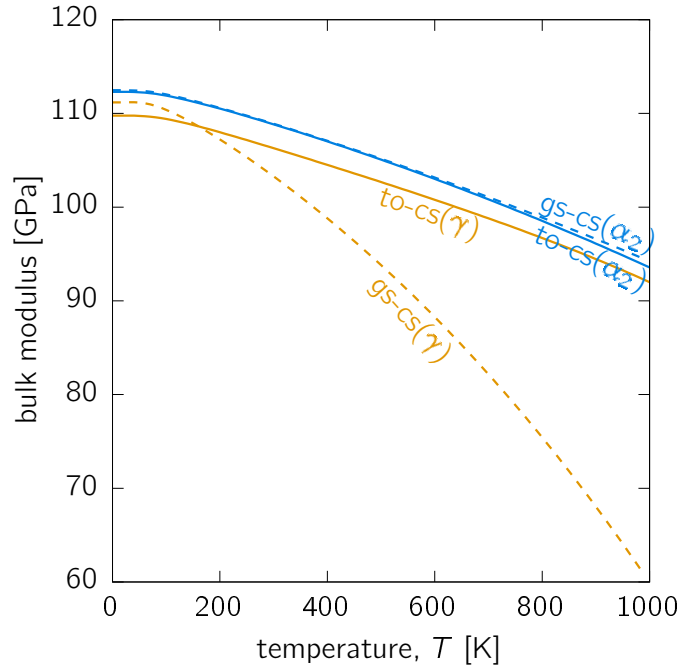


Figure 6.3: (a) Heat capacity at constant (ambient) pressure and (b) bulk modulus of the  $\alpha_2$  (blue lines) and  $\gamma$  (orange lines) phase as functions of temperature evaluated within the gs-cs (dashed lines) and to-cs (solid lines) approach.



## 6.3 Conclusion

Thermal properties, with a special focus on structural analysis of temperature dependent lattice parameters and coefficients of thermal expansion of tetragonal  $\gamma$ -TiAl and hexagonal  $\alpha_2$ -Ti<sub>3</sub>Al phases of binary TiAl system, were calculated using first principles methods. We put our attention on testing whether the  $c/a$  ratio is purely a function of volume independent of temperature, or whether temperature and volumetric effects have to be separated. Our calculations show that in the case of the  $\gamma$ -TiAl phase significant differences are obtained, while both approaches yield comparable results for the hexagonal  $\alpha_2$ -Ti<sub>3</sub>Al phase.

## 6.4 Analytical fits

The above discussed thermodynamic quantities calculated using the ‘to-cs’ approach were fitted with a polynomial of the form

$$X(T) = a_0^X + \sum_{i=1}^4 a_i^X T^i + \sum_{i=1}^4 b_i^X \frac{1}{T^i} + c^X \ln(T) . \quad (6.1)$$

This function fits accurately all obtained data within the temperature window from 0 to 1000 K. The fitted coefficients for  $X = F$  (Helmholtz free energy),  $C_p$  (molar heat capacity),  $B$  (bulk modulus),  $\alpha_a$  and  $\alpha_c$  (TEC in the  $a$  and  $c$  directions) are summarised in Tables 6.2 and 6.1, and the polynomial fits are presented in Fig. 6.4. The calculated dependencies provide a consistent set of material constants which could serve, e.g., for CALPHAD-like modelling.

Table 6.1: Fitted coefficients according to Eq. (6.1) for the calculated thermodynamic properties of the  $\gamma$ -TiAl phase.  $F$  is Helmholtz free energy [eV/at.],  $C_p$  is molar heat capacity at constant pressure [J/K/mol] (mol of atoms),  $B$  is bulk modulus [GPa] and  $\alpha_a$  and  $\alpha_c$  are TEC in the [100] and in the [001] directions [ $\text{K}^{-1}$ ].

	$F$ [eV/at.]	$C_p$ [J/K/mol]	$B$ [GPa]	$\alpha_a$ [ $\text{K}^{-1}$ ]	$\alpha_c$ [ $\text{K}^{-1}$ ]
$a_0$	$-6.4187 \times 10^{+00}$	$-3.4558 \times 10^{+01}$	$1.1499 \times 10^{+02}$	$-3.6457 \times 10^{-05}$	$-3.8562 \times 10^{-04}$
$a_1$	$-1.8683 \times 10^{-04}$	$-4.2978 \times 10^{-02}$	$-1.8487 \times 10^{-02}$	$-7.0845 \times 10^{-08}$	$-3.9878 \times 10^{-07}$
$a_2$	$-3.7211 \times 10^{-07}$	$5.0198 \times 10^{-05}$	$1.5144 \times 10^{-06}$	$8.5104 \times 10^{-11}$	$4.5801 \times 10^{-10}$
$a_3$	$1.5691 \times 10^{-10}$	$-3.5403 \times 10^{-08}$	$-6.3023 \times 10^{-10}$	$-5.4782 \times 10^{-14}$	$-3.2999 \times 10^{-13}$
$a_4$	$-3.7138 \times 10^{-14}$	$1.0447 \times 10^{-11}$	$-2.0214 \times 10^{-12}$	$1.4449 \times 10^{-17}$	$1.0165 \times 10^{-16}$
$b_1$	$3.4305 \times 10^{+00}$	$2.9671 \times 10^{+02}$	$-2.1317 \times 10^{+02}$	$-7.2401 \times 10^{-04}$	$6.0522 \times 10^{-03}$
$b_2$	$-6.0577 \times 10^{+01}$	$-2.0669 \times 10^{+01}$	$5.5554 \times 10^{+03}$	$3.6802 \times 10^{-02}$	$-9.7074 \times 10^{-02}$
$b_3$	$6.3758 \times 10^{+02}$	$-3.9874 \times 10^{+04}$	$-6.9252 \times 10^{+04}$	$-5.5989 \times 10^{-01}$	$9.1203 \times 10^{-01}$
$b_4$	$-2.6280 \times 10^{+03}$	$2.7003 \times 10^{+05}$	$3.1027 \times 10^{+05}$	$2.7435 \times 10^{+00}$	$-3.4160 \times 10^{+00}$
$c$	$4.4277 \times 10^{-02}$	$7.9870 \times 10^{+00}$	$-4.5702 \times 10^{-01}$	$1.1764 \times 10^{-05}$	$8.0199 \times 10^{-05}$

Table 6.2: Fitted coefficients according to Eq. (6.1) for the calculated thermodynamic properties of the  $\alpha_2$ -Ti<sub>3</sub>Al phase.  $F$  is Helmholtz free energy [eV/at.],  $C_p$  is molar heat capacity at constant pressure [J/K/mol] (mol of atoms),  $B$  is bulk modulus [GPa] and  $\alpha_a$  and  $\alpha_c$  are TEC in the (0001) plane and in the [0001] direction [ $\text{K}^{-1}$ ].

	$F$ [eV/at.]	$C_p$ [J/K/mol]	$B$ [GPa]	$\alpha_a$ [ $\text{K}^{-1}$ ]	$\alpha_c$ [ $\text{K}^{-1}$ ]
$a_0$	$-7.3540 \times 10^{+00}$	$-2.0371 \times 10^{+01}$	$1.1716 \times 10^{+02}$	$-1.6008 \times 10^{-04}$	$5.4128 \times 10^{-05}$
$a_1$	$-2.1062 \times 10^{-04}$	$-3.1196 \times 10^{-02}$	$-1.4167 \times 10^{-02}$	$-1.8981 \times 10^{-07}$	$2.5208 \times 10^{-08}$
$a_2$	$-3.6153 \times 10^{-07}$	$3.8017 \times 10^{-05}$	$-4.9187 \times 10^{-06}$	$2.3150 \times 10^{-10}$	$-3.7248 \times 10^{-11}$
$a_3$	$1.5105 \times 10^{-10}$	$-2.7416 \times 10^{-08}$	$-6.5580 \times 10^{-10}$	$-1.6951 \times 10^{-13}$	$3.9920 \times 10^{-14}$
$a_4$	$-3.5505 \times 10^{-14}$	$8.2107 \times 10^{-12}$	$6.6516 \times 10^{-14}$	$5.2923 \times 10^{-17}$	$-1.6988 \times 10^{-17}$
$b_1$	$3.4451 \times 10^{+00}$	$1.9711 \times 10^{+01}$	$-1.6377 \times 10^{+02}$	$1.8767 \times 10^{-03}$	$-2.2451 \times 10^{-03}$
$b_2$	$-5.9472 \times 10^{+01}$	$5.5440 \times 10^{+03}$	$3.9202 \times 10^{+03}$	$-1.9966 \times 10^{-02}$	$6.8760 \times 10^{-02}$
$b_3$	$6.1738 \times 10^{+02}$	$-1.0178 \times 10^{+05}$	$-4.6560 \times 10^{+04}$	$1.1511 \times 10^{-01}$	$-9.5646 \times 10^{-01}$
$b_4$	$-2.5244 \times 10^{+03}$	$5.3097 \times 10^{+05}$	$2.0274 \times 10^{+05}$	$-2.3378 \times 10^{-01}$	$4.5685 \times 10^{+00}$
$c$	$4.6143 \times 10^{-02}$	$5.1928 \times 10^{+00}$	$-5.4515 \times 10^{-01}$	$3.5711 \times 10^{-05}$	$-7.7496 \times 10^{-06}$

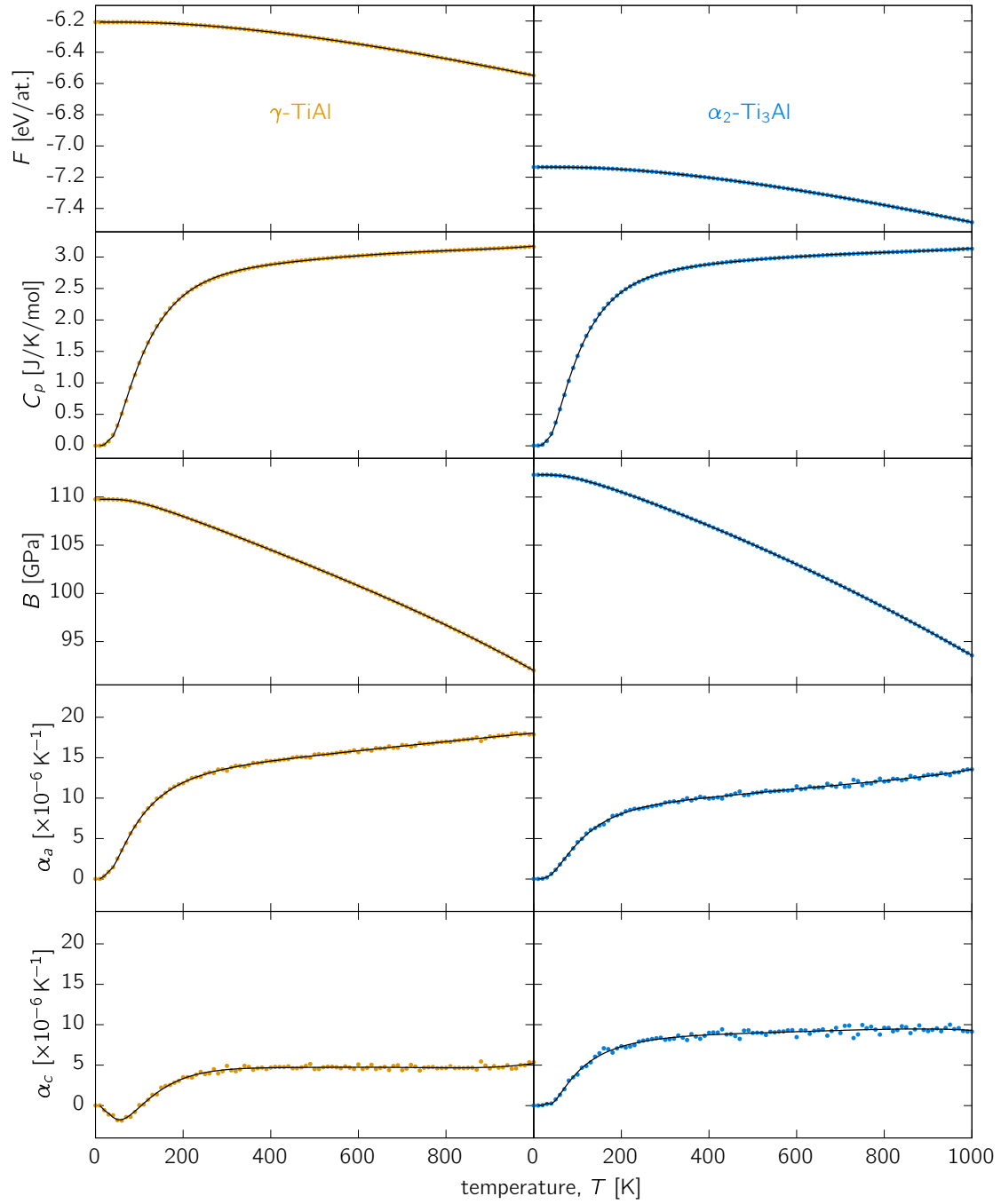


Figure 6.4: Fits of ‘to-cs’ calculated thermodynamic properties using Eq. (6.1) and coefficients from Table 6.1 ( $\gamma$ -TiAl, left column) and Table 6.2 ( $\alpha_2$ -Ti<sub>3</sub>Al, right columns). The actual calculated data are shown by the small coloured points while the fits are thin continuous black lines.

# Ordering temperatures as a function of Mo

The previous chapters have presented a systematic study on structural, energetic and elastic properties of the TiAl+Mo phases. The focused was laid on a comparing properties of ordered ( $\beta_o$ , B19, partly-ordered  $\alpha'_2$ ,  $\gamma$ ) variants with their chemically disordered counterparts. Knowledge of the energy differences related to the ordering state enables establishing ordering temperatures. To do so, we assign the whole energy gain change upon ordering to the loss of the configurational entropy.

## 7.1 Configurational entropy

Suppose that the atomic concentrations of Ti, Al and Mo are  $x_{\text{Ti}}$ ,  $x_{\text{Al}}$  and  $x_{\text{Mo}}$  ( $x_{\text{Ti}} + x_{\text{Al}} + x_{\text{Mo}} = 1$ ). The configurational entropy (per atom) is defined as

$$S_{\text{conf}} = -k_B \sum_{i=\text{Ti,Al,Mo}} x_i \ln x_i \quad (7.1)$$

and the corresponding configurational part of the free energy is  $F_{\text{conf}} = -TS_{\text{conf}}$ . The entropy term is different for the ordered phases, in which the chemical disorder is realized only on one sublattice (half of the total number of atomic sites), and in fully disordered cases where all lattice sites are randomly populated with Ti, Al and Mo. Let us demonstrate this on an example of Ti-rich compositions; Al-rich compositions are treated analogously. The entropy of the disordered case is given by Eq. (7.1). In the ordered cases, the Ti sublattice amounts to half of the sites, but contains no disorder. Hence

$S_{\text{conf,Ti subl.}} = 0$ . The entropy on the Al sublattice is then given by

$$\begin{aligned} S_{\text{conf,Al}} &= -\frac{k_B}{2} \sum_{i=\text{Al,Mo}} (2x_i) \ln(2x_i) \\ &= -\frac{k_B}{2} \underbrace{((2x_{\text{Mo}}) \ln(2x_{\text{Mo}}) + (1 - 2x_{\text{Mo}}) \ln(1 - 2x_{\text{Mo}}))}_A. \end{aligned} \quad (7.2)$$

The factor  $1/2$  in front of the sum relates to the fact, that the disorder is only on 1 sublattice; the factor 2 in the addends corresponds to the Al and Mo concentration on the Al sublattice only. Finally we note that the factors  $1/2$  and 2 are related to the fact that both sublattices in our particular case of  $\beta_o$  and B19 phases contain the same amount of sites.

Omitting all other contributions to the free energy but configurational entropy, and equating the free energies of ordered and disordered phases at the ordering temperature  $T_{\text{ord}}$ , one obtains:

$$E_0(\beta_o) + \frac{T_{\text{ord}}k_B}{2} \sum_{i=\text{Al,Mo}} 2x_i \ln(2x_i) = E_0(\beta) + T_{\text{ord}}k_B \sum_{i=\text{Ti,Al,Mo}} x_i \ln x_i, \quad (7.3)$$

where  $E_0(\beta_o)$  and  $E_0(\beta)$  are total (or formation) energies (per atom) of the  $\beta_o$  and  $\beta$  phases, respectively, at  $T = 0\text{K}$ . Remembering, that for Ti-rich compositions we fix  $x_{\text{Ti}} = 0.5$ , the above expression yields

$$T_{\text{ord}} = \frac{E_0(\beta) - E_0(\beta_o)}{k_B \ln 2}. \quad (7.4)$$

It is trivial to show that the same is true also for the Al-rich compositions. Identical formula applies also to binary  $\alpha' \rightarrow \text{B19}$  ordering temperature.

In the case of hexagonal  $\alpha'/\alpha'_2$  phases, the corresponding energy differences  $E_0(\alpha') - E_0(\alpha'_2)$  replace  $E_0(\beta) - E_0(\beta_o)$  in the Eq. (7.4). Further by considering  $\alpha'_2$  as a partially ordered structure, the configurational entropy is related to the mixing of  $\frac{2}{3}\text{Ti}$  and  $\frac{1}{3}\text{Al}$  on the Ti-sublattice in the  $\text{D0}_{19-\alpha_2}$  phase. The Al sublattice of the parent  $\text{Ti}_3\text{Al}$  is fully populated with Al, hence corresponding entropy is:

$$S_{\text{Al}} = 0. \quad (7.5)$$

This concerns  $\frac{1}{4}$  of all overall sites (the Al sublattice in  $\text{Ti}_3\text{Al}$ ).

Our calculations shown that in the case of Ti-rich compositions, Mo preferentially substitutes for Al on the Ti sublattice. Therefore, the Ti sublattice ( $\frac{3}{4}$  of all sites) contains all Ti and Mo atoms, and remaining Al atoms. From overall mole fraction  $x_{\text{Al}}$  of Al atoms,  $\frac{1}{4}$  is on the Al sublattice; the Ti sublattice is thus randomly populated with  $x_{\text{Al}} - \frac{1}{4}$  Al

atoms,  $x_{Ti}$ , Ti atoms and  $x_{Mo}$  Mo atoms. The relative concentrations on the Ti sublattice are

$$\begin{aligned}x'_{Ti} &= \frac{4}{3}x_{Ti} , \\x'_{Mo} &= \frac{4}{3}x_{Mo} , \\x'_{Al} &= \frac{4}{3}\left(x_{Al} - \frac{1}{4}\right)\end{aligned}$$

with

$$\sum_{i=Ti,Al,Mo} x'_i = 1 .$$

Therefore the entropy on Ti sublattice is

$$S_{Ti} = -k_B \sum_{i=Ti,Al,Mo} x'_i \ln x'_i. \quad (7.6)$$

The total entropy (per atom) is therefore:

$$S(\alpha'_2) = \frac{1}{4}S_{Al} + \frac{3}{4}S_{Ti} = \frac{3}{4}S_{Ti}. \quad (7.7)$$

The ordering temperature can be obtained by equating free energies (containing configurations entropies) of fully disordered and partially ordered systems at temperature  $T_{ord}$ :

$$E_0(\alpha') + T_{ord}k_B S(\alpha') = E_0(\alpha'_2) + T_{ord}k_B S(\alpha'_2) \quad (7.8)$$

which leads to (after a couple of algebraic simplifications)

$$E_0(\alpha') - E_0(\alpha'_2) = T_{ord}k_B \left[ \frac{3}{4} \ln \frac{4}{3} + \left(x_{Al} - \frac{1}{4}\right) \ln \left(x_{Al} - \frac{1}{4}\right) - x_{Al} \ln x_{Al} \right] \quad (7.9)$$

and finally

$$T_{ord} = \frac{E_0(\alpha') - E_0(\alpha'_2)}{k_B \left[ \frac{3}{4} \ln \frac{4}{3} + \left(x_{Al} - \frac{1}{4}\right) \ln \left(x_{Al} - \frac{1}{4}\right) - x_{Al} \ln x_{Al} \right]}. \quad (7.10)$$

## 7.2 Ordering temperature

In the below we present results of a very simple approach making use of the readily available quantities to estimate the ordering temperature,  $T_{ord}$ , using the formalism described in previous Sec. 7.1.

A series of ordered ( $\beta_o$ , B19, partly-ordered  $\alpha'_2$ ) phases and their chemically disordered counterparts ( $\beta$ ,  $\alpha'$ ) are discussed in the present work and have been reported to undergo ordering transformations.

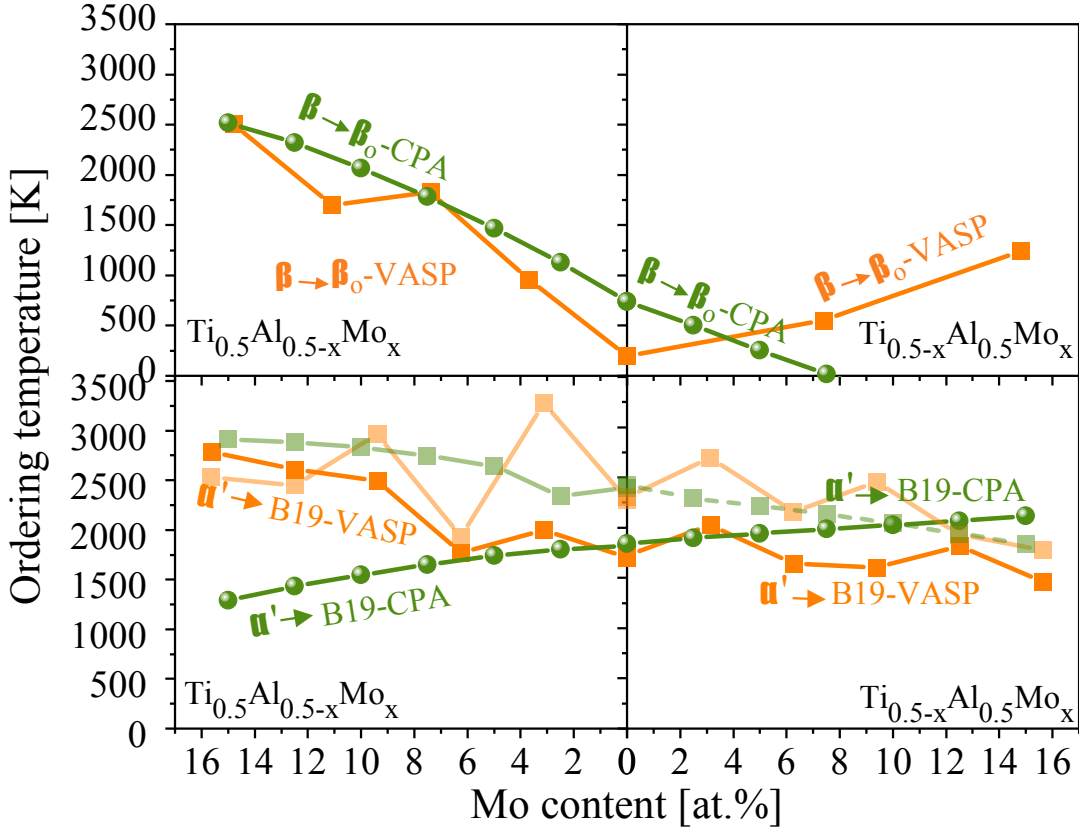


Figure 7.1: The ordering temperatures of  $\beta \rightarrow \beta_0$ , and  $\alpha' \rightarrow \alpha'_2$  (transparent) and  $\alpha' \rightarrow \text{B19}$  Ti and Al rich compositions. The green lines correspond to the EMTO-CPA result and orange lines are the VASP result. The transparent lines correspond to the  $\alpha' \rightarrow \alpha'_2$ .

As demonstrated in Fig. 7.1, the ordering temperature of  $\beta \rightarrow \beta_0$ -binary TiAl, is predicted  $\approx 250$  K, and increases with Mo up to  $\approx 2500$  K for Ti-rich compositions. The EMTO-CPA predicts somewhat higher temperature (e.g.  $\approx 1000$  K for binary TiAl), but both methods qualitatively agree on the increasing trend in  $T_{\text{ord}}$  with adding Mo. In contrast to that, the ordering temperatures of Al-rich cubic compositions show different trends considering two approaches. As discussed in Sec. 4.3, neglecting the lattice distortions leads to energetically preferring the disordered  $\beta$  phase over  $\beta_0$  for high Mo-containing Al-rich compositions, hence leading to the non-physical prediction of  $T_{\text{ord}} < 0$  K for  $x_{\text{Mo}} \approx 8$  at.% and more.

Similar trends in  $T_{\text{ord}}$  are predicted for the hexagonal phases using both methods. In the case of  $\alpha' \rightarrow \text{B19}$  ordering temperature, the supercell VASP-SQS calculations fail to predict any smooth trend.  $T_{\text{ord}}$  varies between  $\approx 1400$  K and  $\approx 2500$  K. The EMTO-CPA calculations predict uniform increase of  $T_{\text{ord}}$  for decreasing (increasing) Mo content for

the Ti-rich (Al-rich) compositions. Qualitatively opposite trends are obtained for the partial ordering  $\alpha' \rightarrow \alpha'_2$ . In both cases, the ordering temperatures are very high, even above the melting temperature of 1729 K for the binary  $\text{Ti}_{0.5}\text{Al}_{0.5}$  [120].

We therefore conclude that this rather simplistic approach neglecting other entropic contributions (e.g., vibrational), treating sublattices as independent and non-interacting systems, and approximating fully disordered systems with finite-sized supercells (in the case of EMTO-CPA), is not sufficient to predict order-disorder transition temperatures. Detailed investigation including evaluation of pair interactions and incorporating Monte Carlo simulations beyond the scope of this thesis and are reported elsewhere [121].



---

# Bcc to fcc phase transformations

This chapter is based on an own publication [14].

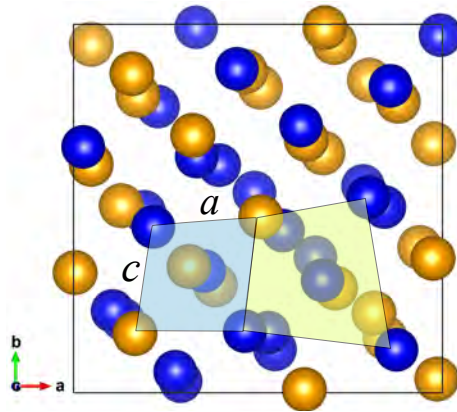
## 8.1 Ground-state properties

The structural instability of some phases emerges already when searching for their minimum-energy configurations. In particular, there is a significant dependency of a computational model of the disordered  $\beta$ -TiAl phase on constraints applied during its structural relaxation. When the simulation box shape is fixed to a cubic one (termed ‘ionic relaxation’ in Chap. 4), the structural relaxation results in large, seemingly disordered, local atomic displacements, see Fig. 8.1a, while a full structural relaxation leads to a significant change of the cell shape (see Fig. 8.1b).

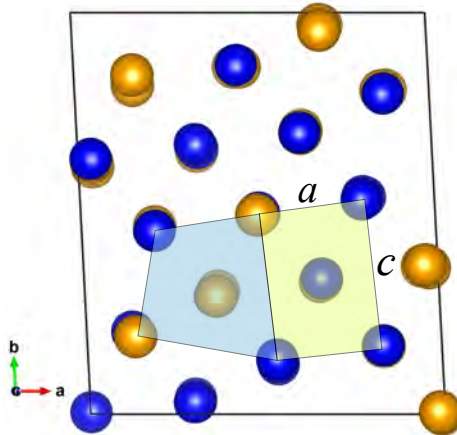
For example, one local structural motif (lemon trapezium) in the former case changes to a clear rectangle with  $a = 2.886 \text{ \AA}$  and  $c = 4.061 \text{ \AA}$  upon a full relaxation. These values are notably similar to the  $\gamma$ -TiAl lattice parameters expressed in a tetragonal body-centered cell:  $a = 2.826 \text{ \AA}$  and  $c = 4.062 \text{ \AA}$  [122]. On the other hand, the blue area in Fig. 8.1a resembling a sheared square ( $a = 3.167 \text{ \AA}$ ,  $c = 3.417 \text{ \AA}$ ), changes to a general non-rectangular shape in Fig. 8.1b. Consequently, also the disordered structures spontaneously transform similar to  $\beta_o \rightarrow \gamma$ , however, the transformation  $\beta \rightarrow \gamma_{\text{dis}}$  is to be expected to take place only locally.

The structural relaxations in the disordered  $\beta$ -TiAl structure, can also be visualized as a histogram of bond angles (Fig. 8.1c) corresponding to the fully relaxed structure from Fig. 8.1b. When compared with the structural fingerprints of ideal ordered  $\beta_o$ -TiAl phase (black) and ordered  $\gamma$ -TiAl structure (red), a significant overlap with the  $\gamma$  structure is apparent. However, some bond angles around  $110^\circ$  still resemble the initial (unrelaxed) disordered  $\beta$  (ordered  $\beta_o$ ) structure, while others around  $145^\circ$  do not agree with either

(a)



(b)



(c)

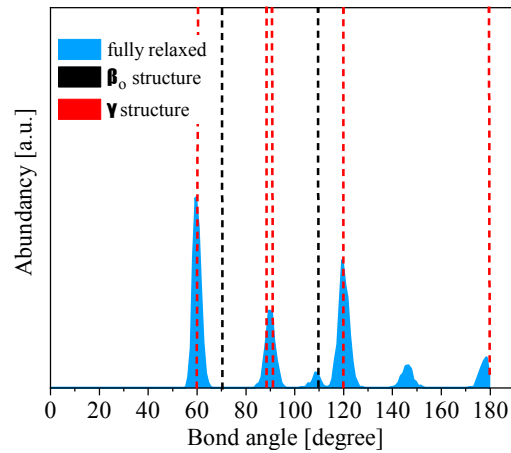


Figure 8.1: Schematic visualization of the minimum-energy configuration of the disordered  $\beta$ -TiAl phase when (a) preserving the overall cubic cell shape and (b) when fully relaxing the supercell. The blue and green motifs result in significantly different shapes depending on the relaxation mode. (c) Histogram of bond angles of the fully relaxed structure.

of the two fingerprints. This only further highlights the complexity and richness of the structural relaxations demonstrating the structural instability of the bcc-based TiAl (see also our previous results in Ref. [109]). In what follows, we used models with desired (fixed) cell shape and fully-relaxed internal degrees of freedom (atomic positions).

## 8.2 Tetragonal Bain’s path for the stoichiometric TiAl phases

We proceed with investigation of configurations along the Bain’s tetragonal deformation path  $\beta_o \leftrightarrow \gamma$  as described in detail in Sec. 3.3.1. The lattice parameters were set according to Eqs. (3.1) and (3.2). The atomic positions remain fixed by the crystal symmetry of the ordered  $\beta_o$  and  $\gamma$  TiAl phases. As shown in Fig. 8.2, the energy extrema correspond to  $\Delta = 0$  ( $\beta_o$ -TiAl, maximum) and  $\Delta = 1$  ( $\gamma$ -TiAl, minimum). The latter is consistent with the fact that the  $\gamma$  phase is the ground state for stoichiometric  $\text{Ti}_{0.5}\text{Al}_{0.5}$ . Both of the above mentioned extrema can be understood in terms of so-called symmetry-dictated extrema. (Note, that while our transformations are not volume conserving the energies change by less than 0.1 meV/at. when the volume is kept constant, well below the accuracy of our calculations, and the arguments of Craievich *et al.* [87] can be applied in our case, too. Namely, those authors have shown that some energy extrema on energy profiles along the constant-volume transformation paths are dictated by the symmetry).

Most of the structures along a transformation path between two higher-symmetry structures, here between B2 and L1<sub>0</sub> at the Bain’s path, have a symmetry that is lower than cubic. At those points of the transformation path where the symmetry of the structure is higher, the derivative of the total energy with respect to the parameter describing the path must be zero. These are the so-called symmetry-dictated extrema. However, other extrema may occur that are not dictated by the symmetry and reflect properties of the specific material. For more details on different types of extrema we refer the reader to Refs. [87–89, 93–97].

The  $\beta_o \rightarrow \gamma$  Bain’s path between ordered phases exhibits no transformation barrier (i.e., it is a barrierless or spontaneous transformation) and a net gain in energy is equal to (see Table 4.1)

$$\Delta E(\beta_o \rightarrow \gamma) = E(\beta_o) - E(\gamma) = 141 \text{ meV/at.}$$

This value is in good agreement with previous studies, for instance, Paidar *et al.* [93] have reported the energy difference along the Bain’s path for the  $\beta_o \rightarrow \gamma$  case of ordered phases equal to about 140 meV/at. while Šob, Wang, and Vitek [89] obtained about 150 meV/at.

Next we investigated the same transformation also for the disordered variants of the

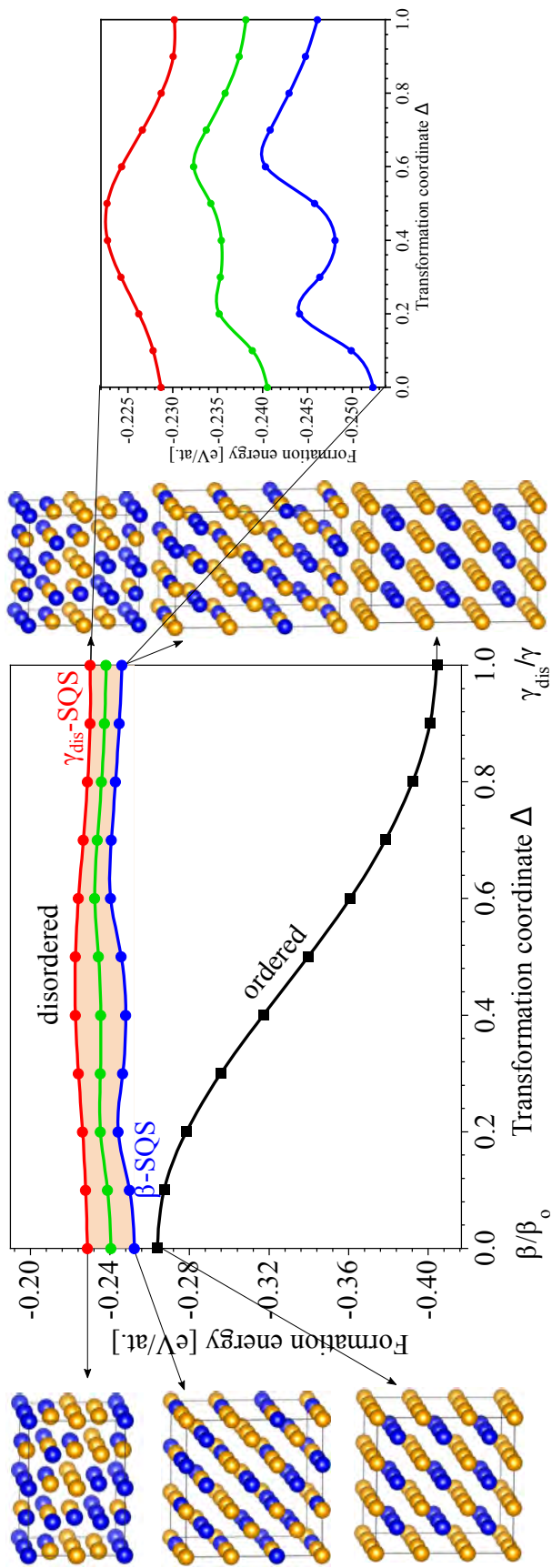


Figure 8.2: The computed changes of the formation energy along the Bain's tetragonal transformation path in the case of ordered phases  $\beta_o \rightarrow \gamma$  as well as disordered ones  $\beta \rightarrow \gamma_{\text{dis}}$ . The inset magnifies the energy changes associated with the transformation of disordered phases with the red and blue curves corresponding to bcc-optimized and fcc-optimized SQSs, respectively (see them visualized along the vertical axes). The green curve in the middle between the red and blue curves represents the average of the energies along the  $\beta \leftrightarrow \gamma_{\text{dis}}$  transformation. The black curve indicates the formation energy changes related to the  $\beta_o \leftrightarrow \gamma$  transformation of the ordered.

ordered  $\beta_o$  and  $\gamma$  phases, i.e.,  $\beta \leftrightarrow \gamma_{\text{dis}}$ . In particular, the blue curve (bottom of the shaded area) in Fig. 8.2 corresponds to a bcc-optimized SQS structure ( $\beta$ -SQS), which is transformed to  $\gamma_{\text{dis}}$ -TiAl (fcc). This means that the short range order parameters were optimized for the bcc lattice (e.g., the first coordination shell containing 8 nearest neighbors) and obviously the Warren-Cowley SRO parameters may no longer be optimal after the transformation to the fcc  $\gamma_{\text{dis}}$ -TiAl phase with 12 nearest neighbors. Taking the fcc structure instead and optimizing its SRO parameters we obtained another supercell (this time with 32 atoms, i.e.,  $2 \times 2 \times 2$  conventional 4-atomic fcc cell). This supercell ( $\gamma_{\text{dis}}$ -SQS) for  $\gamma_{\text{dis}}$ -TiAl is tetragonally transformed into the  $\beta$ -TiAl yielding the data on the red curve.

Therefore, while both blue and red curves are describing the same process, the difference between them may be interpreted as the SQS accuracy limit of our calculations (given also the chosen supercell size). The blue curve starts with  $\beta$  structure at  $-0.252$  and reach the  $\gamma_{\text{dis}}$  phase at  $-0.241$  (refer to Tab. 4.1). Consequently, a simple average (green curve) of these curves is used as a representative for the  $\beta \leftrightarrow \gamma_{\text{dis}}$  transformation path of disordered phases with the color-shaded area being an estimate of the accuracy (Fig. 8.2). The inset clearly shows that small barriers between the two phases occurs for both SQS types, although the actual energy barrier(s) and energy landscapes slightly differ. In summary, our calculations confirm the spontaneous character of the diffusionless transformation  $\beta_o \rightarrow \gamma$  of the ordered phases driven by a mechanical instability (long-wavelength phonons) in the  $\beta_o$ -TiAl phase. This driving force is significantly reduced (the red curve Fig. 8.2), or even completely reversed (the blue curve in Fig. 8.2) in the case of the disordered  $\beta$ -TiAl phase and its hypothetical, chemically disordered counterpart  $\gamma_{\text{dis}}$ -TiAl. Moreover, a (small) energy barrier exists in the disordered case preventing the transformation to proceed spontaneously. Therefore, these results confirm our previous findings that the chemical disorder relatively stabilizes the bcc-based  $\beta$ -TiAl (Chap. 4 and Ref. [109]).

### 8.3 Trigonal transformation in the stoichiometric TiAl

In this section we explore another structural transformation connecting the bcc-like  $\beta_o$  and  $\beta$  on the one hand and the fcc-like states  $\gamma$  and  $\gamma_{\text{dis}}$  on the other hand via the trigonal transformation path described in detail in Section 3.3.1. The corresponding transformation barriers are shown in Fig. 8.3.

The B2 lattice parameter ( $a_{\text{B2}} = 3.187 \text{ \AA}$ ) changes to  $a_{\text{B1}} = 2a_{\text{sc}} = 5.292 \text{ \AA}$  and further to  $a_{\text{L1}_1} = 2a_{\text{fcc}} = 8.132 \text{ \AA}$ . These changes correspond to specific volumes of  $V_{\text{B2}} = 16.19 \text{ \AA}^3/\text{at.}$ ,  $V_{\text{B1}} = 18.52 \text{ \AA}^3/\text{at.}$  and  $V_{\text{L1}_1} = 16.81 \text{ \AA}^3/\text{at.}$ , respectively. For a trigo-

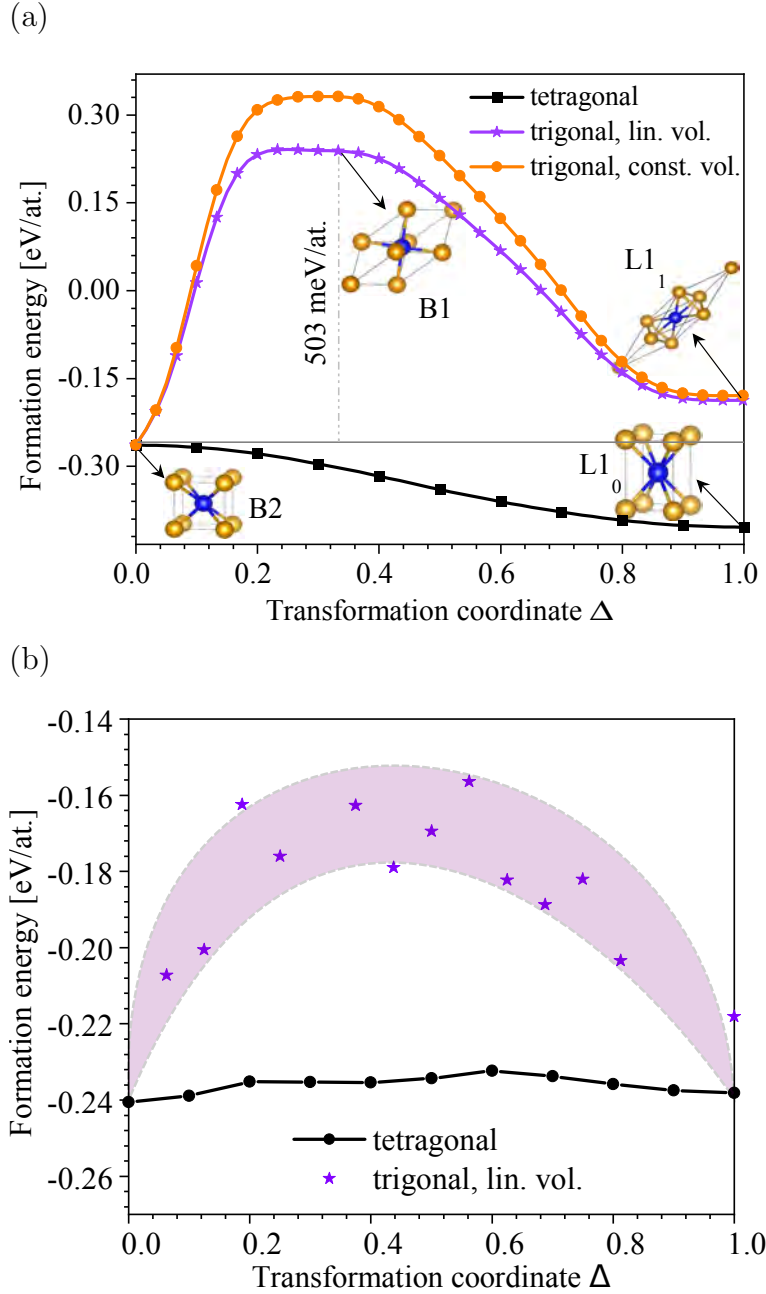


Figure 8.3: The formation energy along the tetragonal (Bain’s) and the trigonal transformation paths for (a) ordered  $\beta_o \rightarrow \gamma/L1_1$  and (b) disordered  $\beta \rightarrow \gamma_{\text{dis}}$  TiAl.

nal path with the specific volume interpolated between the high-symmetry structures, a barrier of 503 meV/at. (see purple curve with star symbols) is obtained. This value is smaller than the previously reported values of 520 meV/at. [93] and 540 meV/at. [89]. This stems from the fact, that the past reports assumed constant volume along the transformation path. To test this hypothesis, we calculated the energies along the trigonal path with keeping the volume constant (and fixed to  $V_{B2}$  (see the orange curve in Fig. 8.3a), yielding a barrier of 596 meV/at.). Importantly, the maximum along the

trigonal path is obtained in either case for the B1 structure, while the B2 ( $\beta_o$ ) and L1<sub>1</sub> structures represent local minima.

The final L1<sub>1</sub> structure represents a metastable phase. Its energy is higher than that of the  $\beta_o$  structure by 76 meV/at. and by 217 meV/at. higher than the  $\gamma$ -TiAl (L1<sub>0</sub> structure), the ground state of TiAl. Similar values of 61 meV/at. and 71 meV/at. were reported for  $E(\text{L1}_1 - \text{B2})$  by [89] and [93], respectively, while the same authors obtained of 215 meV/at. and 212 meV/at. for  $E(\text{L1}_1 - \text{L1}_0)$ . The B1 structure represents a local maximum/saddle point and the energy can be further decreased towards the L1<sub>1</sub> structure for increasing the trigonal distortion. Although this state is (at least thermodynamically) stable, it has not been experimentally reported for the TiAl system with the ground state being the  $\gamma$ -TiAl phase and hence will not be further discussed. Moreover, the barriers are significant and the trigonal transformation is energetically less convenient than the spontaneously proceeding tetragonal path. Consequently, the trigonal transformation path cannot connect the ordered  $\beta_o$ -TiAl and  $\gamma$ -TiAl phases (has the L1<sub>0</sub> lattice), although it offers a possible structural transformation path connecting bcc and fcc disordered states investigated below.

The situation is rather different in the case of disordered states due to the lack of a higher symmetry (Fig. 8.3b). The intermediate state corresponding to a simple cubic structure turned out very difficult to structurally optimize, and therefore we focused on linearly interpolating specific volumes between the values corresponding to the bcc  $\beta$ -TiAl ( $a_{\text{bcc}} = 3.207 \text{ \AA}$ ,  $V_{\text{bcc}} = 16.49 \text{ \AA}^3/\text{at.}$ ) and fcc  $\gamma_{\text{dis}}$ -TiAl ( $a_{\text{fcc}} = 4.05 \text{ \AA}$ ,  $V_{\text{fcc}} = 16.61 \text{ \AA}^3/\text{at.}$ ) phases. The structural complexity manifest itself by the rather scattered data for different  $\Delta$  along the trigonal path. Therefore, the energies are represented by a shaded region with upper and lower envelope for the reader's convenience (Fig. 8.3b). Although the trigonal barrier is an order of magnitude lower than that for the ordered phases, it is still significantly higher than for the tetragonal Bain's path:  $\approx 60\text{--}90$  meV/at. for the trigonal deformation as compared with  $\approx 10$  meV/at. for the tetragonal Bain's path. Therefore, the trigonal transformation is also in the case of disordered phases rather unlikely to be the actual transformation mechanism as the tetragonal path exhibits significantly smaller (to negligible) barriers. We can thus conclude that the (spontaneous) structural transformation between both ordered  $\beta_o \rightarrow \gamma$  and disordered states  $\beta \rightarrow \gamma_{\text{dis}}$  is more likely to proceed via the tetragonal Bain's path instead of the trigonal transformation.

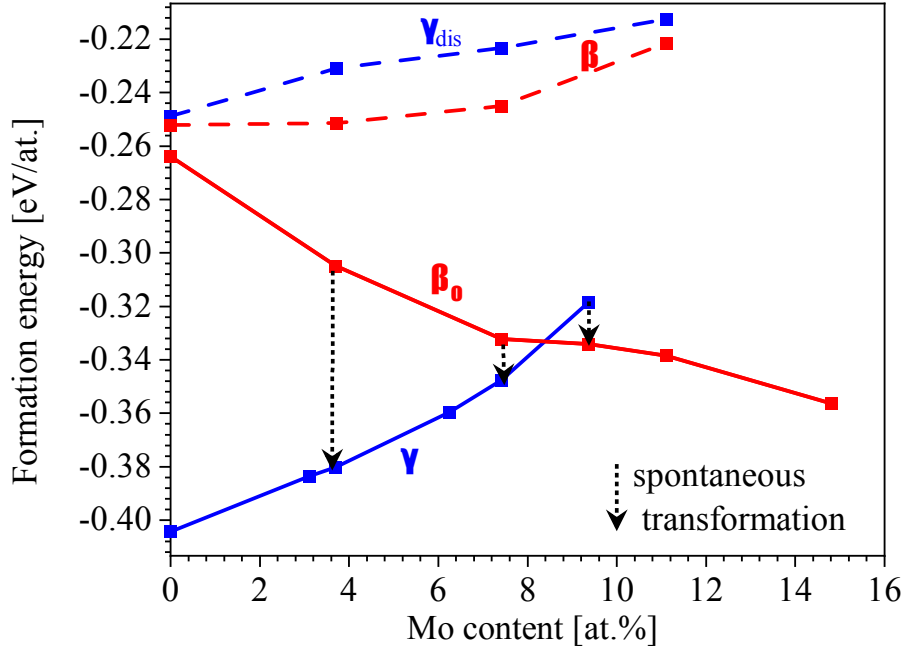


Figure 8.4: The calculated formation energy of the ordered  $\beta_o$  and  $\gamma$  as well as the disordered  $\beta$  and  $\gamma_{\text{dis}}$ -TiAl as a function of the Mo content. The dashed black arrows show spontaneous transformation as obtained during the structural relaxation at 0 K.

## 8.4 Impact of Mo on the $\beta_o \leftrightarrow \gamma$ and $\beta \leftrightarrow \gamma_{\text{dis}}$ transformations in TiAl

As has been mentioned in the Sec. 1.3, the pure  $\beta_o$ -TiAl phase does not exist – it exhibits mechanical and dynamical instability leading to a spontaneous barrierless transformation of the  $\beta_o$  phase into the stable  $\gamma$ -TiAl [109]. Since Mo can be added to TiAl in order to stabilize the  $\beta_o/\beta$  phases [122], we next study the impact of Mo on the transformation energy landscape of both ordered  $\beta_o \leftrightarrow \gamma$  and disordered  $\beta \leftrightarrow \gamma_{\text{dis}}$  states.

The computed energies of formation are shown in Fig. 8.4. Focusing now on the ordered phases, for a low Mo content, the  $\gamma$  phase is more stable than the  $\beta_o$  variant (corresponding to the driving force for the spontaneous transformation at  $x_{\text{Mo}} = 0$ ), but with increasing Mo content the energy difference between these two phases decreases and finally at  $\approx 8$  at.% Mo the  $\beta_o$ -TiAl+Mo phase becomes more stable than the  $\gamma$ -TiAl+Mo variant. The intersection point of the energy of  $\beta_o$  and  $\gamma$  phases denotes the ranges of stability of the single phases, which can co-exist with identical composition exactly at Mo content corresponding to this cross-over.

In contrast to the ordered phases discussed above, the disordered phases exhibit a preference for the bcc structure over the fcc one for all considered Mo compositions (Fig. 8.4). Although the  $\beta$  phase is slightly preferred over the  $\gamma_{\text{dis}}$  phase, the reader should recall



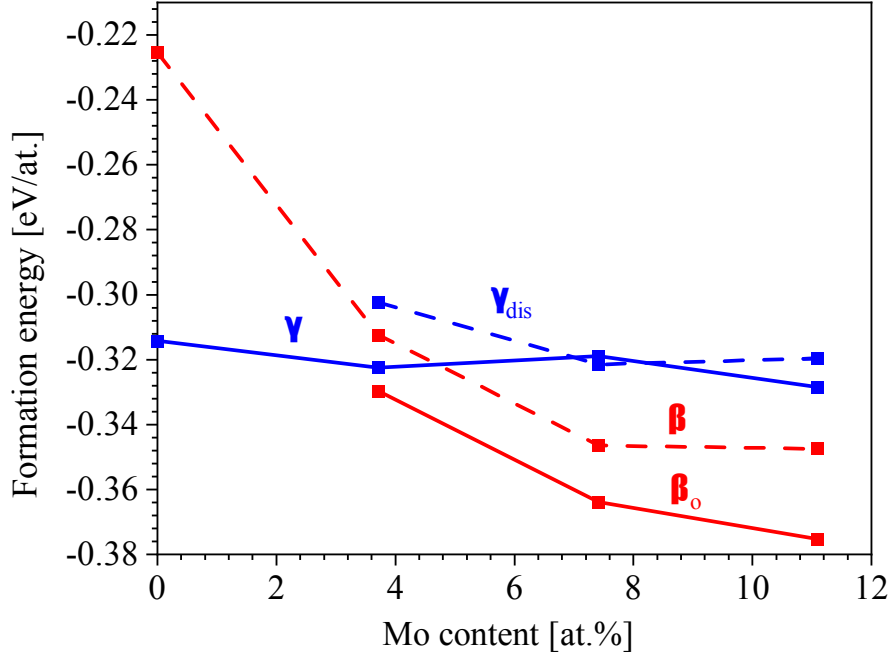


Figure 8.5: Formation energies of  $\beta_o/\beta$  and  $\gamma/\gamma_{\text{dis}}$  phases as a function of Mo content ( $\text{Ti}_{0.5}\text{Al}_{0.5-x}\text{Mo}_x$ ) at 1000 K calculated with the Debye model.

the energy differences presented in Fig. 8.2 for different cells (different sizes, different relaxations). The energy difference between  $\beta$  and  $\gamma_{\text{dis}}$  remains similar to that between different SQSs and supercell sizes (Fig. 8.2). In fact, local structural motifs resembling a hexagonal structure can be detected after the full relaxation which could indicate a relaxation-induced transformation towards a hexagonal  $\alpha$ -based phase. A martensitic transformation of the  $\beta$ -TiAl to a hexagonal phase has been recently experimentally reported [16, 22] and hence such relaxation may possibly be related to this diffusionless transformation as will be discussed in Chap. 9.

Employing the Debye model, we calculated vibrational contribution to the free energy of all four intermetallic phases, as well as of elemental Al, Ti and Mo metals, and used these values to calculate formation energy at finite temperature. The total energy of the binary/ternary systems (the first term on the right hand side of Eq. 4.1) was further corrected for the configurational entropy on the Al sublattice (ordered systems) or in the whole simulation cell (disordered systems). Figure 8.5 shows the resulting  $E_f$  as functions of Mo content corresponding to 1000 K. The most important effect of the temperature is the stabilization of the  $\beta_o/\beta$  phases with respect to the  $\gamma$  phase. We note that the pure  $\beta_o$ -TiAl phase is mechanically unstable, and hence the Debye model (requiring knowledge of elastic constants) is not applicable. It is also worth mentioning that  $\gamma/\gamma_{\text{dis}}$  and  $\beta_o/\beta$  phases become energetically very close. This indicates that the systems are approaching the order/disorder transition at temperatures somewhat higher than 1000 K

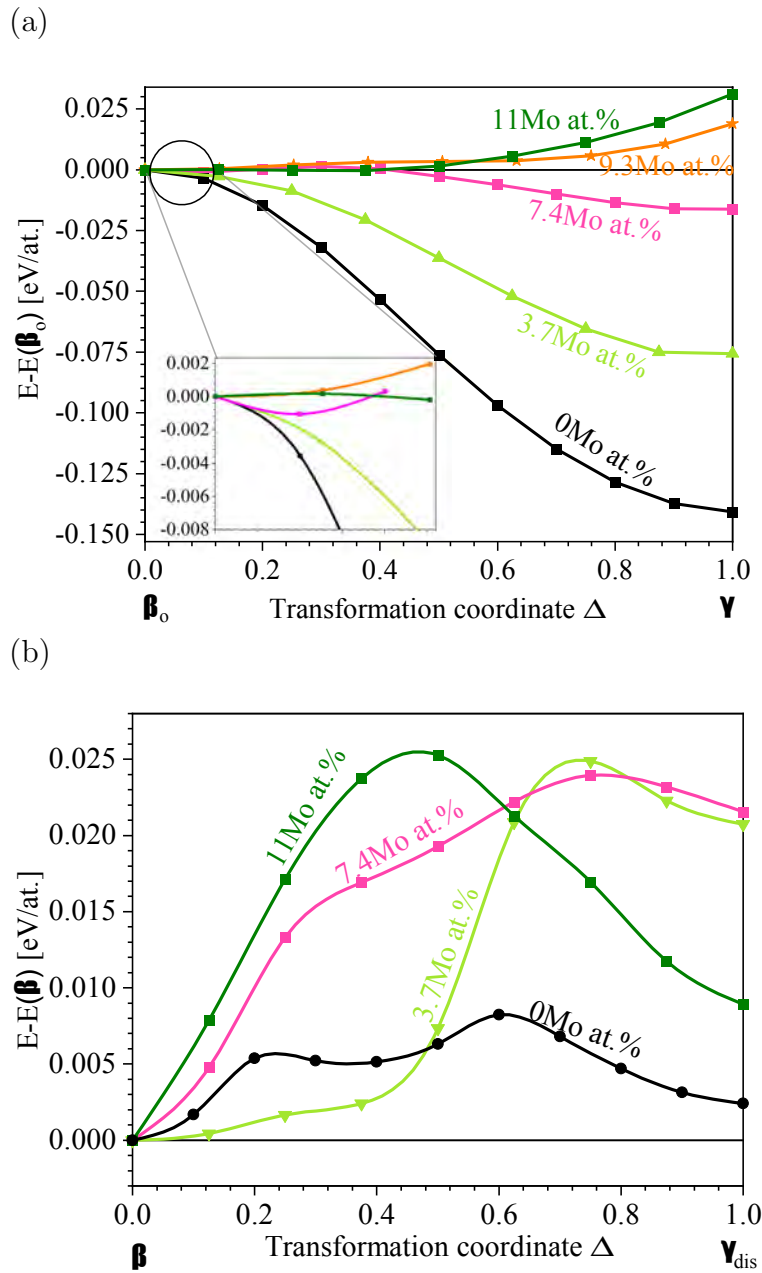


Figure 8.6: The computed energy profile along the tetragonal (Bain's) path for ordered  $\text{Ti}_{0.5}\text{Al}_{0.5-x}\text{Mo}_x$  phase connecting (a) the ordered  $\text{B2-}\beta_o\text{-TiAl+Mo}$  ( $\Delta = 0$ ) and  $\text{L1}_0\text{-}\gamma\text{-TiAl+Mo}$  ( $\Delta = 1$ ) structures and (b) disordered  $\text{bcc-}\beta\text{-TiAl+Mo}$  ( $\Delta = 0$ ) and  $\text{fcc-}\gamma_{\text{dis}}\text{-TiAl+Mo}$  ( $\Delta = 1$ ) structures. The energies are shown relative to the energy of the  $\beta_o/\beta$  phase with a respective Mo content.

(cf. Chapter 7). The Debye model as used here is quite a crude approximation (it considers elastically isotropic material, further no explicit treatment of phonons, no anharmonicity, etc. is included), and thus the present results should be regarded only as demonstrating temperature-related trends rather than accurately predicting ordering temperatures.

Figure 8.6a shows the transformation energy landscape along the tetragonal path as a function of the Mo content for the ordered phases. While the  $\gamma$  structure is clearly preferred for the considered Mo content of 0 and 3.7 at.% with no energy barrier between the  $\beta_o$  and the  $\gamma$  phase, the situation is completely opposite for the 9.3 at.% Mo when the  $\beta_o$ -phase is energetically preferred over the  $\gamma$  phase without any transformation barrier. An interesting case occurs for 7.4 at.% Mo when the  $\gamma$  phase exhibits more negative  $E_f$  than the  $\beta_o$  phase (by  $\approx 18$  meV/at.) but, importantly, the Bain's path shows a small energy barrier (of about  $\approx 1$  meV/at.). Despite its very small height, the barrier opens the possibility of stabilizing both phases, i.e. the  $\beta_o$  phase would become metastable in this particular case.

Figure 8.6b shows energy changes along the  $\beta \rightarrow \gamma_{\text{dis}}$  Bain's transformation path of several studied  $\text{Ti}_{0.5}\text{Al}_{0.5-x}\text{Mo}_x$  compositions. Unlike in the case of the ordered phases (Fig. 8.6a), the disordered phases do not exhibit any clear trend as a function of Mo content. In agreement with formation energies (Fig. 8.4), the  $\gamma_{\text{dis}}$  phases have higher energy than the  $\beta$  phases. Also, in contrary to the ordered phases,  $\beta \rightarrow \gamma_{\text{dis}}$  always exhibit barriers (although in many cases very small) separating the  $\beta$  and  $\gamma_{\text{dis}}$  phases. Consequently, the chemical disorder effectively prevents any spontaneous phase transformations as predicted for the case of ordered  $\beta_o$  and  $\gamma$  phases.

## 8.5 Structural peculiarities of the TiAl(+Mo) system

Our results summarized in the previous section clearly show that the TiAl(+Mo) system exhibits a number of rather unusual properties. For example, when inspecting the energetics of both ordered and disordered TiAl phases transformed along the Bain's path (see Fig. 8.2), it is striking how small energy changes are induced by this structural transformation in the disordered  $\beta \rightarrow \gamma_{\text{dis}}$  case.

An inset at the right-hand side of Fig. 8.2 visualizes energy barriers of a few meV/atom that could be easily overcome. Consequently, the disordered  $\beta$ -TiAl is expected to be quite deformable even in an elastic manner. Despite the disordered  $\beta$ -TiAl is experimentally not observed, the above mentioned deformability can be expected for other phases and/or compositions. For example, the composition of the ordered  $\beta_o$ -TiAl stabilized by 9.3 at.% Mo is close to those found in experimental samples and the energy barriers along

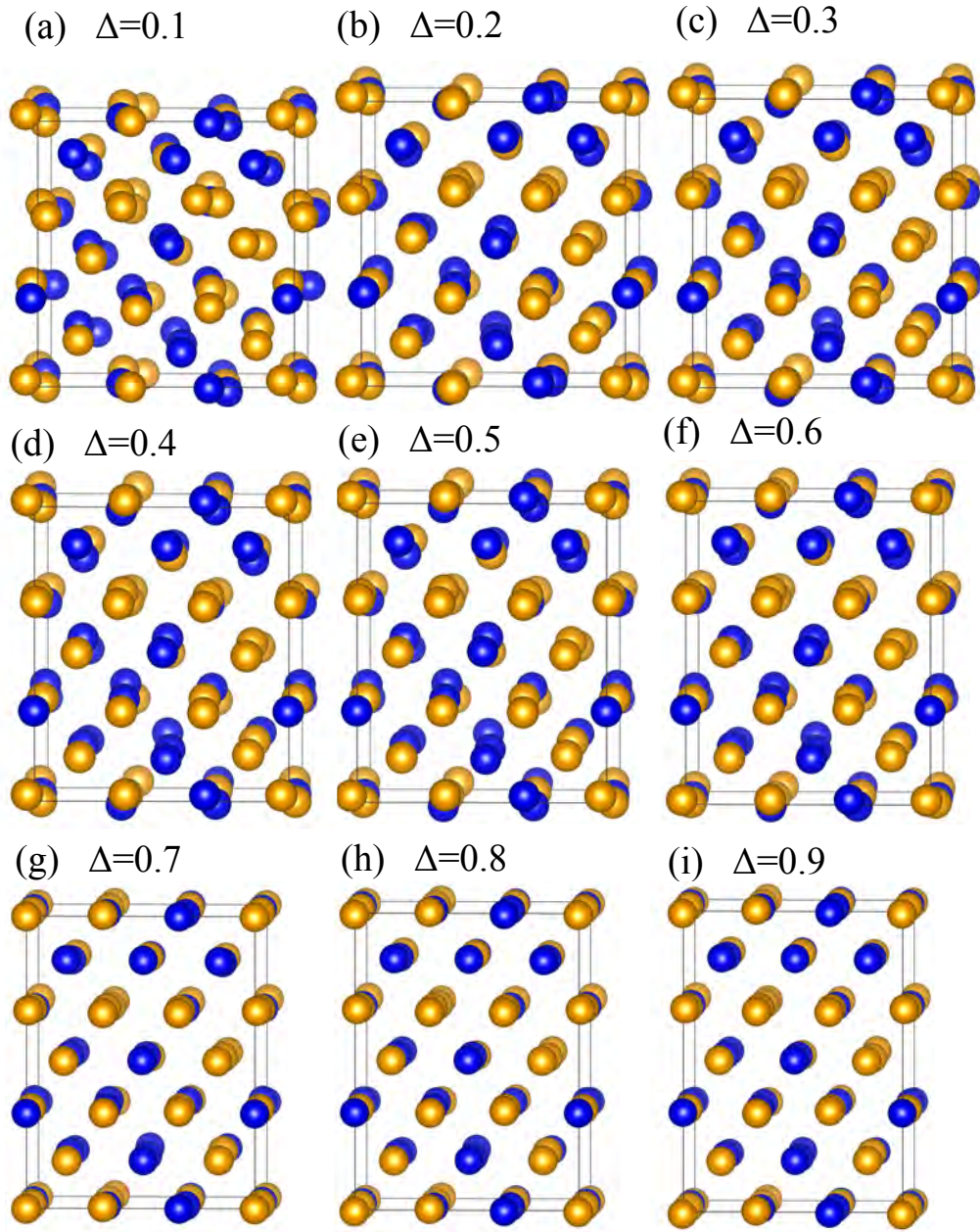


Figure 8.7: Visualization of relaxed internal atomic positions in 54-atom SQS supercell as obtained from minimization of the total energy with respect to the atomic coordinates for selected states along the Bain's path.

a major part of the Bain's tetragonal path are also only a few meV/atom (see Fig. 8.6a). Therefore, it is worthwhile to analyze structural behavior of different phases at an atomic scale along the studied tetragonal path in detail.

Starting with the above mentioned disordered  $\beta$ -TiAl phase and the very small energy changes induced in it by the tetragonal transformation, there are a few facts that should be mentioned.

First, the volume-conserving Bain's transformation is characterized by only very small changes in the first nearest neighbour distances. Therefore, the 1NN bonds are re-oriented in space rather than significantly shortened. The reorientation process is energetically less costly presumably due to the dominant metallic nature of the bonds.

Second, both Ti and Al were reported to exhibit rather small energy differences between the bcc and fcc structures along the Bain's path (about 100 meV/at. and 40 meV/at. for Ti and Al, respectively, see, e.g. Craievich *et al.* [123]). These energy differences are smaller than  $E(\beta_o - \gamma) = 1401$  meV/at. for TiAl. Moreover, none of these two elements is stable in the bcc structure in their ground state and they both spontaneously transform from the bcc structure (symmetry-dictated energy maximum) to the fcc structure (symmetry-dictated energy minimum) in a barrierless manner.

As much as these two reasons may intuitively justify the  $\beta_o \rightarrow \gamma$  behavior, they cannot completely explain the computed results along the whole tetragonal path as the same arguments hold equally well for the disordered  $\beta$ -TiAl, which has the same composition and its energy changes along the tetragonal Bain's transformation path are an order of magnitude smaller (about 10 meV/at.).

The major difference between the disordered  $\beta$ -TiAl and its ordered counterpart is related to its internal atomic configuration and it is not only the fact that  $\beta$ -TiAl has the atoms distributed in a disordered manner. As already discussed above (and shown in Fig. 8.1a), the  $\beta$ -TiAl is internally significantly distorted and the atoms exhibit a tendency to locally resemble the structure of  $\gamma$ -TiAl. We have found that the same significant internal distortions exist in structures encountered along a major part of the Bain's path (Fig. 8.7), in particular for structures from  $\Delta = 0$  up to  $\Delta = 0.6$ . We note that similar behaviour is obtained also for the low-Mo containing TiAl+Mo systems.

In order to analyze distortions of the internal atomic structures quantitatively, we have studied radial distribution functions in the structures encountered along the tetragonal transformation path (Fig. 8.8). Using a comparison with the ordered  $\beta_o$ -TiAl, the differences in the atomic distributions are clearly visible. In particular, the second coordination (2NN) sphere with 6 atoms in the ordered  $\beta_o$ -TiAl (at  $\Delta=0$ ) splits upon transformation, and 4 of its atoms continuously move along the path towards the first coordination (1NN)

shell in the  $\gamma$  phase ( $\Delta = 1$ ), thereby increasing the number in the first coordination cell to 12 (not considering the small tetragonality of the  $\gamma$ -TiAl), see Fig. 8.8a. The other two atoms move further away to join some of the atoms from the third nearest neighbor (3NN) shell (at  $\Delta=0$ ) to form the 2NN shell in the  $\gamma$  phase ( $\Delta = 1$ ). In contrast to these well defined coordination shells in the case of the ordered  $\beta_o$ -TiAl, there is hardly any 2NN shell visible in the radial distribution functions of the disordered  $\beta$ -TiAl (Fig. 8.8b and the magnification in Fig. 8.8c). The peak corresponding to the 1NN shell is significantly broadened covering the distances from 2.8 Å to 3.2 Å. It effectively means that the environment indeed resembles that in the  $\gamma$  phase already for  $\Delta = 0$ .

Therefore, it should be emphasized that the small energy changes in the disordered TiAl along the Bain's path are not those associated with a process when a crystal structure changes from one with strictly 8 atoms in the first nearest neighbor (1NN) shell to another with 12 atoms in the 1NN shell. It is rather so that the Ti and Al atoms locally rearrange (whenever possible) so as to have an fcc-like environment even in configurations that have the shape of the simulation box corresponding to small  $\Delta$  values.

In order to further analyze the importance of the above mentioned internal distortions we have also computed a situation when the  $\beta$ -TiAl phase is chemically disordered but the atoms are located in perfect and undistorted lattice positions, e.g., bcc-like for  $\Delta = 0$ . Computationally it means that the atomic positions were not relaxed, i.e. the total energy was not minimized with respect to the atomic positions. It turns out that the mechanical and thermodynamic stability of such internally undistorted structures is very (even qualitatively) different from the internally distorted (relaxed) ones (Fig. 8.9). The energy of unrelaxed structures is significantly higher than that of their relaxed (internally distorted) counterparts (these energies are same as in Fig. 8.2). In particular, the energies of the unrelaxed structures with  $\Delta = 0$  are clearly higher than those with  $\Delta = 1$ . The energy dependence of configurations close to the  $\Delta = 0$  is very flat and there is no energy barrier along the transformation path. Consequently, the undistorted structures with  $\Delta = 0$  have quite a different mechanical stability: it is much reduced (when compared with the internally distorted configuration with  $\Delta = 0$ ), it is in fact on the verge of instability as there is hardly any barrier for a transformation to the (internally undistorted)  $\gamma$  structure with  $\Delta = 1$ .

When discussing unusual properties of the TiAl+Mo system, it is worth to mention the impact of Mo atoms on the structures that are tetragonally transformed. Regarding the internal atomic configuration of TiAl+Mo phases, the presence of Mo atoms in both ordered and disordered TiAl leads to distortions that are very similar to those in disordered binary TiAl. Employing the analysis of the RDFs along the tetragonal Bain's path again, our results are summarized for 7.4 at.% of Mo in Fig. 8.10. Starting with the

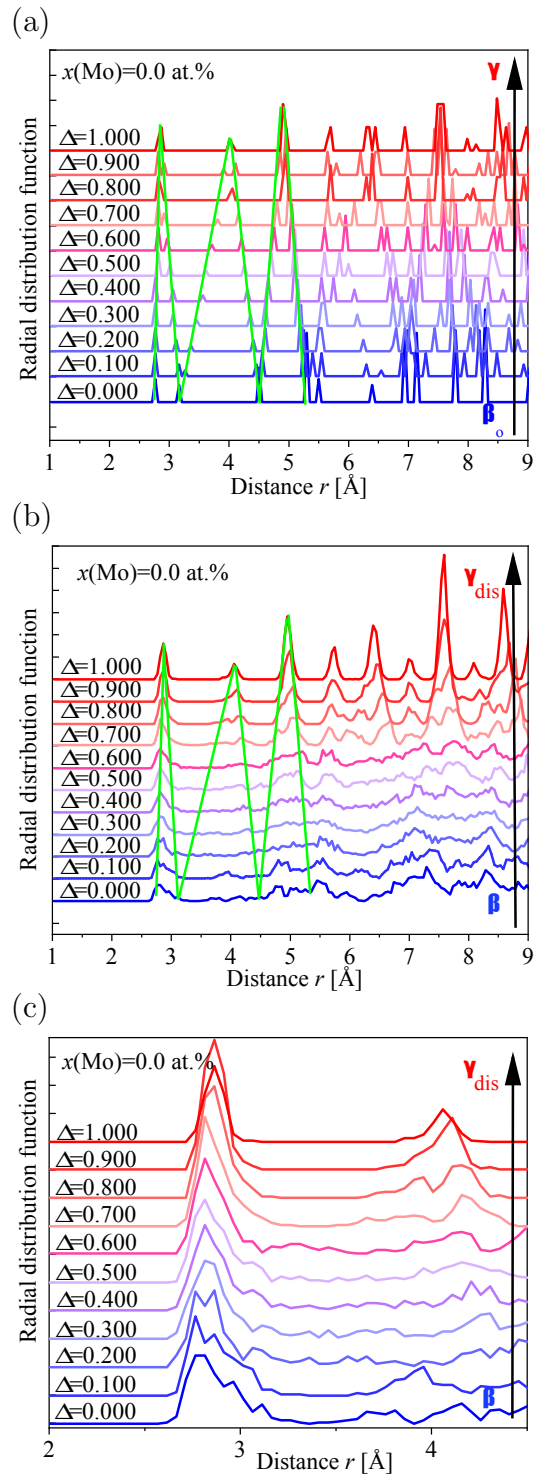


Figure 8.8: Radial distribution functions for (a) the ordered  $\beta_0$ -TiAl and (b) the disordered  $\beta$ -TiAl phases, tetragonally transformed to the  $\gamma/\gamma_{\text{dis}}$  phases. Part (c) is a magnified part of (b). The straight lines schematically indicate shifts in selected nearest neighbor shells of atoms.

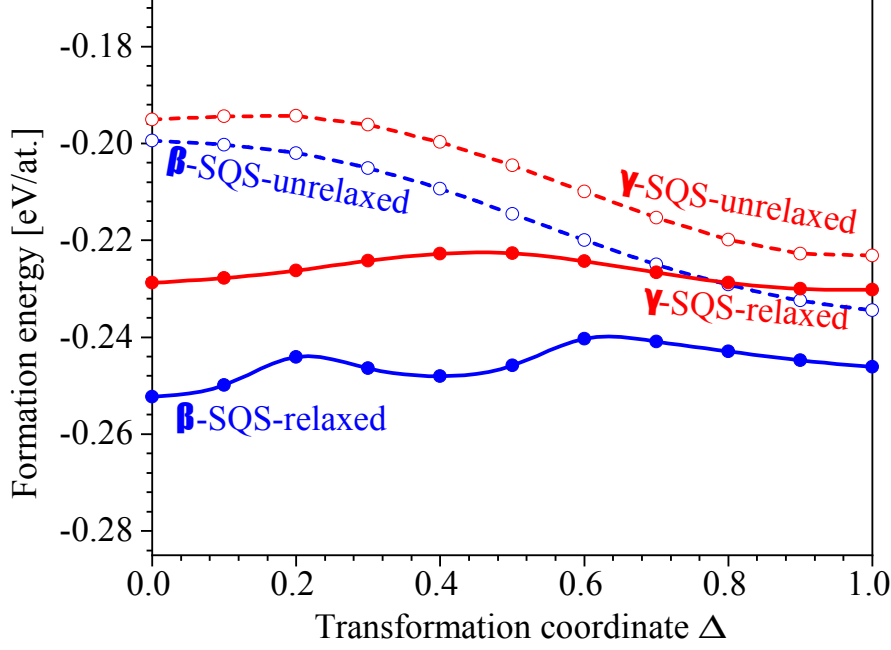


Figure 8.9: Comparison of energies along the  $\beta \rightarrow \gamma_{\text{dis}}$  Bain's transformation path of disordered TiAl for  $\beta$ -optimized (blue) and  $\gamma$ -optimized (red) SQSs with relaxed (full lines) and unrelaxed (dashed lines) internal positions.

ordered TiAl+Mo, the 1NN and 2NN shells merge for  $\Delta = 0$  into a single broad peak (cf. Fig. 8.8a). We interpret this as a tendency to merge the atoms from the 2NN with those in the 1NN in order to form locally an environment that mimics the  $\gamma$  phase. This can be a crucial fact as the Mo atoms stabilize the ordered TiAl phase making it eventually stable even in the  $\beta$  structure.

As far as the disordered TiAl structures with Mo additions are concerned, we exemplify the trends in the case with 7.4 at.% Mo (see Fig. 8.10b, c). The 2NN shell is so broadened and partly merged with both the 1NN shell and other shells that it is very difficult to resolve them (see the magnification in Fig. 8.8c). This behavior resembles that in the disordered binary TiAl visualized in Fig. 8.8b, c. Here it is worth mentioning that the chemical disorder and Mo additions are two mechanisms stabilizing the  $\beta_o/\beta$  phases of TiAl+Mo. It is interesting that their combination, i.e. Mo additions into the disordered  $\beta$ -TiAl does not enhance the stabilization effect. On the contrary, the impact of Mo atoms on the thermodynamic stability of disordered  $\beta$ -TiAl+Mo is negative, i.e. Mo atoms energetically destabilize the disordered TiAl+Mo phase, as visible in the trends of the formation energy in Fig. 8.4. This trend is reverted with temperature (including configurational and vibrational entropy), see Fig. 8.5. We therefore conclude that the stabilizing effect of Mo is related to (i) replacing Ti-Al bonds with Ti-Mo (ordered  $\beta_o$ -TiAl+Mo) and (ii) significant contribution to vibrational entropy at high temperatures.



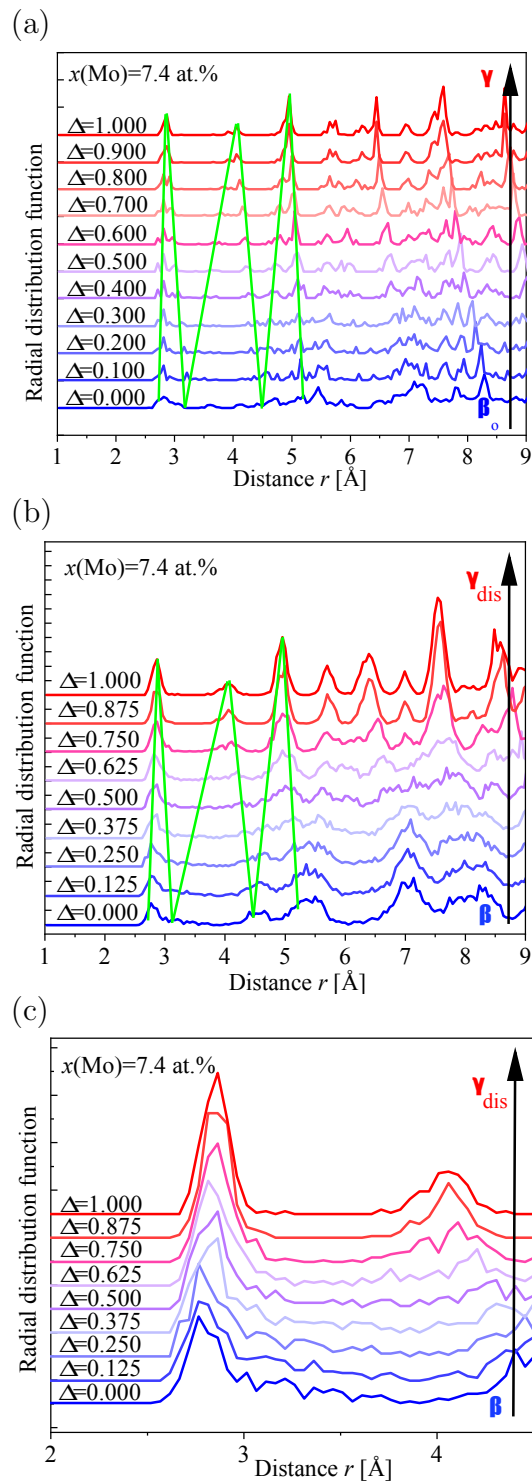


Figure 8.10: Radial distribution functions for (a) the ordered  $\beta_0$  and (b) disordered  $\beta$  TiAl+Mo phases with 7.4 at.% Mo additions. (c) is a magnified part of the RDFs from the (b). The straight green lines schematically indicate shifts in selected nearest neighbor shells of atoms.

Table 8.1: The short-range order parameters of the 54-atom ( $\beta$ -SQS) and 32-atom ( $\gamma_{\text{dis}}$ -SQS) supercells used in our calculations. The parameter  $\Delta$  is the transformation coordinate with  $\Delta = 0$  corresponding to the bcc structure and  $\Delta = 1$  to the fcc structure.  $\alpha_i$  is the Warren-Cowley short range order parameter for the  $i^{\text{th}}$  coordination shell and  $\alpha$  is their weighted sum used as an objective function during the SQS generation [63].

	$\Delta$	$\alpha$	$\alpha_1$	$\alpha_2$	$\alpha_3$	$\alpha_4$	$\alpha_5$	$\alpha_6$	$\alpha_7$
$\beta$ -SQS	0	0.0088	-0.0000	-0.0062	0.0000	-0.0185	0.0000	-0.0021	0.0053
	1	0.0228	-0.0123	0.0062	-0.0123	0.0000	-0.0074	-0.0062	0.0053
$\gamma_{\text{dis}}$ -SQS	0	0.0200	0.0000	0.0000	0.0000	0.0000	-0.1000		
	1	0.0208	0.0000	0.0000	0.0000	-0.0833	0.0000		

### 8.5.1 Supercell size vs. SQS

We now focus a bit closer on the SQS supercells and the fact that the energy values shown in Fig. 8.2 for two different SQS supercells exhibit a difference of about 20 meV/at. We assign this apparent discrepancy to differences in the supercell shapes and/or sizes leading to differently optimized short range order parameters during their generation. In particular, the  $\beta$ -SQS is a  $3 \times 3 \times 3$  supercell based on a 2-atom bcc conventional cubic cell, thus containing 54 atoms. Consequently, the 8<sup>th</sup> coordination shell is the first one containing periodic images of atoms (located in the neighboring periodically repeated supercells), making only the first 7 coordination shells available for an independent optimization of the atomic disorder. On the contrary, the  $\gamma_{\text{dis}}$ -SQS is a  $2 \times 2 \times 2$  supercell based on the conventional 4-atom fcc cell containing 32 atoms. Here, already the 6<sup>th</sup> coordination shell contains periodic images of atoms. Therefore, in this case, only atoms in the first five coordination shells can be independently optimized. The short-range order of atoms in a binary alloy can be conveniently described by Warren-Cowley short range order (SRO) parameters defined as

$$\alpha_i = 1 - \frac{N_{\text{AB}}}{NM_i x_A x_B}, \quad (8.1)$$

where  $N_{\text{AB}}$  is the number of A–B pairs at the  $i^{\text{th}}$  coordination shell in a supercell with  $N$  sites,  $M_i$  is the coordination of each site on the  $i^{\text{th}}$  shell, and  $x_A$  and  $x_B = 1 - x_A$  are compositions of atoms A and B, respectively.

It turns out that our two structural models with 54 and 32 atoms have the Warren-Cowley short range order parameters responding to the simulated tetragonal transformation very different (see Tab. 8.1). In particular, while the 54-atom cell has zero  $\alpha_1$  and  $\alpha_3$  parameters corresponding to the first and third shells in the bcc structure, respectively, the absolute values of the first three SRO parameters  $\alpha_1$ ,  $\alpha_2$  and  $\alpha_3$  are significantly non-zero for the Bain-transformed  $\beta$ -SQS to the fcc structure (the overall  $\alpha = 0.0228$  for  $\Delta = 1$ ). Here we note that the objective function combines individual SRO parameters

$\alpha_i$  (specifically, their absolute values) with arbitrary weights, here with factors  $1/i$ . These decreasing weights  $1/i$  represent an intuitive expectation that the nearest interactions are the most important. However, they do not reflect any specific chemistry of the studied system. The identified complexity related to the SQS description of strong long-range interactions present in the Ti-Al intermetallic system, in particular for the small cells, is in agreement with a previous study on the supercell-size effect on accuracy of elastic constants in the Ti-Al systems [124]. It was shown that the 32-atomic supercell is to be expected to have an error of around 1%, while increasing the size to 108 atoms, the error drops to approximately half of that [124].

## 8.6 Spontaneous transformation as a function of the Mo content

Let us discuss in detail our results obtained for the formation energies given in Fig. 8.4. In particular, it should be noted that the points in Fig. 8.4 represent the calculated energies based on different supercells with different sizes with the Mo atoms distributed according to the SQS concept. The  $\beta_o$ -based SQS supercells contain 54 atoms while the  $\gamma$ -based SQS supercells contain 32 atoms. As a consequence of different sizes the Mo concentrations in the 32-atom and 54-atom supercells are slightly different (one Mo atom corresponds to 1.85 at.% in the  $\beta_o$ -based supercells and 3.12 at.% in the  $\gamma$ -based supercell). Thus, for example, while the datapoint at  $x_{\text{Mo}} = 3.12$  at.% on the  $\gamma$  dataset in Fig. 8.4 corresponds to one Mo atom in the  $\gamma$ -based supercell, the data point at  $x_{\text{Mo}} = 3.70$  at.% is a fully structurally relaxed  $\beta_o$  phase with two Mo atoms in the supercell (i.e. spontaneously transformed  $\beta$ -SQS once also cell shape optimization was allowed).

These differences also mean that a special attention must be paid when comparing spontaneous transformations in Fig. 8.4 (see the vertical black dashed arrows) with the tetragonal Bain's transformations in Fig. 8.6a. The comparison is straightforward for, e.g., a spontaneous transformation of  $\beta_o \rightarrow \gamma$  shown in Fig. 8.4 for 3.7 at.% Mo, which is fully in agreement with the transformation energetics depicted in Fig. 8.6a. Similar situation is in the case of 7.4 at.% (4 Mo atoms in the  $\beta_o$  phase supercell), although the energy difference, i.e. the transformation driving force, is much smaller. Importantly, no  $\beta_o \rightarrow \gamma$  transformation occurs for 11.1 at.% (6 Mo atoms in the  $\beta_o$  supercell). On the contrary, the  $\beta_o$ -TiAl+Mo datapoint with  $x_{\text{Mo}} = 9.4$  at.% is actually a spontaneously transformed  $\gamma$  phase (with 3 Mo atoms in the  $\gamma$  supercell). In summary, since the structural relaxations (at 0 K) are sufficient to induce phase transformations, the Born-Oppenheimer energy landscape for the tetragonal  $\beta_o \leftrightarrow \gamma$  structural connection is likely to contain negligible-to-no energy barriers, in agreement with results from the previous section (Fig. 8.6a).

Therefore, the  $\gamma$  and  $\beta_o$  phase can co-exist only when the local Mo content in each of them is different (up to  $\approx 7$  at.% in the  $\gamma$ -TiAl the less Mo, the more stable), otherwise in the case of  $\beta_o$ -TiAl for yet higher Mo content.

### 8.6.1 Experimental evidence

To support the results of our calculations, let us now compare them with available experimental data. During the previous decades, phase equilibria and phase transformations in the ternary Ti–Al–Mo system have been investigated by a number of different research groups and discussed, e.g., in Refs. [17, 18, 120, 125–131], to name a few. Yet, only some experimental studies have explicitly addressed the phase transformations between  $\beta$  (or  $\beta_o$ ) and  $\gamma$  phases in Mo-containing alloys [21, 128, 128, 132, 133]. Singh and Banerjee [128] analyzed solidification structures of various Ti-(44-50)Al-(2-6)Mo (at.%) alloys. A comparison of the measured chemical compositions, which prevail in these microstructures close to thermodynamic equilibrium, reveals large differences in the local Mo content in the  $\beta/\beta_o$  and  $\gamma$  phases. For example, in the Ti-50Al-6Mo (at.%) alloy, the primary  $\beta$  phase (present at room temperature as ordered  $\beta_o$ ) exhibits a Mo content of 13.0 at.%, whereas only 3.2 at.% Mo are present in the interdendritic  $\gamma$  phase. In Ti-50Al-2Mo (at.%), there are 11.1 at.% Mo in  $\beta_o$  and only 1.2 at.% Mo in  $\gamma$ , while peritectic  $\alpha$  (present at room temperature as ordered  $\alpha_2$ ) features in both microstructures as a third phase. These chemical compositions, which were determined by means of electron probe microanalysis, support our conclusion drawn in previous results section, namely that the co-existence of  $\gamma$  and  $\beta_o$  must be connected with differences in the local Mo content. Furthermore they confirm our prediction that the  $\beta_o$  phase is more stable than  $\gamma$  for Mo contents of 8 at.% and higher, while for lower Mo contents a spontaneous transformation to  $\gamma$  takes place.

At this point it is important to note that qualitative arguments of this kind can only be deployed, if experimental conditions close to thermodynamic equilibrium apply, and the experiments were conducted at sufficiently low temperatures. In specimens that were quenched from high temperatures, also Mo contents lower than  $\approx 8$  at.% can be observed in the  $\beta_o$  phase. For example, Singh and Banerjee [128] observed Mo contents as low as 2.2 at.% and 2.9 at.% after quenching a Ti-44Al-2Mo (at.%) alloy from 1673 K and 1573 K, respectively. These microstructures are usually not stable and transform upon heating as they approach thermodynamic equilibrium. In a recent paper, Musi *et al.* [22] compared quenched specimens of a Ti-44Al-3Mo (at.%) alloy with hot-isostatically pressed conditions of the same material and found (by means of electron dispersive spectroscopy in a transmission electron microscope) that the chemical composition of the  $\beta_o$  phase increased from a Mo content of 4.1 at.% to 7.7 at.% during annealing at 1473 K

and slow cooling. In contrast to this, the newly formed  $\gamma$  phase finally exhibited a Mo content of 1.5 at.%, which is again in good qualitative agreement with our predictions.

Recently, the partitioning of Mo between the phases  $\beta_o$  and  $\gamma$  has also been studied experimentally in the course of an *in situ* heating experiment at a synchrotron radiation source [133]. For this experiment, a Ti-44Al-7Mo (at.%) alloy was selected. According to the equilibrium phase diagram [131, 134],  $\beta_o$  and  $\gamma$  are the only stable phases in this alloy below roughly 1473 K. Consequently, no other phases have to be considered during the observation of the  $\beta \rightarrow \beta_o + \gamma$  phase transformation, which occurs when the quenched and, thus, supersaturated single-phase  $\beta_o$  microstructure decomposes upon heating. Starting from the solid solution, in which  $\beta$  exhibits the nominal chemical composition of the alloy,  $\gamma$  particles of a reduced Mo content nucleate and grow. After heating to 953 K at a rate of 10 K/min, the  $\gamma$  precipitates were found to have a Mo content of 3.9 at.%. As only 8 to 10 % of the matrix had transformed to  $\gamma$  at this point, atom probe tomography indicated that the Mo content of the  $\beta_o$  matrix had increased only marginally. Long-term annealing of this material at 1273 K, though, has been shown to finally yield Mo contents of 16.3 at.% in the  $\beta_o$  and 2.0 at.% in the  $\gamma$  phase [21]. This behaviour is again very much in agreement with our calculations. As can be deduced from Fig. 8.4, the overall energy of the system is minimized by the observed phase separation, during which almost pure  $\gamma$  phase and  $\beta_o$  at a significantly higher Mo content are obtained. Furthermore, in accordance with our results, this transformation was found to take place without the formation of any metastable phase of different crystallographic structure.

Based on our calculations, we can even go one step further. The convex shape of the curve related to the  $\beta_o$  phase in Fig. 8.4 may be taken as an argument supporting the suggestions proposed in Ref. [133], namely that in the investigated Mo-range, the  $\beta_o$  phase does not display any tendency towards spinodal decomposition, but that the phase separation is governed rather by a nucleation and growth process. This research question was raised, as the conditions pertaining to classic nucleation, e.g. that the  $\gamma$  nuclei already show their final chemical composition, were found to be not ideally fulfilled due to the complexity of the proposed heat treatments. In this regard, our *ab initio* calculations successfully address a critical issue which is, in this material system, not easily accessible by means of experimental techniques.

# Cubic to hexagonal martensitic transformations

From the discussions in Sec. 1.3.2 and 1.3.3 we expect a diffusionless transition from cubic to hexagonal phase to take place upon rapid cooling. However, before this transition occurs, the cubic phase must become dynamically unstable (as predicted and explained in details in Sec. 4.2.3 and 8.2) with respect to distortions (has described in Sec. 3.3.2) which transform it to hexagonal structure. The transition path studied in the present work involves two degrees of freedom, namely  $\delta_c$  (cell shape) and  $\delta_s$  (shuffling) as introduced in Sec. 3.3.2. Using these transformation coordinates, the cubic phase is  $(\delta_c, \delta_s)=(0.0,0.0)$  and the hexagonal corresponds to  $(1.0,1.0)$ . Hence we performed total energy calculations for a set of distortions with  $\delta_c, \delta_s \in [0.0, 1.0]$ .

## 9.1 Potential energy surface and the energy barriers for binary TiAl system

The potential energy surface (PES) is the ground state electronic energy of the system which is constructed as a function of the atomic configurations. In the next sections, the calculated energies of two martensitic transformations ( $\beta_o \rightarrow \text{B19}$  and  $\beta \rightarrow \alpha'$ ) will be discussed.

### 9.1.1 $\beta_o \rightarrow \text{B19}$ martensitic transformation

The potential energy surface of  $\beta_o \rightarrow \text{B19}$  is displayed in Fig. 9.1. The transformation is started with changing cell shape and shuffling the atomic positions from the B2 structure ( $a = b = c = 3.187 \text{ \AA}$ ) to the B19 structure ( $a = 4.917, b = 2.839$  and  $c = 4.636 \text{ \AA}$ ). The ordered  $\beta_o$  and B19 unit cells are located at the lower-left and upper-right corners of

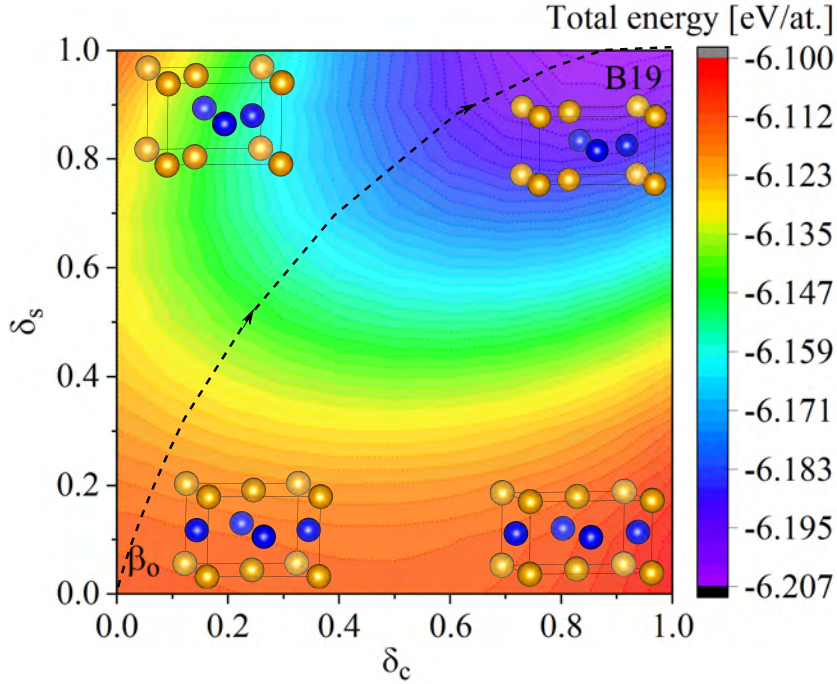


Figure 9.1: A contour plot of a potential energy surface of  $\beta_o \rightarrow \text{B19}$  martensitic transformation in terms of cell shape and cell volume changes,  $\delta_s$  and  $\delta_c$ , respectively. The dashed black curve shows the minimum energy path (MEP) which was drawn by tracing back the steepest descent from the initial ( $\beta_o$ ) to final (B19) structures. Crystal structures of some states belonging to the specific  $\delta_c$  and  $\delta_s$  are shown.

Fig. 9.1, respectively. In contrast, the upper-left and lower-right corner plots corresponds to unit cells transformed along only one of the  $\delta_s$  or  $\delta_c$  axes. As can be seen in the contour plot, the local maximum  $\simeq -6.113$  eV/at. and minimum  $\simeq -6.207$  eV/at. belong to  $\beta_o$  and B19 structure, respectively. However, the B19 phase is energetically favored nearby  $\simeq -6.207$  eV/at.. The dashed black curve shows the minimum energy path which was drawn by tracing back the steepest descent from the initial ( $\beta_o$ ) to the final (B19) structure. The most clearly revealed feature in the  $\beta_o \rightarrow \text{B19}$  transformation is the fact that it is barrierless, and therefore a spontaneous transition is anticipated.

### 9.1.2 $\beta \rightarrow \alpha'$ martensitic transformation

We start the analysis by considering a disordered structure modeled using special quasi-random structures (SQS) method [63, 86], in which the Warren-Cowley short-range order (SRO) parameters were optimized for pair up to 7th coordination shell in the bcc structure. We call this structure a bcc(sq<sub>s</sub>). The PES corresponding to the  $\beta \rightarrow \alpha'$  martensitic transformation obtained with bcc(sq<sub>s</sub>) is plotted in Fig. 9.2a; we called this path bcc(sq<sub>s</sub>). To gain more insight and clarity, we have additionally considered SQS structure with SRO

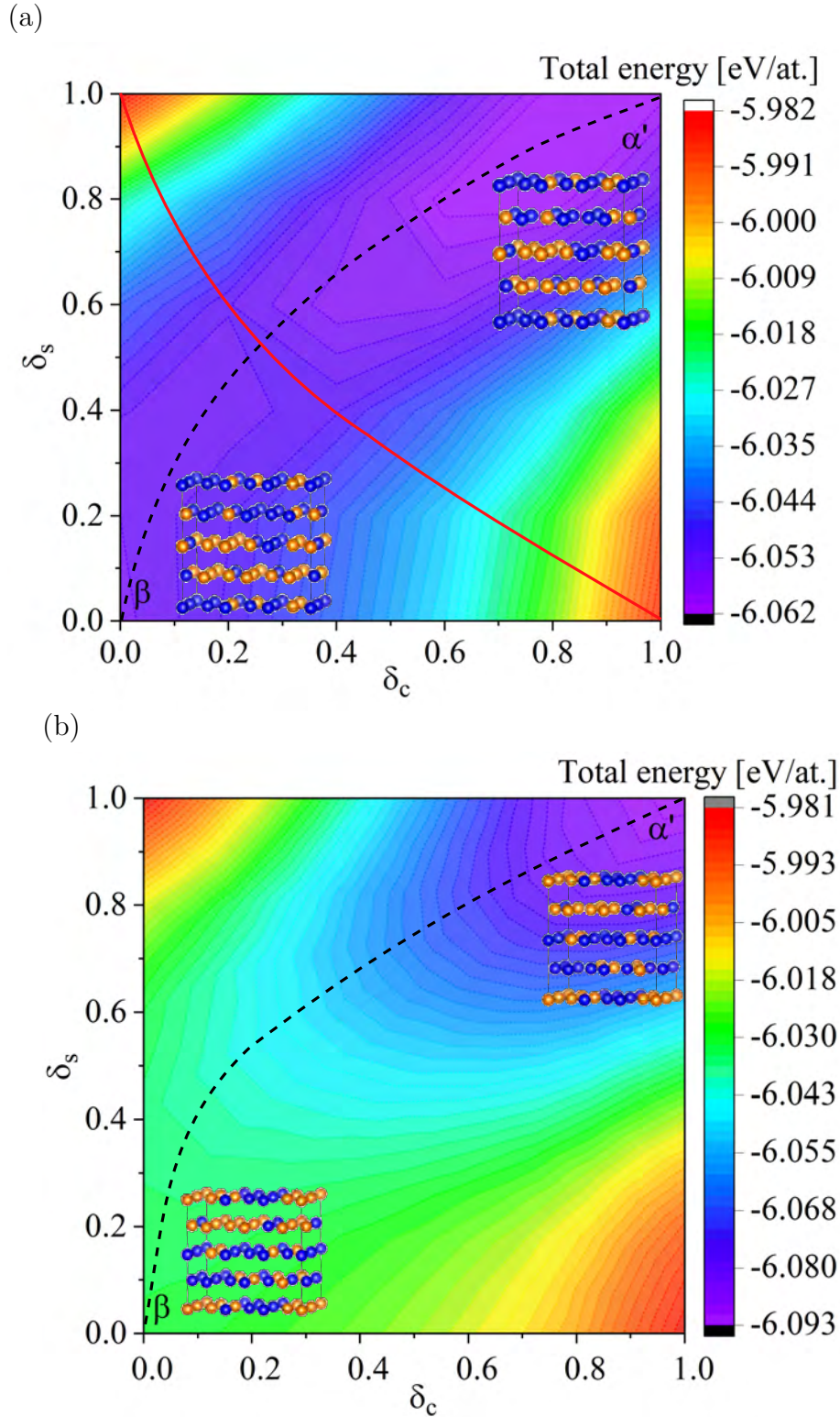


Figure 9.2: A contour plot of a potential energy surface of  $\beta \rightarrow \alpha'$  martensitic bcc to hcp transformation, in which (a) bcc(sqs) and (b) hcp(sqs) are deformed in terms of cell shape change and cell volume changes  $\delta_s$  and  $\delta_c$ , respectively. The dash black curves show the minimum energy path (MEP) which was drawn by tracing back the steepest descent from the initial ( $\beta$ ) to final ( $\alpha'$ ) structures. The solid-red curve demonstrates the position of the energy barrier. Snapshot of  $\beta$  and  $\alpha'$  states are shown.



parameters optimized on the hcp lattice. Thus we have explored a reverse path by starting transformation from hexagonal  $\alpha'$  (sqs-structure) to cubic  $\beta$ -TiAl as a function of  $\delta_c$  and  $\delta_s$ , which is plotted in Fig. 9.2b. This path is called hcp(sqs). In both transformations,  $(\delta_c, \delta_s) = (0.0, 0.0)$  and  $(1.0, 1.0)$  correspond to  $\beta$ -TiAl (lower-left corner) and  $\alpha'$ -TiAl (upper-right corner), respectively.

By comparing both contour plots, unlike the cases of  $\beta_o \rightarrow \text{B19}$  (Fig. 9.1) and hcp(sqs) (Fig. 9.2b) transformations, there is an energy barrier (crossing of dashed-black and solid-red curves)  $\simeq -6.05$  eV/at. along the bcc to hcp transformation using bcc(sqs) (Fig. 9.2a). This means that the transformation in this case is not spontaneous. The Minimum Energy Path (MEP) was analyzed in both systems (see Fig 9.2). The dashed black curves represent the MEP of the ionic relaxation of bcc(sqs) and hcp(sqs) transformations, respectively. It is therefore obvious that the TiAl system is extremely sensitive to the actual disorder state, as demonstrated by the qualitatively different behavior of different SQS cells.

### 9.1.3 Comparison with the CPA method

In order to obtain more trust in the *ab initio* predictions, the total energy along the cubic to hexagonal transformation path was calculated also using an alternative EMTO-CPA method. Unlike the VASP-SQS method, EMTO-CPA does not use any supercell but treats the disorder problem within the single-site approximation. Moreover, for the clarity of the comparison, we will represent the transformation landscapes using only a single transformation coordinate, namely  $\delta_c$ . The shuffling parameter,  $\delta_s$  is set equal to  $\delta_c$  for the EMTO-CPA calculations as well as the initial structures for the VASP-SQS calculations. This corresponds to a transformation along the diagonal  $(0, 0) \rightarrow (1, 1)$  in Figs. 9.1 and 9.2. However, while the PES clearly suggest that the MEPs are not straight connections of the initial and final states, we have additionally relaxed the ionic positions in VASP-SQS while keeping the cell shape fixed. Those calculations are in the following denoted as ‘relaxed’, whereas the energies corresponding to the initial states with  $\delta_s = \delta_c$  are denoted as ‘unrelaxed’. Finally we note that this relaxation can yield lower energies along the transformation path than what would be read out from PES, as the relaxation may be more general than what is described by a simple plane shuffling.

Generally, we compare the EMTO-CPA result with the supercell result without the ionic relaxation, i.e. with energies corresponding to the initial configurations, identical to that considered with the EMTO-CPA method. In Fig. 9.3 we plot the total energies normalized to the  $\beta_o/\beta$  state energy by subtracting the total energy,  $E$ , from the total energy of the initial state,  $E_0$ , which belongs to  $\delta_c = 0.0$  state ( $\beta$  structure). The transparent blue line in Fig 9.3a is the total energy of unrelaxed  $\beta_o \rightarrow \text{B19}$  deformation

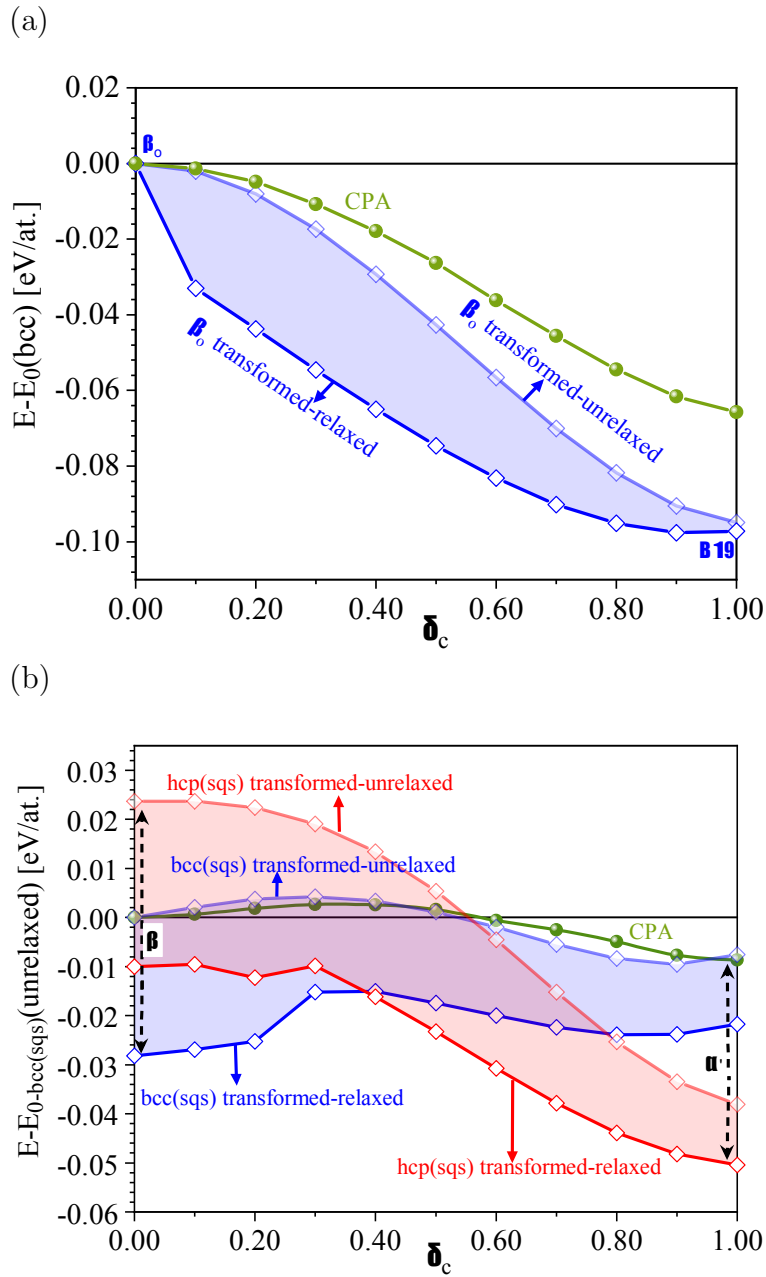


Figure 9.3: The total energy along with the cubic to hexagonal transformation path for (a)  $\beta_0 \rightarrow \text{B19}$  transformation and (b) for  $\beta \rightarrow \alpha'$  path in terms of cell shape changes,  $\delta_c$ . The EMTO-CPA result are represented by green curves. The unrelaxed results are shown with transparent colors. bcc(sq3) denotes structural connection between cubic and hexagonal structures using bcc-optimized SQS, hcp(sq3) is a connection for hcp-optimized SQS supercell.

obtained by VASP and the green line represents the gained total energy by EMTO-CPA method. Both methods agree qualitatively on the energy landscape including a maximum at  $\delta_c = 0.0$  state and a minimum at  $\delta_c = 1.0$  state which belong to  $\beta_o$  and the B19 structures, respectively. VASP predicts somewhat larger energy difference between the two states of  $\Delta E(\text{B19} - \beta_o) = -0.094 \text{ eV/at.}$  than the EMTO-CPA method which yields  $\Delta E(\text{B19} - \beta_o) = -0.065 \text{ eV/at.}$ . Those values are consistent with results in Table 4.1, with the EMTO-CPA value differing slightly, perhaps due to slightly different geometry of the B19 structure. Allowing for ionic relaxations results in a significant energy reduction for small  $\delta_c$  (i.e. in the vicinity of the  $\beta_o$  structure), while for  $\delta_c \rightarrow 1$  only minor energy gain due to ionic relaxations are predicted. This is consistent with the MEP shape shown in Fig. 9.1.

The same comparison for  $\beta$  to  $\alpha'$  is presented in Fig. 9.3b. The unrelaxed energies along the bcc(sqs) path show a good agreement with the EMTO-CPA method. The energy difference  $\Delta E(\alpha' - \beta) = -0.007 \text{ eV/at.}$  predicted by VASP-SQS is almost identical with  $\Delta E(\alpha' - \beta) = -0.008 \text{ eV/at.}$  obtained from EMTO-CPA. Moreover, both methods suggest a small energy barrier of  $E_b = \Delta E(\text{barrier} - \beta) = 0.004 \text{ eV/at.}$  (VASP-SQS) and  $0.002 \text{ eV/at.}$  (EMTO-CPA). Relaxing the SQS supercells yields the energy difference to  $\Delta E(\alpha' - \beta) = 0.006 \text{ eV/at.}$ . Importantly, the phase preference changes ( $\beta$  is more stable than  $\alpha'$ ) and the transformation barrier increases to  $E(\text{barrier} - \beta) = 0.013 \text{ eV/at.}$ .

The hcp(sqs) path was evaluated also with respect to the  $\beta$  bcc(sqs) phase in Fig. 9.3b. Several aspects can be realized. First, the hcp(sqs) path decreases the energy of  $\alpha'$  structure at the  $\delta_c = 1.0$  in both relaxed and unrelaxed cases (with respect to bcc(sqs)), which means the hcp(sqs) is energetically more suitable description than the bcc(sqs). Second, the unrelaxed energy difference in case of hcp(sqs),  $\Delta E(\alpha' - \beta) = -0.061 \text{ eV/at.}$ , is bigger than the energy difference of unrelaxed bcc(sqs). By relaxing the structures along the transformation path, this energy difference decreases (in absolute value) to  $\Delta E(\alpha' - \beta) = -0.04 \text{ eV/at.}$ . Third, no barrier is predicted for the hcp(sqs) in both unrelaxed as well as relaxed cases (for the latter the barrier is  $1.8 \text{ meV/at.}$ , which is likely within the accuracy error of our calculations).

From Fig. 9.3b, it is predicted the unrelaxed bcc(sqs) has a similar energy landscape to the EMTO-CPA method, unlike the hcp(sqs). Since CPA is expected to provide a more accurate description of ideal random alloys than SQS supercells, we conclude that bcc(sqs) is likely to describe the transformation energetics better. The effect of atomic relaxation is clarified by comparing the relaxed and unrelaxed energies: the phase preference is inverted from  $\alpha'$  to  $\beta$ , which is likely to be linked to the dynamical instability of the  $\beta$  phase [109]. Further, the phase preference would be inverted from  $\beta$  to  $\alpha'$  by considering hcp(sqs) instead of bcc(sqs).

### 9.1.4 Strain energy

The cell shape changes without shuffling correspond to elastic deformations and hence the energy change along  $\delta_s = \text{const.}$  can be ascribed to the strain energy [135]. This allows to couple atomic description using quantum mechanics and linear elasticity. The strain energy,  $E_{\text{strain}}$ , can be estimated using elastic constants as in the following equation:

$$E_{\text{strain}} = \frac{1}{2}V_0 \sum C_{ij}\epsilon_i\epsilon_j \quad (9.1)$$

where the  $V_0$  is the equilibrium volume, the  $C_{ij}$  are the elastic constants, and the  $\epsilon_{i,j}$  are the components of the strain tensor in Voigt's notation (it is explained in detail in Sec. 2.4).

Realizing, that the strain tensor for the cubic to hexagonal transformation does not contain any shear components, and using the matrix of elastic constants  $C_{ij}$ , the corresponding strain energy,  $E_{\text{strain}}$ , is

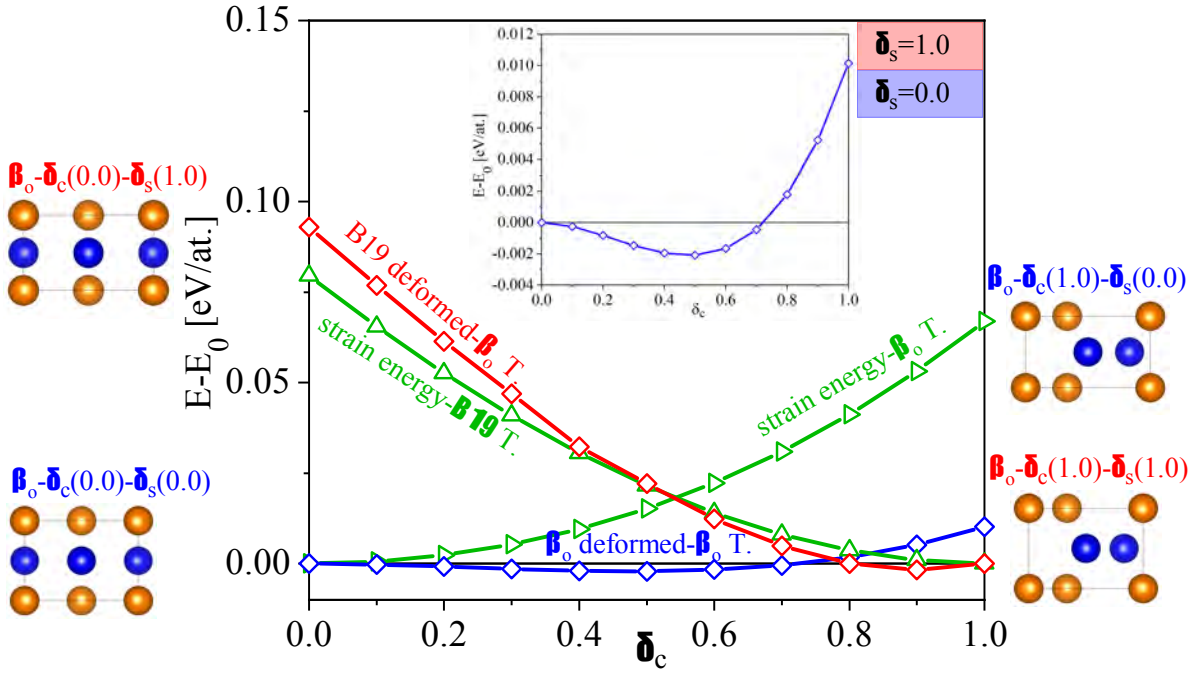
$$E_{\text{strain}} = \frac{1}{2}V_0 [C_{11}\epsilon_1^2 + 2C_{12}\epsilon_1\epsilon_2 + C_{22}\epsilon_2^2 + 2C_{13}\epsilon_1\epsilon_3 + C_{33}\epsilon_3^2 + 2C_{23}\epsilon_2\epsilon_3] \quad (9.2)$$

The strains are defined using the cell lattice constants with respect to the initial structure.

If a structure is elastically stable with respect to a chosen deformation, then the strain energy is positive and increases with increasing strain. As demonstrated in Fig. 9.4a, with transforming the  $\beta_o \rightarrow \text{B19}$ , the strain energy (the green curve that so-called ‘‘strain energy- $\beta_o$  T’’) quadratically increases. Unlike that, the total energy difference  $\Delta E((\delta_c, \delta_s = 0) - \beta_o)$  first slightly decreases and increases only for  $\delta_c \geq 0.5$ . This discrepancy is likely to be related to the mechanical instability of the  $\beta_o$  phase, which is not picked by the linear elasticity. In contrast to that, another approach by transforming the B19 structure and follow the path in terms of  $\delta_c$  (the green curve that so-called ‘‘strain energy-B19 T’’,  $\Delta E((\delta_c, \delta_s = 1) - \text{B19})$ ) exhibit a very decent correlation with the and red curve in Fig. 9.4a. This implies that PES for  $\delta_s \approx 1$  and  $0 \leq \delta_c \leq 1$  is dominated represent by the elastic energy. It also nicely demonstrates the mechanical stability of the B19 phase (red curve), in agreement with Sec. 4.2.3.

Figure 9.4b shows a similar result for the disordered phases, i.e. the  $\beta \rightarrow \alpha'$  transformation, and both considered SQS structures, bcc(sqs) (solid lines) and hcp(sqs) dashed lines. All SQS model are predicted to be mechanically stable, in line with results in Sec. 4.2.3. In particular for the bcc structures, the elastic energy very well agrees with energy derived from PES (the blue area); in the case of deforming the hexagonal  $\alpha'$  structure, the strain energy is smaller than the actual energy from PES,  $\Delta E((\delta_c, \delta_s = 1) - \alpha')$  (the red area), suggesting that in this case the linear elasticity is not fully capturing the behavior.

(a)



(b)

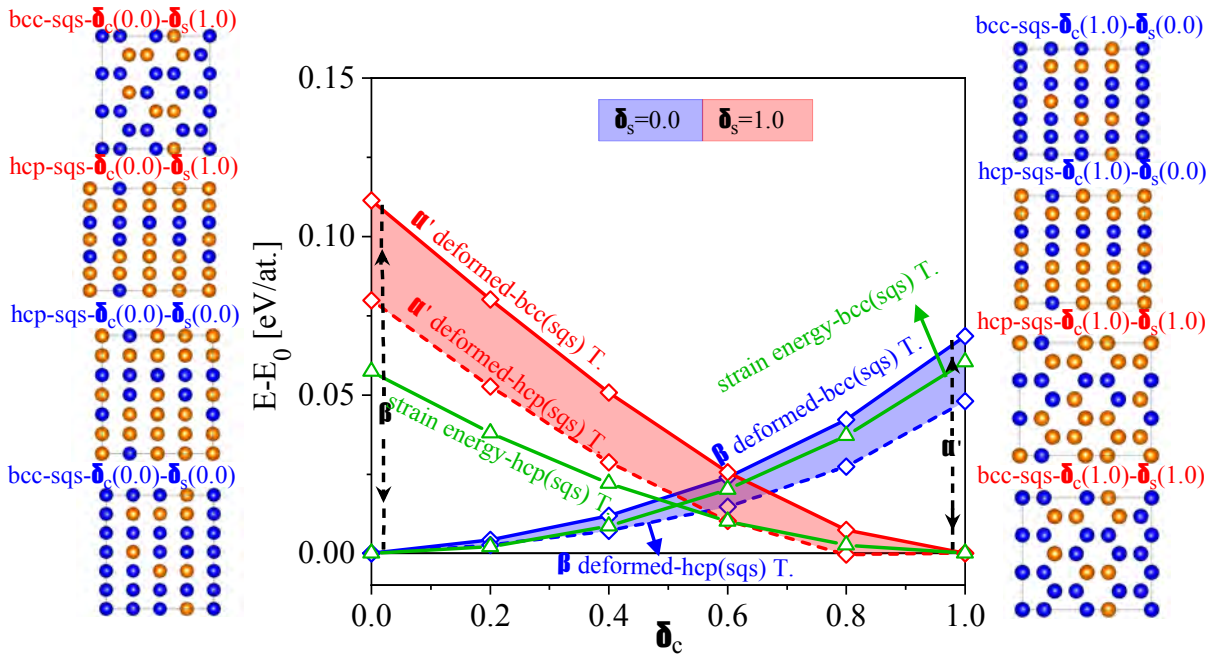


Figure 9.4: The strain energy and deformation <https://www.overleaf.com/project/60b4b903e751783898> of a)  $\beta_0 \rightarrow \text{B19}$  and b)  $\beta \rightarrow \alpha'$  in terms of cell shape changing.

Overall, the energy landscape for the cubic to hexagonal transformation can be approximated by the elastic strain energy fairly well, provided that the structures are mechanically stable.

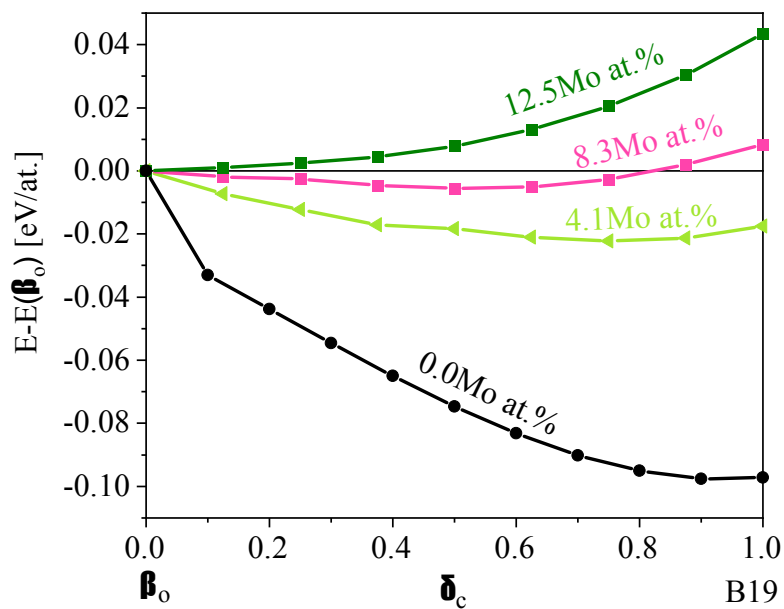
## 9.2 Energy barrier for ternary martensitic TiAl+Mo system

Figure 9.5a shows the transformation energy landscape along the path as a function of the Mo content for the ordered phases. While the B19 structure is clearly preferred for the Mo content of 0.0 and 4.16 at.% with no energy barrier between the  $\beta_o$  and the B19 phase, the situation is completely opposite for the 8.3 and 12.5 at.% Mo. There, the  $\beta_o$  phase is energetically preferred over the B19 phase without any transformation barrier which could be a sign for spontaneous transformations. This is interesting, because by increasing the Mo content, the spontaneous transformation  $\beta_o \rightarrow \text{B19}$  changes to  $\text{B19} \rightarrow \beta_o$ . The prediction of the later transformation for the high Mo content was described in detail in Sec. 4.3.2. Finally we note that in both 4.1 and 8.3 at.% cases, the overall energy minimum along the transformation path is obtained for  $\delta_c = 0.875$  and  $\delta_c = 0.5$ , respectively, suggesting that the most stable configuration is somewhere “in-between” the cubic  $\beta_o$  and the hexagonal B19 structure.

Figure 9.5b shows energy changes along the  $\beta \rightarrow \alpha'$  transformation path of several studied  $\text{Ti}_{0.5}\text{Al}_{0.5-x}\text{Mo}_x$  compositions. Unlike in the case of the ordered phases (Fig. 9.5a), the disordered phases do not exhibit any clear trend as a function of Mo content. The  $\beta$  structure is energetically slightly preferred for 0 at.% Mo, and this preference gradually changes with increasing Mo content for a slight preference for the  $\alpha'$  phase for 8.3 at.%. There is a small energy barrier for  $\beta \rightarrow \alpha'$  at 0 at.% Mo content, which diminishes with increasing Mo content, almost flattening the PES along most of the transformation path for 8.3 at.%. In contrary to this behavior, a clear preference for the  $\beta$  phase is predicted for 12.5 at.% Mo, with no barrier for  $\beta \leftarrow \alpha'$  a spontaneous transformation.

Existence of the barriers and/or flat and rough energy landscape opens the possibility of stabilizing both phases, i.e. the  $\alpha'$  ( $\beta$ ) phase would become metastable in the 0 and 4.1 at.% (8.3 at.%) Mo cases. Consequently, the chemical disorder effectively prevents any spontaneous phase transformations as predicted for the case of ordered  $\beta_o$  and  $\alpha'$  phases, except for the high Mo content of 12.5 at.%.

(a)



(b)

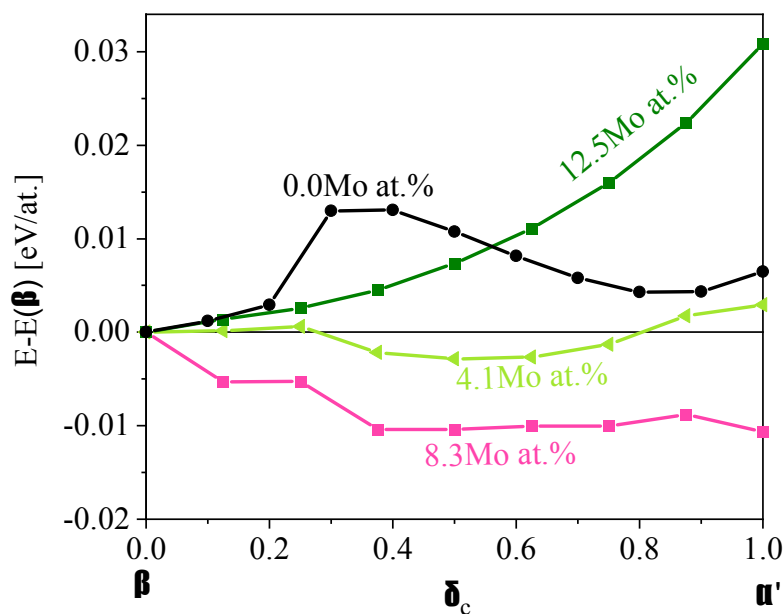


Figure 9.5: The energy landscape of (a)  $\beta_0 \rightarrow \text{B19}$  and (b)  $\beta \rightarrow \alpha'$  transformation (bcc(sq) state) in terms of cell shape parameter  $\delta_c$ , calculated as a function of Mo content.

---

## Conclusion and outlook

### 10.1 Summary of result

This thesis presents an overview of methods for modeling of phase transformations, and can be divided into three parts. The first part contains theoretical concepts and formalism for simulating the structures and structural connections between bcc and fcc, and bcc and hcp transformations. The second part deals with *ab initio* calculation of structural and mechanical and some thermodynamic properties of binary and ternary TiAl(+Mo) alloys. The last part brings the results of the phase transformations modeled using the description introduced in the first part.

A summary of the concepts behind the bcc to fcc and bcc to hcp phase transformations and the corresponding equations is given in the Chap. 3. The derived formulae were used for the investigation of how geometrical properties of bcc, fcc, and hcp unit cells change along with the phase transformation path in terms of some internal parameters, e.g., lattice changes, atomic positions or shuffling of atomic planes. In the fcc-to-bcc study, the Bain's path in which volume is not conserved, was innovatively employed. Additionally to this tetragonal transformation, a structural connection of the initial and final phases using a trigonal transformation was also studied. The second case focused on bcc→hcp transformation path applied to ordered  $\beta_o \rightarrow B19/\alpha'_2$  and disordered  $\beta \rightarrow \alpha'$  phases, to study martensitic transformations in the TiAl system. The deformation during the transformation is quantified in terms of two transformation parameters denoted as  $\delta_c$  and  $\delta_s$ , which represent cell shape changes and shuffle displacements, respectively.

Presentation of calculated results starts with Chap. 4 by discussing structural properties of binary and ternary TiAl(+Mo) alloys. The concepts of formation energy and phase stability were employed in these studies. All structures and compositions are yielding negative formation energies and hence are chemically stable. Nonetheless, alloying Mo



increases  $E_f$  and hence leads to chemical destabilization of all those phases except for  $\beta_o$ -Ti<sub>0.5</sub>Al<sub>0.5-x</sub>Mo<sub>x</sub> which is stabilized by Mo. This is inline with Mo being known as  $\beta$ -stabilizer. Additionally, alloying Mo into any of the here considered intermetallic phases leads to a decrease of specific volume, which means an increase of the mass density. Those trends based on supercell SQS calculations were confirmed by the CPA method. Analysis of single-crystalline elastic constants allowed to remove mechanically unstable compositions from a further discussion. Those were low-Mo containing  $\beta_o$  structures: to achieve mechanical stability of the ordered  $\beta_o$  phase, a minimum Mo content of  $\approx 8$  at.% is necessary.

The single crystalline elastic constants and polycrystalline elastic properties are presented in Chap. 5. Mo is shown to beneficially influence the ductility of TiAl intermetallic phases, and to increase the elastic anisotropy. The here provided compositional trends provide a basis for targeted, knowledge-based development of novel intermetallic alloys based on the TiAl(+Mo) ternary system.

In Chap. 7, the focus was laid on comparing energies of ordered ( $\beta_o$ , B19, partly-ordered  $\alpha'_2$ ) variants with their chemically disordered counterparts. Knowledge of the energy differences related to the ordering enables establishing ordering temperatures via a simple model. To do so, we assign the whole energy gain change upon ordering to the loss of configurational entropy.

Two different concepts based on quasi-harmonic approximation (QHA) were employed in Chap. 6 to see the temperature dependence of lattice parameters and coefficients of thermal expansion of tetragonal  $\gamma$ -TiAl and hexagonal  $\alpha_2$ Ti<sub>3</sub>Al of binary TiAl system. Our calculations show that in the case of the  $\gamma$ -TiAl phase, significant differences are obtained when employing gs-cs (ground-state cell shape) or to-cs (temperature-optimized cell shape) methods. Contrarily, comparable results are predicted for the hexagonal  $\alpha_2$ Ti<sub>3</sub>Al phase. We propose that the to-cs method with the decouples the impact of temperature and volume on the cell geometry ( $c/a$  ratio) gives better agreement for the  $\gamma$ -TiAl phase. The present work, therefore, contributes to advancing the first principles of thermodynamics beyond systems with cubic symmetry.

The energetics of a bcc-to-fcc transformation is predicted in Chap. 8. Energetic landscapes of structural connections between the bcc-based ordered  $\beta_o$  and disordered  $\beta$  phases on the one hand and fcc-based ordered  $\gamma$  and disordered  $\gamma_{\text{dis}}$  TiAl(+Mo) phases on the other hand are discussed. In the case of the stoichiometric TiAl system, the ordered phase is predicted to transform spontaneously from the bcc  $\beta_o$  to the tetragonally distorted fcc  $\gamma$  phase. Unlike that, the disorder stabilizes the bcc- $\beta$  phase and raises a small barrier between the bcc and the fcc phases. The trigonal path, however, transforms the ordered TiAl into a different structural type and exhibits a large energy barrier of

$\approx 500$  meV/at. in the ordered case, effectively ruling such structural connection out. A small barrier is predicted also for the transformation between disordered states. The impact of Mo, a known stabilizer of the  $\beta_o/\beta$  phase, was finally considered, too. It turns out that the bcc phase becomes energetically preferred over the  $\gamma$  phase for Mo content of  $\approx 7.4$  at.% and higher. Around this critical Mo content, a small energy barrier of  $\approx 1$  meV/at. is predicted. For all other compositions, the spontaneous (barrierless) nature of the Bain’s path connecting the  $\beta_o$  and  $\gamma$  phases are predicted to prevail. Unlike that, Bain’s path connecting the disordered bcc  $\beta$  and fcc  $\gamma_{\text{dis}}$  phases exhibits a barrier for all Mo concentrations considered here, effectively making it possible for both phases to co-exist. Finally, the instability of the  $\beta$ -TiAl(+Mo) phase was linked to individual atomic environments, exhibiting a strong tendency to locally resemble the tetragonally distorted structure of the  $\gamma_{\text{dis}}$ -TiAl(+Mo) phase.

In the Chap. 9, the *ab initio* calculations of the martensitic bcc-to-hcp transformation for binary and ternary TiAl(+Mo) alloys were reported. Since the PES clearly suggest that the MEPs are not straight connections of the initial and final states, we have additionally relaxed the ionic positions using our SQS supercells which yielded different result from the EMT0-CPA method. We could show that the elastic energy is a decent approximation of PES as a function of  $\delta_c$  for fixed  $\delta_s$ , provided the initial structure is mechanically stable. Moreover, the transformation energy landscape as a function of Mo content predicts, that adding Mo favors  $\beta_o/\beta$  phase on the expense of B19/ $\alpha'$ , eventually leading to spontaneous barrierless transformations  $\text{B19} \rightarrow \beta_o$  and  $\alpha' \rightarrow \beta$  for 12.5 at.% Mo.

This work presents novel and consistent information on structural and elastic and thermodynamic properties of binary TiAl and ternary TiAl+Mo systems. Energetics of possible diffusion-less phase transformations in the ternary TiAl+Mo system are presented for the first time. These results are expected to deepen understanding of this industrially important intermetallic system and provide a basis for further knowledge-based development of novel alloys based on TiAl+Mo.

## 10.2 Proposed future work

This work covers a wide range of problems. Consequently, the here reported results can also serve as a motivation for further research. In this section are suggested some possible directions of future studies based on the conclusions of this work.

For example, the machine-learned potentials and MD simulation could be used for an explicit modeling of the transformation energetic at finite temperatures. Alternatively, the Debye model using the elasticity results, shall be investigated as an approximation of the PES at finite temperature effects.

---

## Bibliography

- [1] T. Pusztai, G. Tegze, G. I. Tóth, L. Környei, G. Bansel, Z. Fan, and L. Gránásy, [Journal of Physics: Condensed Matter](#) **20**, 404205 (2008).
- [2] X. Wang, W. Xu, P. Xu, H. Zhou, F. Kong, and Y. Chen, [Metals](#) **10** (2020).
- [3] H. Clemens and S. Mayer, [Materials at High Temperatures](#) **33**, 560 (2016).
- [4] X. Wu, [Intermetallics](#) **14**, 1114 (2006).
- [5] E. Abe, T. Kumagai, and M. Nakamura, [Intermetallics](#) **4**, 327 (1996).
- [6] J. W. Wang and H. Gong, [International Journal of Hydrogen Energy](#) **39**, 1888 (2014).
- [7] T. Schmoelzer, K.-D. Liss, G. A. Zickler, I. J. Watson, L. M. Droessler, W. Wallgram, T. Buslaps, A. Studer, and H. Clemens, [Intermetallics](#) **18**, 1544 (2010).
- [8] T. Klein, M. Schachermayer, D. Holec, B. Rashkova, H. Clemens, and S. Mayer, [Intermetallics](#) **85**, 26 (2017).
- [9] H. Clemens and S. Mayer, [Advanced Engineering Materials](#) **15**, 191 (2013).
- [10] S. Zhang, Z. Song, J. Han, C. Zhang, P. Lin, D. Zhu, F. Kong, and Y. Chen, [Journal of Materials Science & Technology](#) **34**, 1196 (2018).
- [11] F. Appel, J. D. H. Paul, and M. Oehring, [Gamma Titanium Aluminide Alloys](#) (Wiley Online Library, 2011).
- [12] J. C. Schuster and M. Palm, [Journal of Phase Equilibria and Diffusion](#) **27**, 255 (2006).
- [13] J. Wang and T. Nieh, [Intermetallics](#) **8**, 737 (2000).
- [14] N. Abdoshahi, P. Spoerk-Erdely, M. Friák, S. Mayer, M. Šob, and D. Holec, [Physical Review Materials](#) **4**, 103604 (2020).

- [15] M. Palm, B. P. Bewlay, K. S. Kumar, and K. Yoshimi, in *Materials Research Society, Symp. Proc.*, Vol. 1295 (2011).
- [16] S. Mayer, M. Petersmann, F. D. Fischer, H. Clemens, T. Waitz, and T. Antretter, *Acta Materialia* **115**, 242 (2016).
- [17] S. Kabra, K. Yan, S. Mayer, T. Schmoelzer, M. Reid, R. Dippenaar, H. Clemens, and K.-D. Liss, *International Journal of Materials Research* **102**, 697 (2011).
- [18] T. Schmoelzer, S. Mayer, C. Sailer, F. Haupt, V. Guether, P. Staron, K.-D. Liss, and H. Clemens, *Advanced Engineering Materials* **13**, 306 (2011).
- [19] Y. Wen, L. Wang, H. Liu, and L. Song, *Crystals* **7**, 39 (2017).
- [20] T. Schmoelzer, A. Stark, E. Schwaighofer, T. Lippmann, S. Mayer, and H. Clemens, *Advanced Engineering Materials* **14**, 445 (2012).
- [21] B. Rashkova, K. Spiradek-Hahn, M. Brabetz, Z. Zhang, T. Schöberl, H. Clemens, and S. Mayer, *International Journal of Materials Research* **106**, 725 (2015).
- [22] M. Musi, P. Erdely, B. Rashkova, H. Clemens, A. Stark, P. Staron, N. Schell, and S. Mayer, *Materials Characterization* **147**, 398 (2019).
- [23] M. Born and R. Oppenheimer, *Annalen der Physik* **389**, 457 (1927).
- [24] V. Fock, *Zeitschrift für Physik* **61**, 126 (1930).
- [25] J. G. Lee, *Computational Materials Science: An Introduction* (CRC Press, 2016).
- [26] P. Hohenberg and W. Kohn, *Physical Review* **136**, B864 (1964).
- [27] R. Courant, *Lecture Notes in Pure and Applied Mathematics* **49**, 1 (1943).
- [28] W. Kohn and L. J. Sham, *Physical Review* **140**, A1133 (1965).
- [29] R. Stowasser and R. Hoffmann, *Journal of the American Chemical Society* **121**, 3414 (1999).
- [30] R. G. Parr, in *Horizons of Quantum Chemistry* (Springer, 1980) pp. 5–15.
- [31] D. M. Ceperley and B. J. Alder, *Physical Review Letters* **45**, 566 (1980).
- [32] J. P. Perdew and Y. Wang, *Physical Review B* **45**, 13244 (1992).
- [33] J. P. Perdew, K. Burke, and M. Ernzerhof, *Physical Review Letters* **77**, 3865 (1996).

- [34] P. Borlido, J. Schmidt, A. W. Huran, F. Tran, M. A. Marques, and S. Botti, [npj Computational Materials](#) **6**, 1 (2020).
- [35] A. J. Garza and G. E. Scuseria, [The Journal of Physical Chemistry Letters](#) **7**, 4165 (2016).
- [36] S. Cottenier, “Density Functional Theory and the family of (L)APW-methods: a step-by-step introduction,” (2013), [http://susi.theochem.tuwien.ac.at/reg\\_user/textbooks/DFT\\_and\\_LAPW\\_2nd.pdf](http://susi.theochem.tuwien.ac.at/reg_user/textbooks/DFT_and_LAPW_2nd.pdf).
- [37] J. E. Lennard-Jones, [Transactions of the Faraday Society](#) **25**, 668 (1929).
- [38] C. Herring, [Physical Review](#) **57**, 1169 (1940).
- [39] P. E. Blöchl, [Physical Review B](#) **50**, 17953 (1994).
- [40] F. Bloch, [Zeitschrift für Physik](#) **52**, 555 (1929).
- [41] C. Kittel and P. McEuen, [Introduction to Solid State Physics](#), Vol. 8 (Wiley New York, 1996).
- [42] C. Stampfl and A. J. Freeman, [Physical Review B](#) **67**, 064108 (2003).
- [43] K. Reuter and M. Scheffler, [Physical Review B](#) **65**, 035406 (2001).
- [44] F. Mouhat and F.-X. Coudert, [Physical Review B](#) **90**, 224104 (2014).
- [45] M. Born, in [Mathematical Proceedings of the Cambridge Philosophical Society](#), Vol. 36 (Cambridge University Press, 1940) pp. 160–172.
- [46] M. A. Caro, S. Schulz, and E. P. O’Reilly, [Journal of Physics: Condensed Matter](#) **25**, 025803 (2012).
- [47] N. Koutná, [Superlattice Design for Nitride-Based Thin Films](#), Ph.D. thesis, TU Wien, Austria (2021).
- [48] J. F. Nye, [Physical Properties of Crystals](#) (Clarendon Press, Oxford, 1957).
- [49] A. Togo and I. Tanaka, [Scripta Materialia](#) **108**, 1 (2015).
- [50] D. Holec, N. Abdoshahi, S. Mayer, and H. Clemens, [Materials](#) **12**, 1292 (2019).
- [51] C. Schuh, D. Dunand, A. Wanner, and H. Clemens, [Intermetallics](#) **8**, 339 (2000).
- [52] F. Nabarro, [Intermetallics](#) **8**, 979 (2000).
- [53] C. Bittorf, S. Matthies, H. Priesmeyer, and R. Wagner, [Intermetallics](#) **7**, 251 (1999).

- [54] X. Li, R. Dippenaar, A. Shiro, T. Shobu, Y. Higo, M. Reid, H. Suzuki, K. Akita, K.-I. Funakoshi, and K.-D. Liss, [Intermetallics](#) **102**, 120 (2018).
- [55] T. Novoselova, S. Malinov, W. Sha, and A. Zhecheva, [Materials Science and Engineering: A](#) **371**, 103 (2004).
- [56] W. Zhang, B. Reddy, and S. Deevi, [Scripta Materialia](#) **45**, 645 (2001).
- [57] W. Stone and T. Kurfess, Technical Paper - Society of Manufacturing Engineers. MR , 1 (2002).
- [58] Y. He, R. Schwarz, T. Darling, M. Hundley, S. Whang, and Z. Wang, [Materials Science and Engineering: A](#) **239-240**, 157 (1997), 4th Conference on High-Temperature Intermetallics.
- [59] H. Fu, Z. Zhao, W. Liu, F. Peng, T. Gao, and X. Cheng, [Intermetallics](#) **18**, 761 (2010).
- [60] A. Togo, L. Chaput, I. Tanaka, and G. Hug, [Physical Review B](#) **81**, 174301 (2010).
- [61] F. Birch, [Physical Review](#) **71**, 809 (1947).
- [62] S.-H. Wei and S. Zhang, [Physical Review B](#) **62**, 6944 (2000).
- [63] D. Nöger, *Optimised Structural Models of Solid Solutions for Tensorial Properties*, Master's thesis, Montanuniversität Leoben, Austria (2017).
- [64] F. Appel, M. Oehring, and J. D. Paul, [Advanced Engineering Materials](#) **8**, 371 (2006).
- [65] G. Kresse and J. Furthmüller, [Physical Review B](#) **54**, 11169 (1996).
- [66] G. Kresse and D. Joubert, [Physical Review B](#) **59**, 1758 (1999).
- [67] O. K. Andersen, O. Jepsen, and G. Krier, *Lectures on Methods of Electronic Structure Calculations*, edited by V. Kumar, O. K. Andersen, and A. Mookerjee (World Scientific Singapore, 1994) p. 63.
- [68] L. Vitos, *Computational Quantum Mechanics for Materials Engineers, The EMTO Method and Applications* (Springer-Verlag London, 2007).
- [69] P. Soven, [Physical Review](#) **156**, 809 (1967).
- [70] B. L. Gyorffy, [Physical Review B](#) **5**, 2382 (1972).
- [71] L. Vitos, I. Abrikosov, and B. Johansson, [Physical Review Letters](#) **87**, 156401 (2001).

- [72] A. V. Ruban and M. Dehghani, [Physical Review B](#) **94**, 104111 (2016).
- [73] I. A. Abrikosov, A. M. N. Niklasson, S. I. Simak, B. Johansson, A. V. Ruban, and H. L. Skriver, [Physical Review Letters](#) **76**, 4203 (1996).
- [74] I. A. Abrikosov, S. I. Simak, B. Johansson, A. V. Ruban, and H. L. Skriver, [Physical Review B](#) **56**, 9319 (1997).
- [75] O. E. Peil, A. V. Ruban, and B. Johansson, [Physical Review B](#) **85**, 165140 (2012).
- [76] H. J. Monkhorst and J. D. Pack, [Physical Review B](#) **13**, 5188 (1976).
- [77] L. Vitos, H. Skriver, B. Johansson, and J. Kollár, [Computational Materials Science](#) **18**, 24 (2000).
- [78] L. Vitos, J. Kollár, and H. L. Skriver, [Physical Review B](#) **55**, 13521 (1997).
- [79] L. Vitos, [Physical Review B](#) **64**, 014107 (2001).
- [80] K. Momma and F. Izumi, [Commission on Crystallogr. Comput., IUCr Newsllett.](#), **7**, 106 (2006).
- [81] K. Momma and F. Izumi, [Journal of Applied Crystallography](#) **41**, 653 (2008).
- [82] K. Momma and F. Izumi, [Journal of Applied Crystallography](#) **44**, 1272 (2011).
- [83] A. Togo, L. Chaput, I. Tanaka, and G. Hug, [Physical Review B](#) **81**, 174301 (2010).
- [84] A. Togo and I. Tanaka, [Scripta Materialia](#) **108**, 1 (2015).
- [85] A. Zunger, S. Wei, L. Ferreira, and J. Bernard, [Physical Review Letters](#) **65**, 353 (1990).
- [86] S.-H. Wei, L. G. Ferreira, J. Bernard, and A. Zunger, [Physical Review B: Condens. Matter.](#) **42**, 9622 (1990).
- [87] P. J. Craievich, M. Weinert, J. M. Sanchez, and R. E. Watson, [Physical Review Letters](#) **72**, 3076 (1994).
- [88] P. Alippi, P. Marcus, and M. Scheffler, [Physical Review Letters](#) **78**, 3892 (1997).
- [89] M. Šob, L. G. Wang, and V. Vitek, [Computational Materials Science](#) **8**, 100 (1997).
- [90] M. Šob, L. G. Wang, and V. Vitek, [Materials Science and Engineering: A](#) **234**, 1075 (1997).
- [91] M. Šob, L. G. Wang, and V. Vitek, [Philosophical Magazine B](#) **78**, 653 (1998).

- [92] M. Šob, L. G. Wang, and V. Vitek, *Kovové Materiály (Metallic Materials)* **36**, 145 (1998).
- [93] V. Paidar, L. Wang, M. Sob, and V. Vitek, *Modelling and Simulation in Materials Science and Engineering* **7**, 369 (1999).
- [94] M. Friák, M. Šob, and V. Vitek, *Physical Review B* **63**, 052405 (2001).
- [95] M. Šob, M. Friák, D. Legut, J. Fiala, and V. Vitek, *Materials Science and Engineering: A* **387-389**, 148 (2004).
- [96] D. Legut, M. Friák, and M. Šob, *Physical Review B* **81**, 214118 (2010).
- [97] M. Friák, T. Hickel, F. Körmann, A. Udyansky, A. Dick, J. von Pezold, D. Ma, O. Kim, W. Counts, M. Šob, T. Gebhardt, D. Music, J. Schneider, D. Raabe, and J. Neugebauer, *Steel Research International* **82**, 86 (2011).
- [98] L. G. Wang, M. Šob, and Z. Zhang, *Journal of Physics and Chemistry of Solids* **64**, 863 (2003).
- [99] M. Zouhar and M. Šob, *Physical Review B* **94**, 184110 (2016).
- [100] M. Friák, A. Schindlmayr, and M. Scheffler, *New Journal of Physics* **9**, 5 (2007).
- [101] D. Legut, M. Friák, and M. Šob, *Physical Review Letters* **99**, 016402 (2007).
- [102] M. Zelený, M. Friák, and M. Šob, *Physical Review B* **83**, 184424 (2011).
- [103] M. Friák and M. Šob, *Physical Review B* **77**, 174117 (2008).
- [104] Z. Lu, W. Zhu, T. Lu, and W. Wang, *Modelling and Simulation in Materials Science and Engineering* **22**, 025007 (2014).
- [105] A. Ojha and H. Sehitoglu, *Computational Materials Science* **111**, 157 (2016).
- [106] B. Cordero, V. Gómez, A. E. Platero-Prats, M. Revés, J. Echeverría, E. Cremades, F. Barragán, and S. Alvarez, *Dalton Transactions* , 2832 (2008).
- [107] J. C. Slater, *The Journal of Chemical Physics* **41**, 3199 (1964).
- [108] N. N. Greenwood and A. Earnshaw, *Chemistry of the Elements 2nd Edition* (Butterworth-Heinemann, 1997).
- [109] D. Holec, D. Legut, L. Isaeva, P. Souvatzis, H. Clemens, and S. Mayer, *Intermetallics* **61**, 85 (2015).



- [110] D. Holec, R. K. Reddy, T. Klein, and H. Clemens, [Journal of Applied Physics](#) **119**, 205104 (2016).
- [111] M. Moakher and A. N. Norris, [Journal of Elasticity](#) **85**, 215 (2006).
- [112] L.-Y. Tian, L.-H. Ye, Q.-M. Hu, S. Lu, J. Zhao, and L. Vitos, [Computational Materials Science](#) **128**, 302 (2017).
- [113] S. Pugh, [The London, Edinburgh, and Dublin Philosophical Magazine and Journal of Science](#) **45**, 823 (1954).
- [114] D. Pettifor, [Materials Science and Technology](#) **8**, 345 (1992).
- [115] S. Ranganathan and M. Ostoja-Starzewski, [Physical Review Letters](#) **101**, 55504 (2008).
- [116] L. Capolungo, I. J. Beyerlein, and Z. QWang, [Modelling and Simulation in Materials Science and Engineering](#) **18**, 085002 (2010).
- [117] T. Hickel, B. Grabowski, F. Körmann, and J. Neugebauer, [Journal of Physics: Condensed Matter](#) **24**, 053202 (2011).
- [118] A. Glensk, B. Grabowski, T. Hickel, and J. Neugebauer, [Physical Review Letters](#) **114**, 195901 (2015).
- [119] B. Grabowski, T. Hickel, and J. Neugebauer, [Physical Review B](#) **76**, 024309 (2007).
- [120] V. Witusiewicz, A. Bondar, U. Hecht, O. Stryzhyboroda, N. Tsyganenko, V. Voblikov, V. Petyukh, and T. Y. Velikanova, [Journal of Alloys and Compounds](#) **749**, 1071 (2018).
- [121] M. Dehghani, J. Spitaler, A. V. Ruban, N. Abdoshahi, and D. Holec, submitted (2021).
- [122] S. Mayer, P. Erdely, F. D. Fischer, D. Holec, M. Kasthuber, T. Klein, and H. Clemens, [Advanced Engineering Materials](#) **19**, 1600735 (2017).
- [123] P. J. Craievich, J. M. Sanchez, R. E. Watson, and M. Weinert, [Physical Review B](#) **55**, 787 (1997).
- [124] J. V. Pezold, A. Dick, M. Friák, and J. Neugebauer, [Physical Review B](#) **81**, 094203 (2010).
- [125] M. Kimura and K. Hashimoto, [Journal of Phase Equilibria](#) **20**, 224 (1999).

- [126] R. Kainuma, Y. Fujita, H. Mitsui, I. Ohnuma, and K. Ishida, [Intermetallics](#) **8**, 855 (2000).
- [127] Y. Li and M. Loretto, [Acta Metallurgica et Materialia](#) **42**, 2913 (1994).
- [128] A. Singh and D. Banerjee, [Metallurgical and Materials Transactions A](#) **28**, 1745 (1997).
- [129] S. Azad, R. Mandal, and A. Singh, [Materials Science and Engineering: A](#) **429**, 219 (2006).
- [130] D. M. Cupid, O. Fabrichnaya, F. Ebrahimi, and H. J. Seifert, [Intermetallics](#) **18**, 1185 (2010).
- [131] S. Mayer, C. Sailer, T. Schmoelzer, H. Clemens, T. Lippmann, P. Staron, V. Güther, and M. Takeyama, [BHM Berg-und Hüttenmännische Monatshefte](#) **156**, 438 (2011).
- [132] M. Engstler, S. Mayer, C. Pauly, H. Clemens, and F. Mücklich, [Advanced Engineering Materials](#) **15**, 1125 (2013).
- [133] P. Erdely, P. Staron, A. Stark, T. Klein, H. Clemens, and S. Mayer, [Acta Materialia](#) **164**, 110 (2019).
- [134] L. Usategui, M. Nó, S. Mayer, H. Clemens, and J. San Juan, [Materials Science and Engineering: A](#) **700**, 495 (2017).
- [135] D. Hull and D. J. Bacon, [Introduction to Dislocations](#) (Butterworth-Heinemann, 2011).